

N67-25041

FACILITY FORM 602

(ACCESSION NUMBER)

(THRU)

(PAGES)

(CODE)

(NASA CR OR TMX OR AD NUMBER)

(CATEGORY)

# Two Phase Detonations and Drop Shattering Studies

by

E. K. Dabora, K. W. Ragland, A. A. Ranger

J. A. Nicholls

Principal Faculty Investigator

prepared for

NATIONAL AERONAUTICS AND SPACE ADMINISTRATION  
Contract NASr 54(07)

April 1967

THE UNIVERSITY OF MICHIGAN  
Ann Arbor, Michigan

#### NOTICE

This report was prepared as an account of Government sponsored work. Neither the United States, nor the National Aeronautics and Space Administration (NASA), nor any person acting on behalf of NASA:

- A.) Makes any warranty or representation, expressed or implied, with respect to the accuracy, completeness, or usefulness of the information contained in this report, or that the use of any information, apparatus, method, or process disclosed in this report may not infringe privately owned rights; or
- B.) Assumes any liabilities with respect to the use of, or for damages resulting from the use of any information, apparatus, method or process disclosed in this report.

As used above, "person acting on behalf of NASA" includes any employee or contractor of NASA, or employee of such contractor, to the extent that such employee or contractor of NASA, or employee of such contractor prepares, disseminates, or provides access to, any information pursuant to his employment or contract with NASA, or his employment with such contractor.

Requests for copies of this report should be referred to

National Aeronautics and Space Administration  
Office of Scientific and Technical Information  
Attention: AFSS-A  
Washington, D.C. 20546

1136



4E TECHNICAL REPORT  
(Third Annual Progress Report for the period  
February 1, 1966 - January 31, 1967)

3 TWO PHASE DETONATIONS AND DROP SHATTERING STUDIES 4

by

6 E.K. Dabora, K. W. Ragland, and A. A. Ranger 7

J. A. Nicholls  
Principal Faculty Investigator

prepared for

NATIONAL AERONAUTICS AND SPACE ADMINISTRATION

9 April 1967 100-

CONTRACT NASr-54(07)-7

Technical Management  
NASA Lewis Research Center  
Cleveland, Ohio  
Chemistry and Energy Conversion Division  
Bruce J. Clark

2 Department of Aerospace Engineering, 3  
UNIVERSITY OF MICHIGAN  
Ann Arbor, Michigan

## FOREWORD

This report covers the progress made from February 1, 1966 to January 31, 1967 on a continuing study of the relation of two-phase detonations to liquid rocket motor instability under NASA Contract NASr 54(07). The study is under the direction of Professor J.A. Nicholls, Department of Aerospace Engineering. Mr. Bruce Clark of NASA Lewis Research Center, is the technical monitor.

## ACKNOWLEDGMENT

The authors wish to thank D. E. Haddock for designing the field effect transistor and the raster circuits. The assistance of D. Giere, W. Whitman, P-L Lu, R. May, H. Radcliff, and R. Stitt in carrying out the experiments and in data reduction is appreciated.

## TABLE OF CONTENTS

FOREWORD	Page ii
ACKNOWLEDGMENT	ii
ABSTRACT	iv
LIST OF FIGURES	v
LIST OF TABLES	viii
NOMENCLATURE	ix
I. INTRODUCTION	1
II. SPRAY DETONATION—EXPERIMENTAL RESULTS	4
1. Facility and Experimental Procedure	4
2. Experimental Results on 940 $\mu$ Drop Sprays	9
3. Detonation of 2600 $\mu$ Diameter Drops	17
III. TWO-PHASE DETONATION—THEORY AND APPLICATION	47
1. One Dimensional Difference Equations with Mass, Momentum and Heat Transfer at the Boundaries	48
2. Mass, Momentum and Heat Transfer Coefficients for a Film Detonation	56
3. Application—Estimate of the Effect of Drag and Heat Loss on Detonation Parameters for 2600 $\mu$ Drops	61
IV. DROP SHATTERING	65
1. Experimental Apparatus and Procedure	68
2. Results and Discussion	69
V. SUMMARY OF RESULTS	85
APPENDIX	87
1. Pressure Measurement	87
2. Heat Transfer Measurement	97
3. Velocity Measurement	104
REFERENCES	108

## ABSTRACT

Experimental results on detonations in two phase mixtures of liquid diethylcyclohexane and gaseous oxygen are presented. Measurements of detonation velocity, and pressure and heat transfer behind the wave are made on  $940\ \mu$  sprays at equivalence ratios .18-.96 and single streams of  $2600\ \mu$  drops at an equivalence ratio of .23. In general, the velocities are lower than the theoretical Chapman-Jouguet velocities and their variation with mixture ratio follow the theoretical trend. The structure of the reaction zone of the detonation of the  $2600\ \mu$  drops was studied by means of a new piezoelectric transducer (described in the report), thin film heat transfer gauges, and streak photography.

Difference equations for detonations with mass, momentum and heat transfer at the boundaries, as well as expressions for transfer coefficients of mass, momentum and heat transfer for diffusion limited laminar boundary layer behind a shock with vaporization and combustion are derived. The combined results can be applied to explain, in part, the measured velocity defect in the  $2600\ \mu$  drop mixture.

Experimental data on the acceleration, deformation and breakup time of water drops ( $750$ - $2700\ \mu$ ) by shock waves ( $M = 1.3 - 3.5$ ) in air initially at NTP are also included. Over the range studied, the breakup time is found to be approximately proportional to the drop diameter and the inverse of the convective flow velocity. Observed differences between the dynamics of inert drops and reacting drops behind the detonation front are discussed.

## LIST OF FIGURES

Figure No.	Title	Page
2.1	Schematic diagram of two-phase detonation setup	5
2.2	Schematic diagram of combustion tube showing transducer locations	6
2.3	Drop generator design	8
2.4	The appearance of spray at test section, 1 second before detonation	10
2.5	Progress of detonation velocity along the tube for 940 $\mu$ spray	12
2.6	Comparison of experimental results on velocity and pressure with theory	13
2.7	Pressure records of the detonation of 940 $\mu$ diameter drops from 4 needles (equiv. ratio = .18)	14
2.8	Pressure and heat transfer records of the detonation of 940 $\mu$ drops from 25 needles (equiv. ratio = .96)	15
2.9	Photograph of 2600 $\mu$ drops in the combustion tube	18
2.10	Schematic of the optical system for the framing camera photographs	19
2.11	Framing camera photographs and pressure record of the detonation of 2600 $\mu$ drops	21
2.12	Schematic of the optical system for the streak photographs	23
2.13	Combined self-luminous and shadow streak photographs of the detonation of 2600 $\mu$ drops	24
2.14	Displacement of 2600 $\mu$ diameter drop vs. time after passage of detonation front	34
2.15	Pressure record of 2600 $\mu$ diameter droplet detonation using Kistler pressure transducers	36

Figure No.	Title	Page
2.16	Pressure and heat transfer records of 2600 $\mu$ diameter droplet detonations using pressure transducers with acoustic absorbing rod and platinum thin film resistance gauges	38
2.17	Propagation velocity vs. distance from ignition source for 2600 $\mu$ diameter drop detonation	43
2.18	Heat transfer to the wall from data shown in Fig. 2.16(i, j, k).	46
3.1	Control volume and coordinate system for use with one-dimensional conservation equations	49
3.2	Model for film detonation: normal shock moving across a flat plate with boundary layer combustion	57
4.1	Schematic of shock wave-liquid drop interaction	66
4.2	The two types of drop disintegration	67
4.3	The appearance of 750 $\mu$ water drops at various times after the passage of $M_s = 2$ shock in air	70
4.4	The appearance of 2700 $\mu$ water drops at various times after the passage of $M_s = 3$ shock in air	71
4.5	The appearance of 2700 $\mu$ water drops at various times after the passage of $M_s = 3.5$ shock in air	75
4.6	The appearance of 1090 $\mu$ water drops at various times after the passage of $M_s = 3.25$ shock in air	76
4.7	Deformation of 2700 $\mu$ drop	77
4.8	Displacement of 2700 $\mu$ water drop after passage of wave	79
4.9	Non-dimensional displacement vs. non-dimensional time	80
4.10	Effect of shock Mach number on the breakup time	81

Figure No.	Title	Page
4. 11	Breakup time correlation with the dynamic pressure	83
4. 12	Correlation of non-dimensional time with $Re_g$ , $We$ , $M_2$ and $\beta$	84
A. 1	Response of Kistler pressure transducers to a 1 atm stoichiometric hydrogen-oxygen gaseous detonation	88
A. 2	Pressure transducer with acoustic absorbing rod	91
A. 3	High impedance circuit for the pressure transducer utilizing a field effect transistor	95
A. 4	Response of 1/8 in. diameter lead metaniobate-tin pressure transducer	96
A. 5	Assembly drawing of heat transfer gauge	98
A. 6	Operating circuit for heat transfer gauge	99
A. 7	Response of heat transfer gauge to a 1 atm stoichiometric hydrogen-oxygen gaseous detonation	102
A. 8	Experimental and theoretical heat transfer to the wall behind a 1 atm stoichiometric hydrogen-oxygen gaseous detonation	103
A. 9	Schematic diagram of raster circuit	105
A. 10	Typical raster record	107

## LIST OF TABLES

	Page
I.      Analysis of streak photographs of 2600 $\mu$ diameter drop detonation	30
II.     Analysis of pressure records from detonation of 2600 $\mu$ diameter drops	44
III.    Summary of initial conditions satisfying the Blasius equation for various values of $M_s$ and B	60
IV.    Summary of estimated drag coefficients	62
V.     Drop breakup variables	68
VI     Properties of several piezoelectric disks normal to the direction of the applied force	93



## NOMENCLATURE

(A roman numeral after a definition refers to corresponding section where that definition is used.)

A	Gauge constant
$A_c$	Cross sectional area
$A_s$	Surface area between stations 2 and 3 of Fig. 3.1
a	Speed of sound
B	Parameter defined by Eq. (3.25).
b	Perimeter of the surface through which mass is added
C	Defined by Eq. (8)
$C_p$	Specific heat at constant pressure
$C_D$	Drag coefficient defined by Eq. (3.27)
$C_H$	Heat transfer coefficient defined by Eq. (3.28)
$C_M$	Mass transfer coefficient defined by Eq. (3.26)
c	Specific heat
D	Defined by Eq. (3.9)
$D_o$	Initial drop diameter (IV)
E	Defined by Eq. (3.10)
$E( )$	Voltage
e	Internal energy per unit mass
$e_m$	Internal energy of the added mass per unit mass
f	Blasius function, the solution of Eq. (3.20)
$\Delta H$	Heat of combustion per unit mass of fuel

$h$	Enthalpy per unit mass
$h_L$	Latent heat of vaporization per unit mass
$I$	Current
$k$	Conductivity
$M$	Mass added through control surface per unit area per second
$M_i$	Symbol for chemical species $i$
$M_s$	Mach number of propagation of shock or detonation
$m$	Molecular weight
$n$	Time interval index
$p$	Pressure
$Q$	Heat added by chemical reaction per unit area per second
$q$	Heat loss out of control surface per unit area per second
$q_2$	$\frac{1}{2} \rho_2 V_2^2$
$R$	Universal gas constant
$Re$	Reynolds number
$R_o$	Initial resistance
$T$	Static temperature
$\overline{T}$	Non-dimensional time = $tV_2/D_o \beta^{1/2}$
$t$	Time
$t_b$	Breakup time
$u$	Mass average velocity in the $x$ direction
$V$	Flow velocity
$V_s$	Incident shock propagation velocity (IV)

$v$	Mass average velocity in the y direction
We	Weber number: $\rho_2 V_2^2 D_o / \sigma$
X	Distance between shock and end of reaction zone, i. e., $x_3 - x_2$
x	Distance, see Figs. 3.1 and 3.2
x	Displacement (IV)
$\bar{x}$	$x/D_o$ = non-dimensional displacement (IV)
$\alpha$	Coefficient of resistivity
$\beta$	Liquid-gas density ratio $\rho/\rho_2$ (IV)
$\gamma$	Ratio of specific heats
$\eta$	Similarity parameter defined by Eq. (3.24)
$\mu$	Viscosity
$\nu_i'$	Stoichiometric coefficient for species i appearing as a reactant
$\nu_i''$	Stoichiometric coefficient for species i appearing as a product
$\rho$	Density
$\sigma$	Surface tension
$\tau$	Shear stress per unit surface area
$\tau$	Nondimensional time (IV) Dummy variable (App. )
$\phi$	Fuel to oxidizer mass ratio
$\psi$	Arbitrary function

### Subscripts

1, 2, 3, w, s	Defined in Figs. 3.1 and 3.2 (I-III)
1	Initial condition (IV)
2	Convective flow condition (IV)
$\ell$	Liquid (IV)

### Superscript

—	Refers to shock fixed coordinate system (I-III) Nondimensional quantity (IV)
---	---

## I. INTRODUCTION

The motivation for investigating two-phase detonation waves stems from the fact that shock and detonation phenomena are now known to exist in liquid propellant rocket motors. Our studies on two phase detonations have shown that such waves are relatively easy to produce <sup>(1,2,3)</sup>. Detonations or steep fronted waves supported by combustion have been consistently obtained in mixtures consisting of gaseous oxygen and liquid fuel where the fuel was either in a spray or in a film on the walls of the tube. It is found from our experiments that the detonation mechanism in the spray case is related to the shattering of the drops by the convective gaseous flow, and in the film case to film stripping, evaporation, and the high surface to volume ratio of the fuel. A supporting study on the mechanism of drop breakup by shock waves without the influence of combustion has shown that water drops of the order of  $1000\ \mu$  in diameter exhibit appreciable surface shear and mass removal in a few microseconds after the passage of a 3.5 Mach number shock in air originally at NTP. In the spray detonation larger Mach numbers are involved so that drop stripping and breakup can start at even shorter times.

Aside from the pertinence of our studies to rocket motor instability, there are other applications which can be cited. For part of the operating regime, the supersonic combustion ramjet (scramjet) will likely use liquid fuel injection. In view of the very high velocities in the combustor it is important to know the rate of breakup of the fuel and its effect on the combustion rate. Other applications would include the use of liquid fuels injected on the outside of an aerodynamic body for external combustion or for control forces, thrust vector control, and the interaction of supersonic vehicles with clouds.

The theoretical and experimental studies on the subject of two phase detonation which preceded our work have been reviewed in the past (Ref. 1,3). Reference (3) also included a comprehensive review of the literature pertinent to the subject of drop shattering. Recently, some preliminary experiments

have been carried out by Morris et al.<sup>(4)</sup> on the development of detonation in a mixture of kerosene and oxygen. Streak photographs of the self-emitting phenomenon were obtained from which velocities of 5000-7100 ft/sec were measured. However no correlation with mixture ratio was attempted.

In our previous reports<sup>(1, 3)</sup>, the jump relations for two phase detonations without dissipative losses were derived. It was shown in (Ref. 3) that a dilute spray could be treated as a pseudo-ideal gas. This facilitated the comparison between a spray detonation and its "all gaseous" counterpart with the same heat release per unit mass of mixture. Computer calculations were performed<sup>(2, 3)</sup> for diethylcyclohexane (DECH) (vapor pressure  $\cong 1.5$  mm Hg at 70°F) and oxygen mixtures to obtain the Chapman-Jouguet velocity and Mach number, and pressure, temperature and density ratios for the spray as a function of equivalence ratio. Analytical work which treats the film detonation as a laminar boundary layer problem with mass addition and heat release resulting from reaction was also performed<sup>(3)</sup>. Experimental observations on both types of detonations and on drop shattering were also reported<sup>(1, 3)</sup>. The spray and drop shattering experiments necessitated the production of controlled sizes of drops and therefore a technique to accomplish this was developed<sup>(1, 5)</sup> and used.

In this report we present experimental results on the effect of mixture ratio on the propagation of detonation for one size (940  $\mu$ ) droplet field. In addition detailed experimental results on a single stream of drops (2600  $\mu$ ) are described. To assess the reaction zone, measurements of pressure and heat transfer within the reaction zone are made. Pressure measurements with commercially available transducers were inadequate to resolve the pressure history in detail. Therefore a pressure transducer, which is described in this report, was developed and has been used with encouraging results. Heat transfer measurements with thin film transducers are also reported.

Experiments on the shattering of water drops when subjected to shocks in air under wider conditions than reported before are made and the results are discussed. Comparison between the dynamics of these inert drops and the dynamics of fuel drops ( $2600\ \mu$ ) in the single stream detonation experiments is made.

In addition to the above experiments, further analytical results on the film detonation problem are presented. Also, treatment of the jump relations wherein account of drag on the walls and/or drops as well as heat losses within the reaction zone behind the detonation front, is made and the results are applied to the detonation of a single droplet stream.

## II. SPRAY DETONATION: EXPERIMENTAL RESULTS

### 1. Facility and Experimental Procedure.

The experimental facility for studying two-phase detonations consists of the following main items: a) a device for producing a fuel spray, b) a tube in which the spray is evenly distributed with the gaseous oxygen, c) an initiation device, and d) instrumentation for the operation of the facility and for data acquisition. Several versions of such a facility have been described in detail before <sup>(1,2,3)</sup> and Fig. 2.1 shows a schematic diagram of the setup used for the experiments reported here. The detonation tube which is shown schematically in Fig. 2.2, is a square tube 12-1/3 ft. long with an internal side of 1.64". It is provided with two viewing sections. The top section is used for observation of the spray before a run is made to insure that it is properly set up. To one side wall of this section, the driven section of the initiating tube is flush mounted at a 45° angle. The lower viewing section which will be called the test section has an 11" long window with its center located at 83" from the top of the tube and is used for photographic observations during a run. Mounted flush with the inside wall of the tube, are pressure switches which, in conjunction with a multiple RC circuit and an oscilloscope operated in a raster mode as described in Ref. (3), are used for velocity measurement. The raster circuit used here is different from that used in Ref. (3) and is described in the Appendix. Pressure and heat transfer measurements are made by appropriate transducers which are described also in the Appendix. These transducers are located in general at stations near the test section where steady or nearly steady conditions prevail.

The device for producing monodisperse sprays is described in Ref. (1,3,5). It consists of a small cylindrical chamber fitted at its bottom with a plate having several capillary needles in parallel. The fuel capillary jets issuing from the needles are broken up into regular size drops when the chamber is



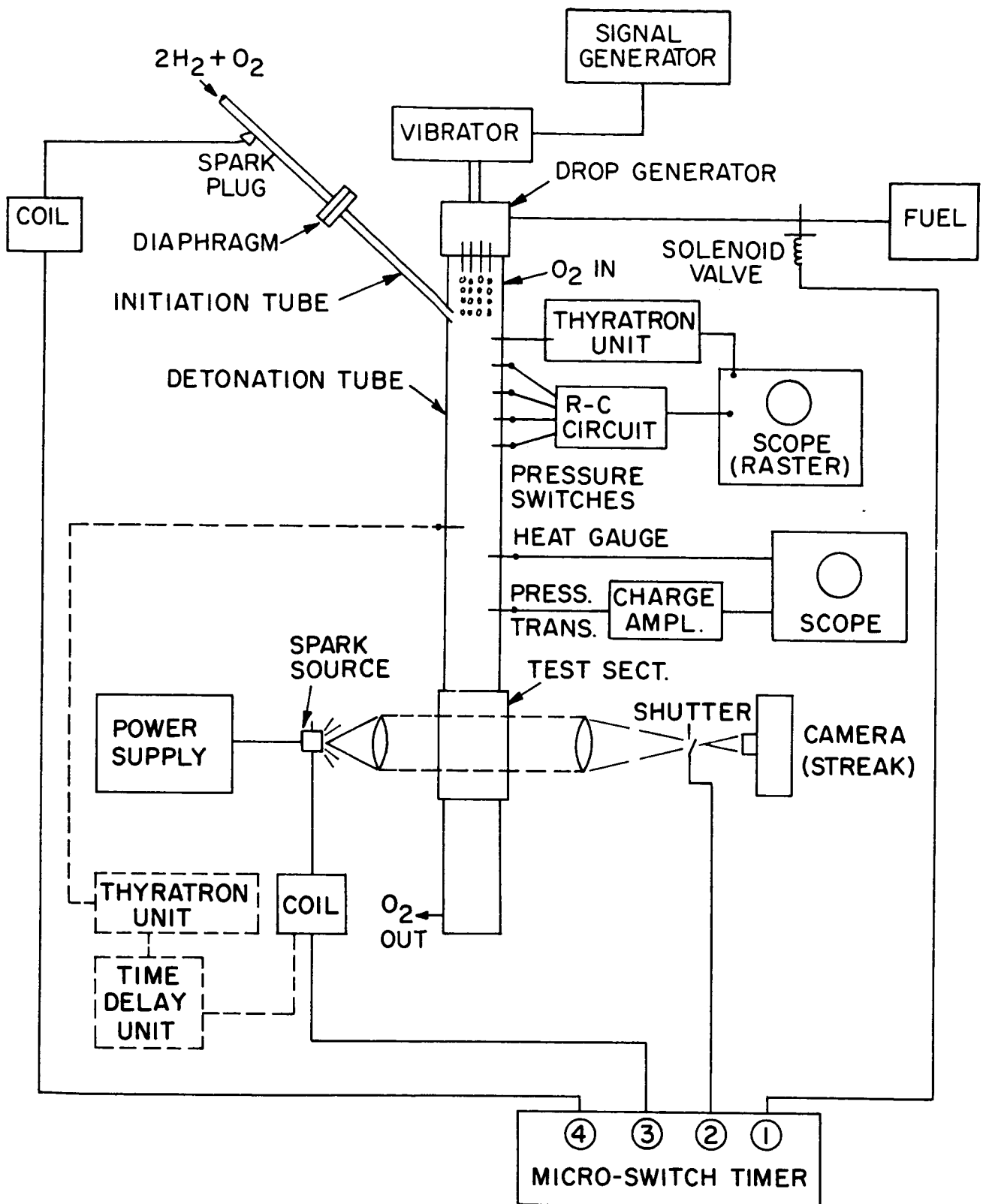


Figure 2.1 Schematic Diagram of Two-Phase Detonation Setup.

STATION  
LOCATION

①

②

③

④

⑤

⑥

⑦

⑧

⑨

⑩

⑪

⑫

⑬

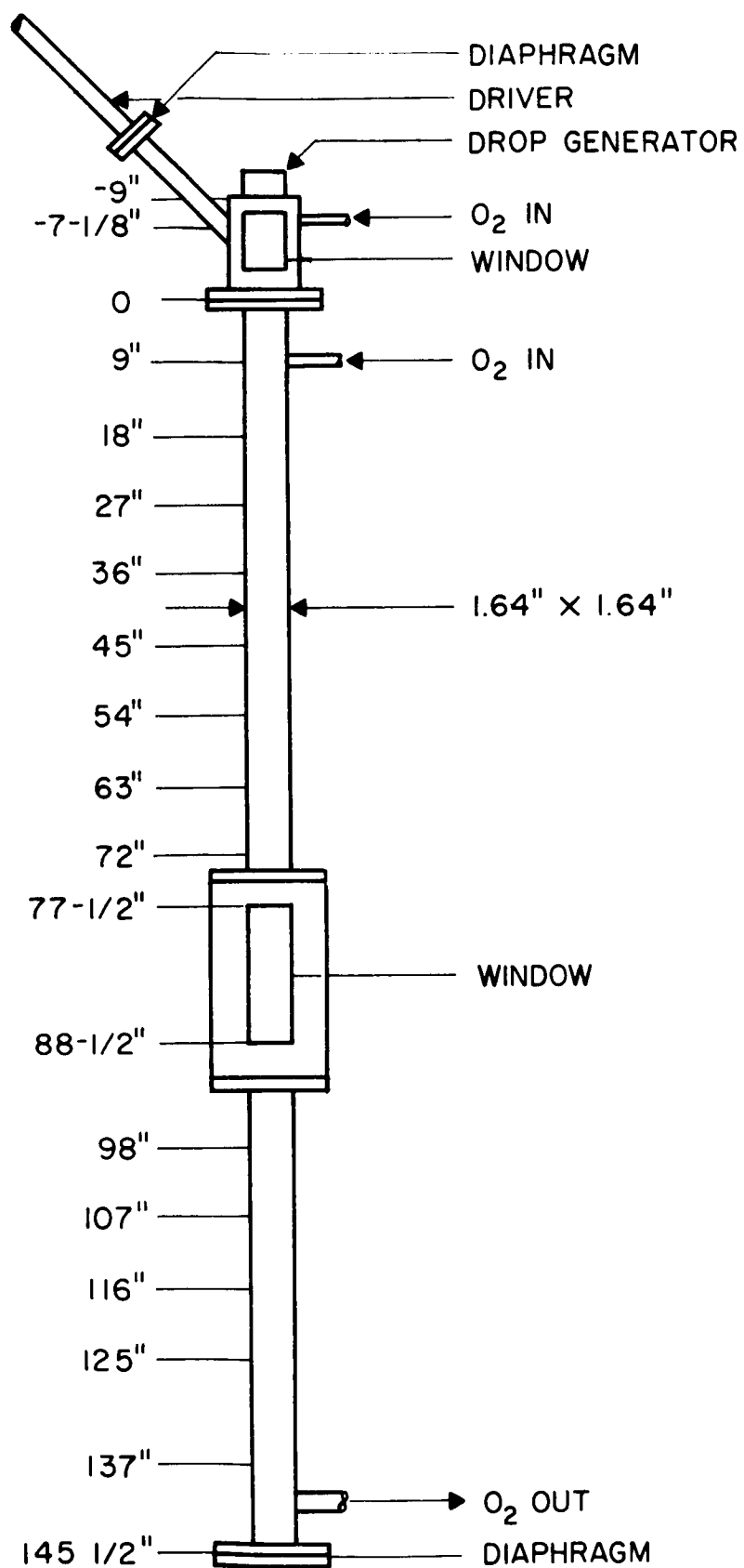


Figure 2.2 Schematic Diagram of Combustion Tube Showing Transducer Locations.

vibrated at the proper frequency as delineated in Ref. (5). It has been found that an equally adequate method of inducing vibration in the liquid jets is to vibrate a .003" brass shim stock piece which makes up the top base of the generator, as shown in Fig. 2.3. The main purpose of vibrating only the top part of the generator is to keep its main body free from motion and thus facilitate sealing it to the tube.

The operational procedure which can best be followed by referring to Fig. 2.1, is described next. The fuel flow through the drop generator and the signal generator frequency and amplitude are set and the drops are checked to insure that regular sizes are produced. Then the solenoid valve is closed, the detonation tube is dried with air and then purged with oxygen. The initiating tube is evacuated and filled with  $2\text{H}_2 + \text{O}_2$  mixture usually at atmospheric pressure. Then a cycle of events leading to detonation is started with the microswitch timer which has a total cycle of 10 sec and circuit controls in any position of the cycle to within 0.25 sec resolution. These events are as follows:

- 1) The solenoid valve is opened so that the fuel flows through the drop generator for a preset length of time controlled by the timer. The duration is sufficient to allow the first drops to reach the bottom of the tube and is usually 2-4 sec. The flow is terminated .25 sec after the detonation spark plug is fired. 2) The mechanical shutter is then opened, and 3) a spark-source ( $.2 \mu\text{sec}$  duration) or a flash unit (1 msec duration) are fired so that either photographs of the spray before detonation or of the detonation itself are obtained. When necessary, the light source is controlled by the event itself as shown by the dotted path in Fig. 2.1. Finally, 4) the spark plug for starting the gaseous detonation in the initiation tube is energized. This detonation produces a shock wave in the driven section which hits the spray and thus initiates a detonation in the main tube.

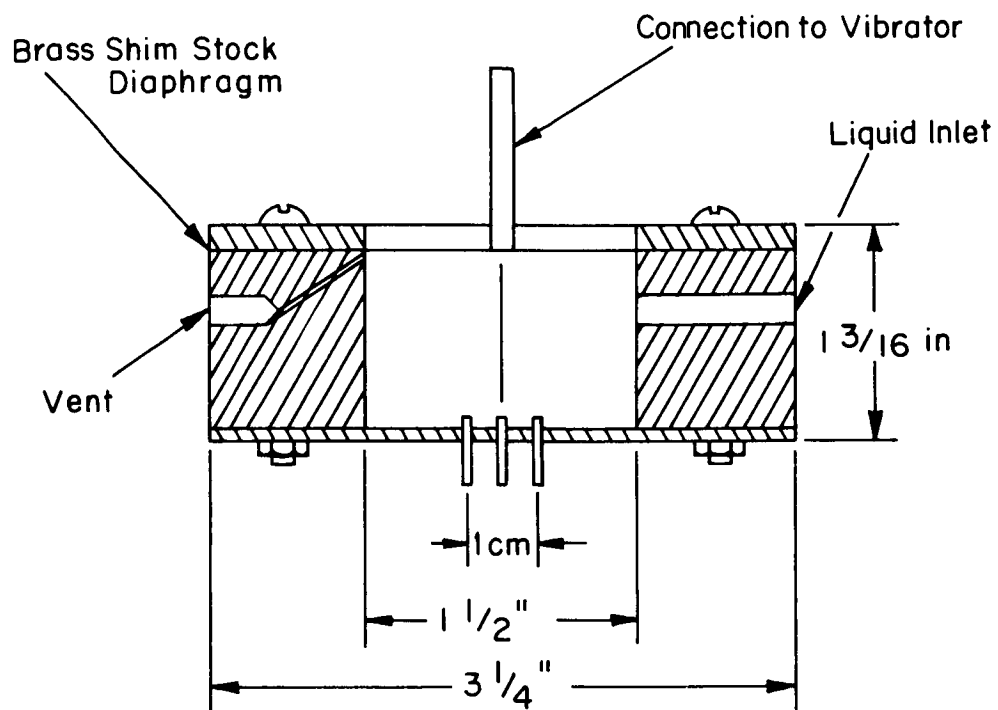


Figure 2.3 Drop Generator Design.

## 2. Experimental Results on 940 $\mu$ Drop Sprays.

Experiments with diethylcyclohexane (DECH) monodisperse sprays in oxygen were conducted for the purpose of checking the influence of fuel-oxygen ratio. The mixture is varied by changing the number of needles in the drop generator. Needle plates with 4, 12, and 25 needles (I.D. .020") are used resulting in 940  $\mu$ drops. Because of the nature of the spray producing device as discussed in Ref. (5), these plates gave, from a knowledge of the initial velocity (2.5 ft/sec) and shedding frequency ( $\sim 320$  Hz) equivalence ratios of 0.83, 2.37, and 4.87 respectively at the injection point. Because of the acceleration of the drops the equivalence ratios can theoretically be calculated to reach nearly constant values of 0.216, 0.608 and 1.27 respectively at distances beyond 4 ft from the injection point. However, due to some wall wetting, the measured equivalence ratio from photographs of the spray averaged 0.18, 0.42 and 0.96 respectively. Examples of spray photographs are shown in Fig. 2.4. As might be expected, both coalescence as evidenced by the presence of large drops, and wall wetting as evidenced by the streaks on the window, increase as the number of needles increase. In calculating the equivalence ratio, consideration of the coalescence as well as the drops on the wall which amount to about 20% of the fuel are taken into account.

It should be mentioned that in checking the spray when the 12 needle plate was first installed, it was found that the type of diaphragm used at the bottom of the tube as well as whether air or oxygen was in the tube affected the extent of both coalescence and wall wetting. A loose plastic bag gave the best results. The problem resulting from the type of gas in the tube was traced to the natural frequency of the gaseous column in the tube. When the drop generator is driven at a frequency which happens to be close to a multiple of the natural frequency of the tube, coalescence is more intense. The situation is corrected by driving the generator at a slightly different frequency from that dictated by theory<sup>(5)</sup>.

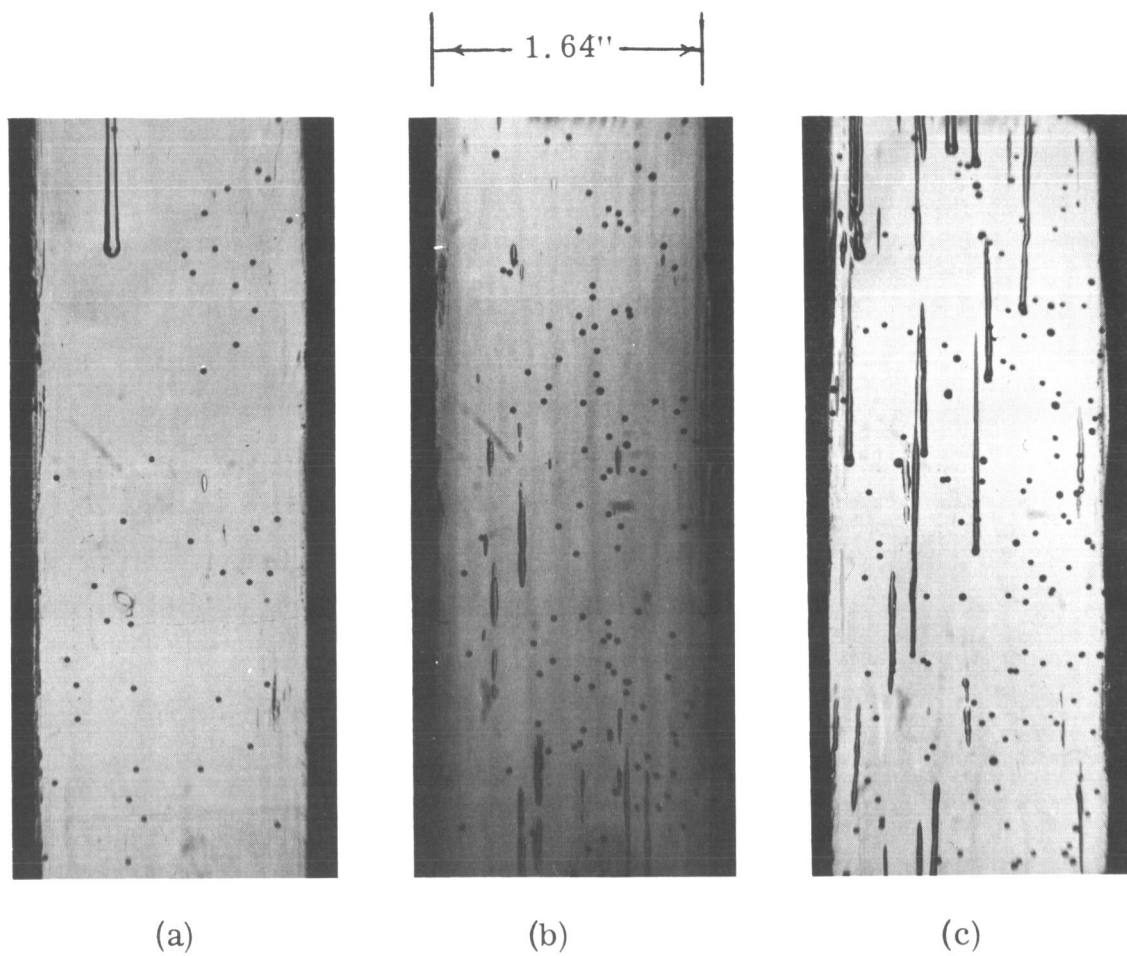


Figure 2. 4    The appearance of spray at test section, 1 second before detonation.

- (a)    Spray from 4 needles
- (b)    Spray from 12 needles
- (c)    Spray from 25 needles

Measurements of detonation velocity throughout most of the tube length are made from time measurements between pressure switches, as indicated in the Appendix. The results are shown in Fig. 2.5 where the range of variation of the velocity is indicated. Similar velocity variation with tube length is observed in all three cases. The velocity appears to taper off near the test section but suffers an abrupt change to a steady velocity in the last three feet of the tube. The sudden change is found to be due to a step in the wall of the tube where the flanges of the tube and the test section meet. Details on this are described in the next section.

At any rate comparison of the final steady velocities with theory<sup>(2, 3)</sup> shows, as can be seen in Fig. 2.6, that the experimental values are within 5-8% of the theoretical values. The leanest mixture shows a value higher than, whereas the other two mixtures indicate values lower than theoretical. It should be mentioned, however, that for the two leanest mixtures the microswitch timer (Fig. 2.1) was not available so that the difference in time when the spray photograph is taken and detonation initiation is 1-2 sec compared to the 0.25 sec when the microswitch timer is used. Thus the mixture ratio when detonation takes place could be higher than plotted on Fig. 2.6. Similarly our data here cannot be fairly compared to the data on the 940  $\mu$  drop spray in Ref. (3) because no attempt was made in Ref. (3) to precisely time the initiation of detonation. Figure 2.6 shows that the trend in the measured velocity variation with equivalence ratio seems to follow the theoretical trend very well. The velocity difference between theory and experiment can, at present, qualitatively be attributed to the drag on the drops and the tube walls and heat loss within the reaction zone as explained in section III-3.

Pressure and heat transfer measurements were made for the leanest and richest mixtures. Figures 2.7 and 2.8 show examples of the records obtained. In the case of the leaner mixture, it appears that after the initial

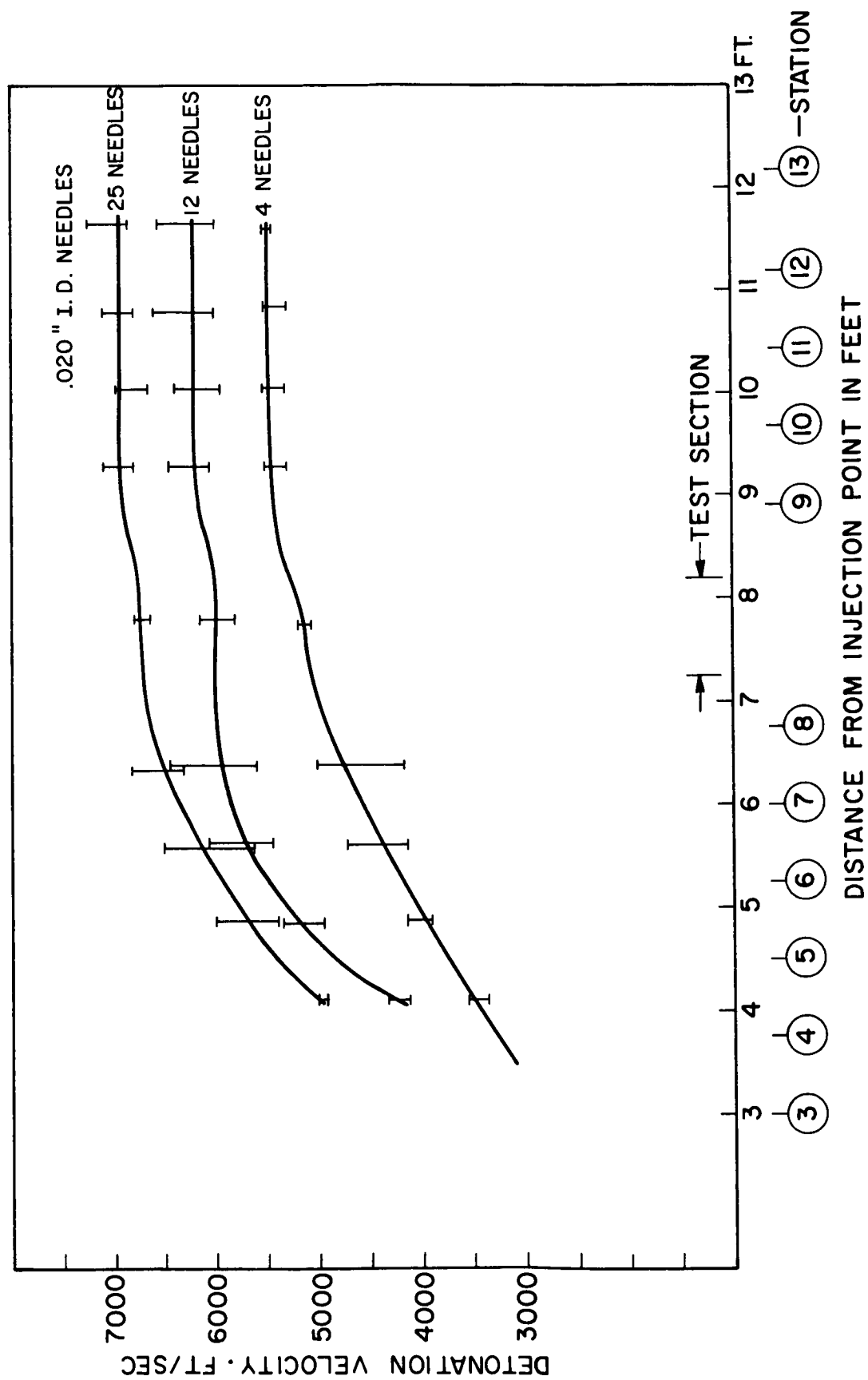


Figure 2.5 Progress of Detonation Velocity Along the Tube for 940  $\mu$  Spray.



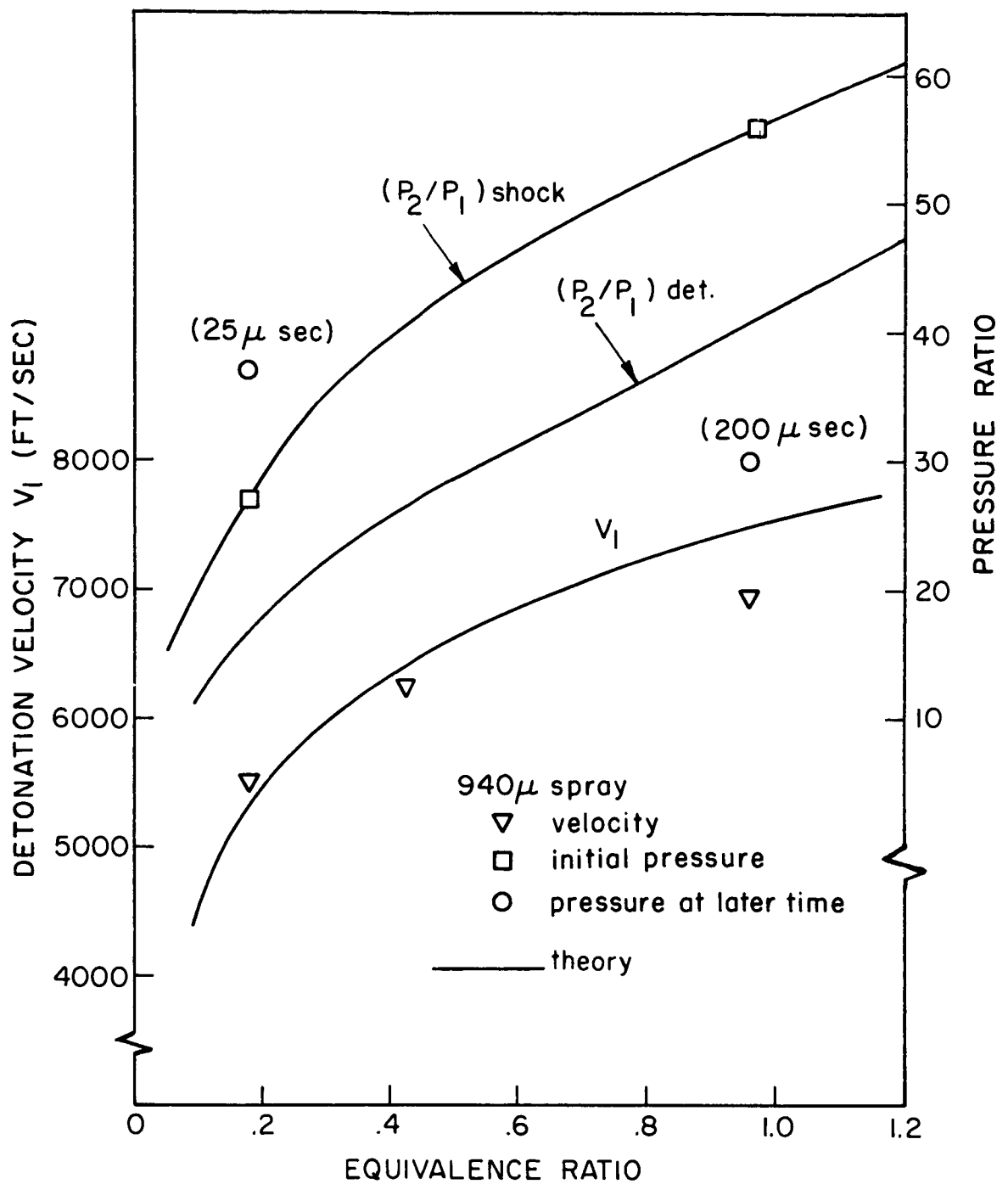


Figure 2.6 Comparison of Experimental Results on Velocity and Pressure with Theory.

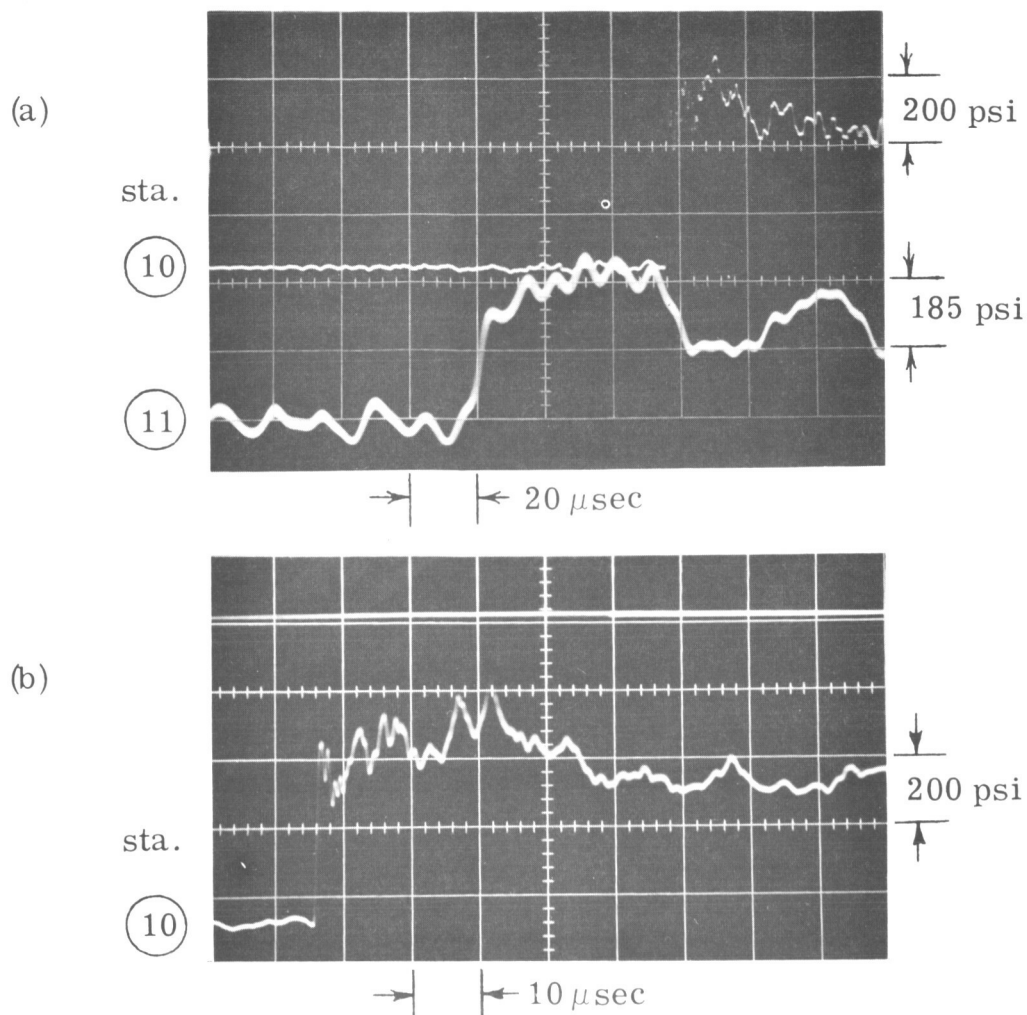


Figure 2.7 Pressure records of the detonation of  $940\mu$  diam. drops from 4 needles. (equiv. ratio = 0.18)

- (a) Run 246. Upper beam: Model 6.1 transducer with acoustic absorbing rod at station 10, triggered at station 9, 200 psi/div and 20  $\mu$ sec/div. Lower beam: Kistler Model 601A with 50 KHz output filter on charge amplifier at 10 mV/pCb, 185 psi/div and 20  $\mu$ sec/div at station 11, triggered with 200  $\mu$ sec delay at station 9.
- (b) Run 247. Model 6.1 transducer with acoustic absorbing rod at station 10, triggered with 120  $\mu$ sec delay at station 9, 200 psi/div and 10  $\mu$ sec/div.

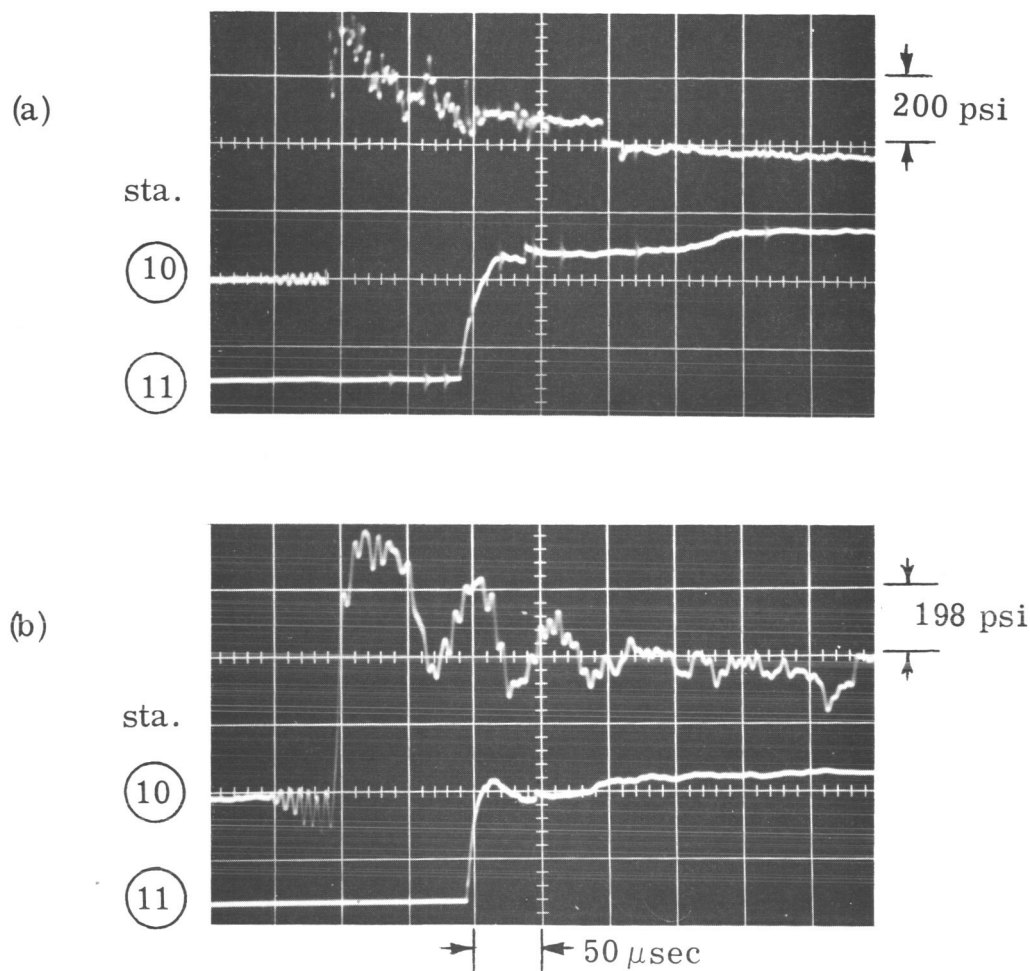


Figure 2.8 Pressure and Heat Transfer Records of the Detonation of 940  $\mu$ Drops from 25 Needles. (equiv. ratio = 0.96)

- (a) Run 268. Upper beam: Model 6. transducer with accoustic absorbing rod at station 10, triggered at station 9, 200 psi/div and 50  $\mu$ sec/div. Lower beam: heat transfer gauge No. 3 at station 11, 0.05 V/div. and 50  $\mu$ sec/div.
- (b) Run 269. Upper beam: Kistler Model 601A with 50 KHz output filter on charge amplifier at 10 mV/pCb, 198 psi/div. and 50  $\mu$ sec/div at station 10, triggered at station 9. Lower beam: heat transfer gauge No. 3 at station 11, 0.05 V/div and 50  $\mu$ sec/div.

rise in pressure to a pressure ratio of 27, there is a continuous increase in pressure until 25  $\mu$ sec after passage of the wave when the pressure ratio reaches 37; then an eventual drop-off in pressure takes place to again a pressure ratio of 27 at 45-85  $\mu$ sec. The pressures can be compared with the theoretical results as shown in Fig. 2.6. It can be seen that the original jump is higher than the theoretical C.J. pressure ratio. On the same figure, the curve labeled  $(P_2/P_1)_{\text{shock}}$  corresponds to pressure ratios of normal shocks travelling at the detonation velocity in oxygen. The initial measured pressure fits on this curve very well. This is reasonable and consistent with the accepted model of a detonation. However the rise in pressure is unexpected and may be due to secondary shocks as observed in the next section on larger drops experiments.

For the richer mixture, a pressure ratio of 56 initially and 30 at 200  $\mu$ sec after detonation passage was measured. Again from Fig. 2.6, the initial pressure rise falls on the shock pressure curve. The relatively steady pressure at 150-200  $\mu$ sec, however, is lower than the C.J. pressure. More pressure measurements are needed before any conclusions can be made.

Preliminary heat transfer records shown in Fig. 2.8 are reduced as indicated in the Appendix resulting in rates of  $\sim 10,000 \text{ Btu/ft}^2\text{-sec}$  at the front and  $\sim 2500 \text{ Btu/ft}^2\text{-sec}$  at 100  $\mu$ sec behind it. These rates for detonations at  $M \cong 7$  are much higher than those obtained for a gaseous  $2\text{H}_2\text{-O}_2$  detonation which travels at  $M \cong 5.3$ .

### 3. Detonation of 2600 $\mu$ Diameter Drops.

The size of the droplets in the combustion tube was increased to 2600  $\mu$  diameter in order to investigate the upper limit on drop size and at the same time insure that no wall wetting occurred. With this drop size it is possible to obtain a mixture ratio in the range of interest with only one stream of drops. And since these drops are separated further than the 940  $\mu$  diameter drops due to the lower operating frequency of the generator and the higher terminal velocity of the drops, better resolution of the drop dynamics in the reaction zone could be obtained.

A needle plate with one 0.063 in. I.D. tube was used in the drop generator which was operated at 116 Hz. The mass flow was measured periodically by collecting a known volume of fuel in a known time, and the drop diameter was thus calculated to be from 2530 to 2630 microns depending on the pressure setting in the generator. The precise pressure at which the best formation of the drops was possible varied slightly from day to day, but generally the size of the drops used was close to 2600  $\mu$  in diameter. The drops leave the generator with a velocity of about 1.64 ft/sec and spaced .17 in. apart thus resulting in a mixture with an equivalence ratio of 2.5. The drops then accelerate to a terminal velocity of 18 ft/sec with a measured average separation distance of 1.84 in. at the test section and 1.89 in. at 3 ft below the test section which results in an equivalence ratio of 0.23. A spark photograph of the back-lighted drops such as Fig. 2.9, was taken 1 sec before each run to insure that the drops were properly set up. The test procedure was the same as described in section I-1.

It is surprising that this configuration of drops would detonate at all, but no difficulty was experienced in initiating the process. When air was used instead of oxygen, combustion of this size drops could not be initiated, however.

Framing camera photographs and pressure records of the detonation were taken first. The optical arrangement is shown in Fig. 2.10. A Fastax camera model WF3 using 16 mm Dupont 931A reversal film at f/4 was positioned

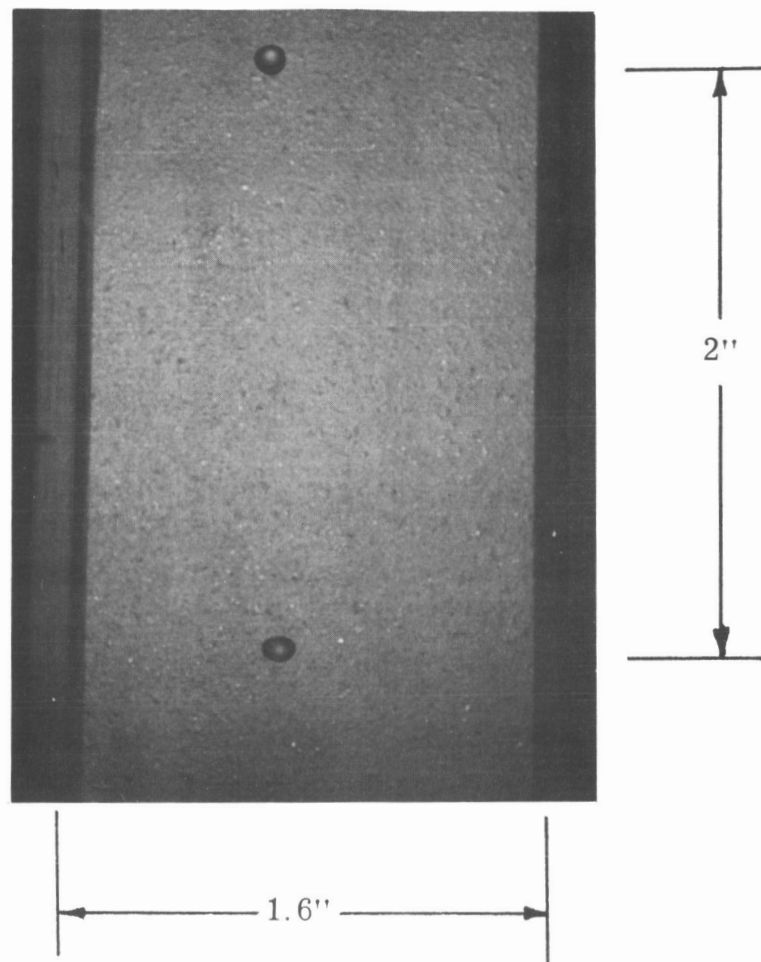


Figure 2.9 Photograph of  $2600\ \mu$  Drops in the Combustion Tube.

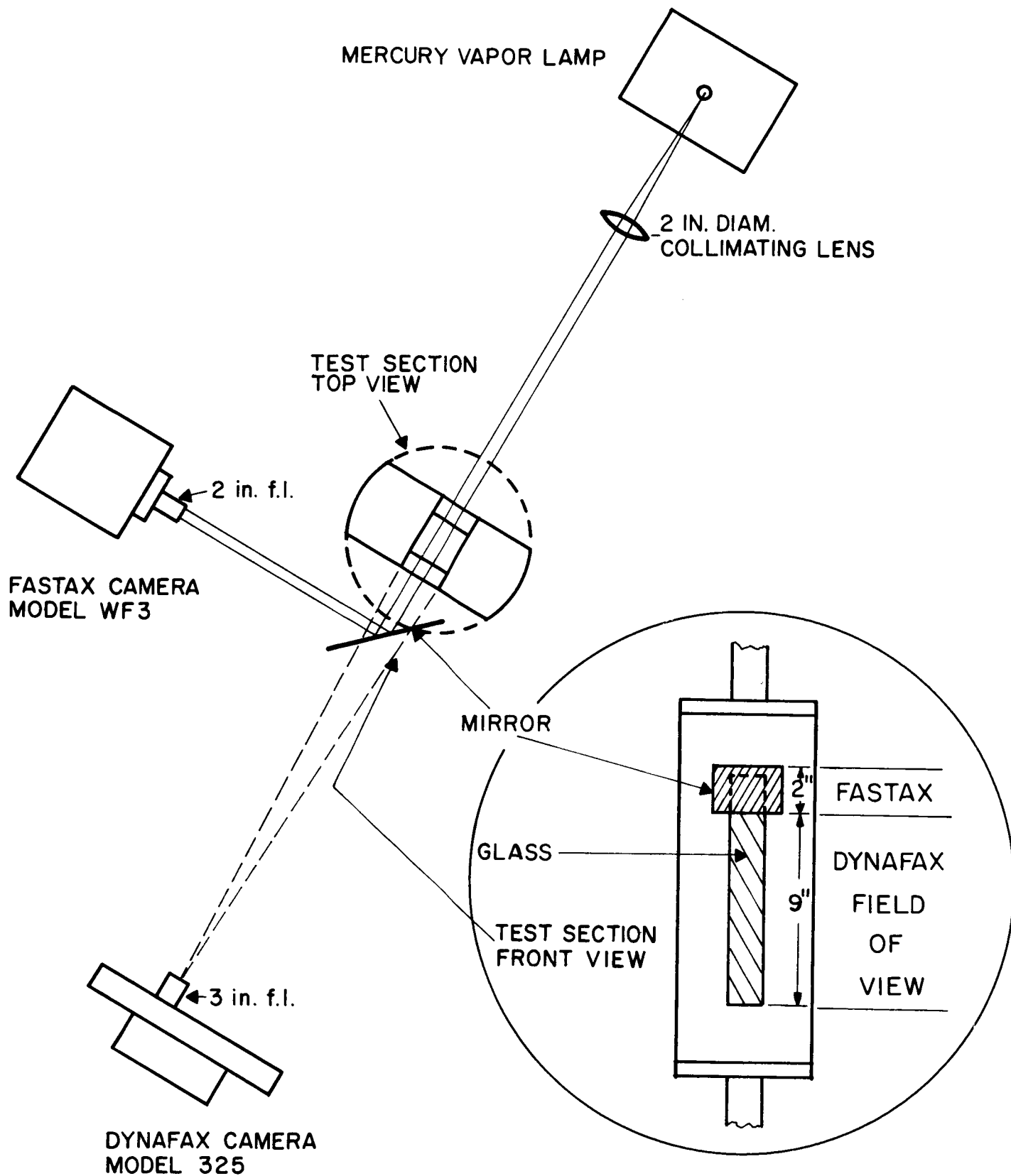


Figure 2.10 Schematic of the Optical System for the Framing Camera Photographs.

to view the falling drops by means of back light over a small portion of the test section. In this manner the exact position of each drop at the time of passage of the detonation could be reconstructed. A Dynafax model 326 framing camera using 35mm Tri-X film was focused on the remainder of the test section and recorded the self-luminous light of combustion. Framing camera photographs and pressure records from Kistler transducers located before and after the test section are shown in Fig. 2.11 for a representative test. As verified by the Fastax photographs, the drops were well centered and separated slightly less than 2 in. apart, so that there were 5 drops in the field of view. In the framing camera photographs, the detonation wave is moving from right to left in each frame while the time sequence is from left to right as indicated. The time between frames is  $95.2 \mu\text{sec}$ . Since shock waves do not register in a self-luminous photograph, the first indication of combustion is taken as the start of the reaction zone. The luminosity is at a relatively low level during the first 4 frames ( $380 \mu\text{sec}$ ) compared to frames 5-10; the significance of this will not become apparent until the streak photographs are discussed. The velocity of propagation for run 171, as obtained from Fig. 2.11(b), is 2900, 3100, 3200, and 3600 ft/sec between stations 6-7, 7-8, 8-9, and 9-10, respectively. The peak pressures as measured by this system varied from 135 psia at station 8 to 175 psia at station 10. There is apparently a somewhat stronger acceleration of the detonation after the test section, as will be discussed later.

Since it appears that the reaction zone of the detonation is extended many orders of magnitude over that of a gaseous detonation, one would like to examine the gasdynamic structure of this detonation; that is, to describe the features of the leading shock front, the droplet breakup, the chemical reaction zone and the trailing rarefaction. Streak photographs, special pressure transducers, and heat transfer gauges have been used for this purpose.



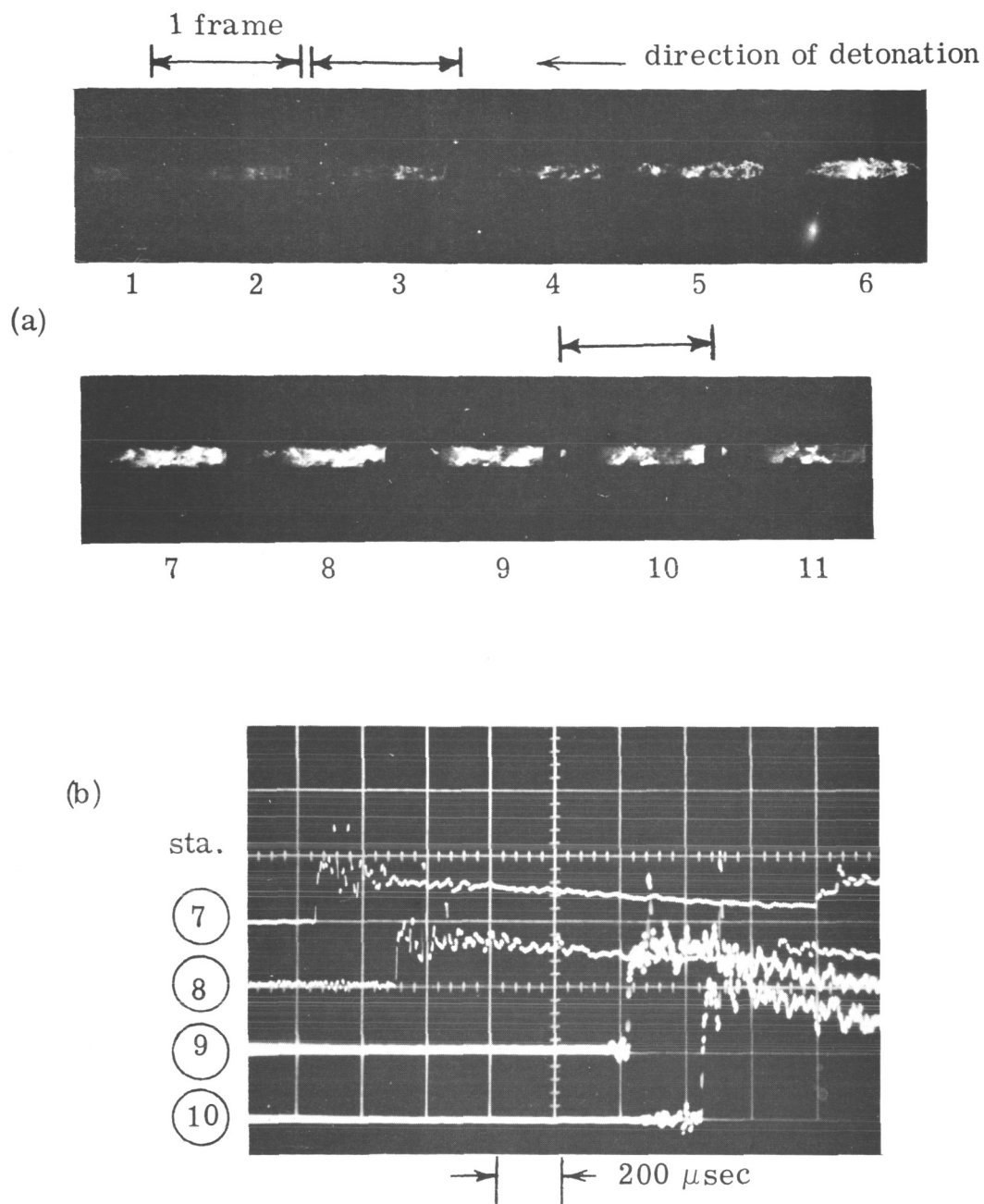


Figure 2.11 Framing Camera Photographs and Pressure Record of the Detonation of  $2600\ \mu$  Drops. Run 171.

- (a) Dynafax Model 326,  $f\ 2.8$ ,  $2.6\ \mu\text{sec}$  exposure,  $95.2\ \mu\text{sec}$  between frames.
- (b) Kistler pressure transducers with 50 KHz output filter on charge amplifier at  $10\ \text{mV/pCb}$ ,  $200\ \mu\text{sec/div}$ , triggered at station 6.

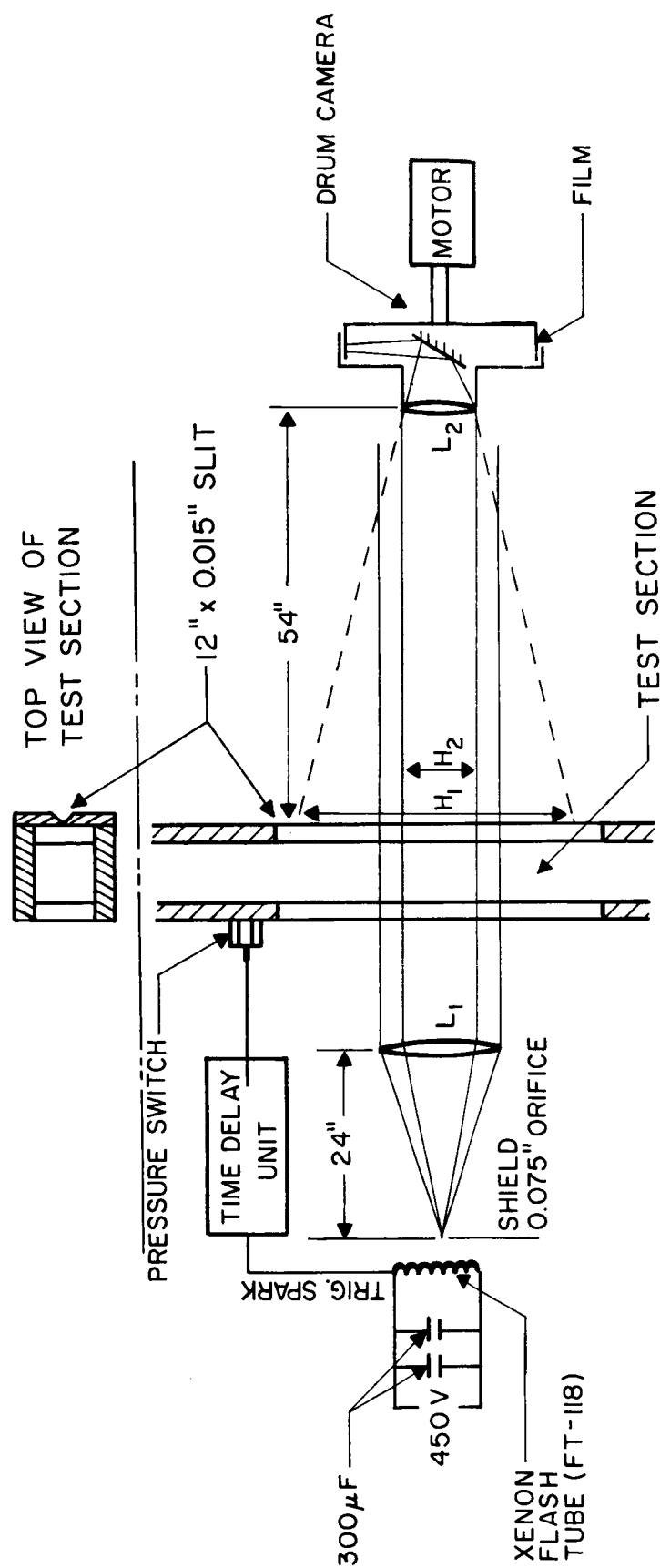
For beams starting at top:

sta. 7, Model 603,  $143\ \text{psi/div}$   
 sta. 8, Model 603,  $132\ \text{psi/div}$   
 sta. 9, Model 601A,  $95\ \text{psi/div}$   
 sta. 10, Model 601A,  $80\ \text{psi/div}$

The streak photographs of the  $2600\ \mu$  diameter detonations will be discussed first. A schematic diagram of the optical arrangement is shown in Fig. 2.12. The drum camera, which consisted of the motor and drum of the Dynafax model 326 with a new lens-cover plate-prism assembly, was focused on a 0.015 in. slit which was positioned at the center of the test section window. Collimated light from a Xenon flash tube with a duration slightly less than one rotation of the drum was directed through the slit as indicated, to yield a shadowgraph effect over a small portion of the test section.

In general the runs were qualitatively repeatable in all but 3 out of 45 cases. Three of the runs, which occurred interspersed between normal runs in the course of several days, exhibited highly unstable behavior on both the pressure transducers and the streak photographs. As shown in Fig. 2.13(a), the shock runs far ahead of the combustion and at the position of the photograph is decaying, while it appears that a new leading shock is forming at the edge of the flame zone. The reason for this behavior in such a few cases is not known.

The streak photograph of Fig. 2.13(b) is representative of "normal" behavior. The vertical bright line is an image of the slit. The three fine horizontal dark lines are reference wires placed across the slit at 2 and 3 in. intervals. Increasing distance from the drop generator is in the positive x direction. The dark, nearly horizontal line in the band of collimated light is a drop which happened to be directly in the slit. The leading shock front is travelling at a velocity of 3350 ft/sec. This velocity was obtained from pressure transducers and not from the streak film directly because the speed of the camera drum could not be monitored. All other velocities on the streak photographs may be obtained relative to the initial shock velocity by measuring the tangent of the angle between the horizontal and the line of disturbance. The leading shock sweeps over the drops, accelerating and disintegrating them.



NOTE:

L<sub>1</sub> is 5" Diam. 24" f.l. Lens

L<sub>2</sub> is 1-13/16" Diam. 7" f.l. Lens

H<sub>1</sub> is Field of View of Direct Photography = 10 Inches

H<sub>2</sub> is Field of View of Shadow Photography = 1-13/16 Inches

Figure 2.12 Schematic of the Optical System for the Streak Photographs.

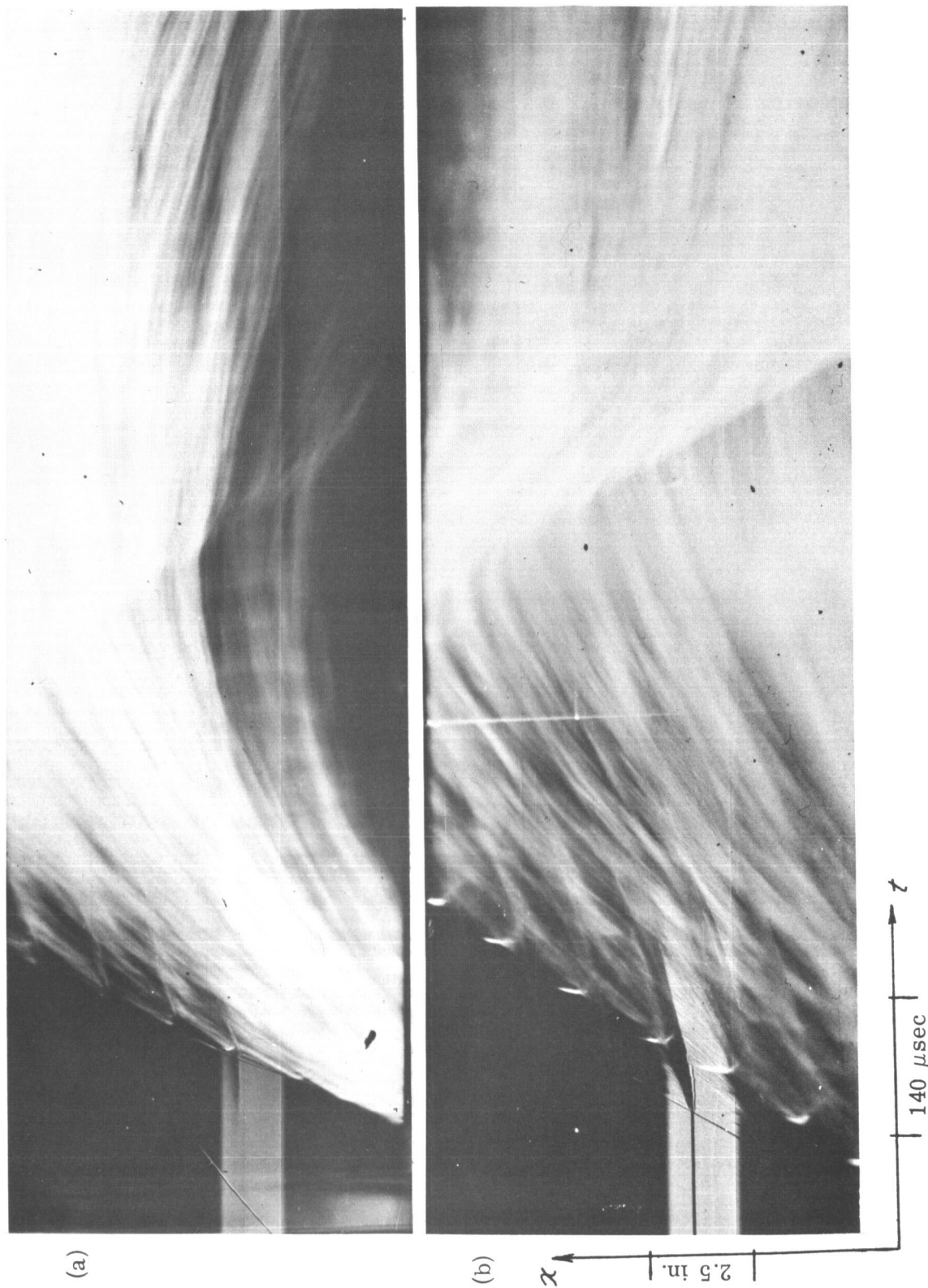


Figure 2.13 Combined Self-Luminous and Shadow Streak Photographs of  $2600\ \mu$  Diameter Drop Detonation.

(a) Run 278, unstable case; (b) Run 279, normal case with induced retonation below the optical section.

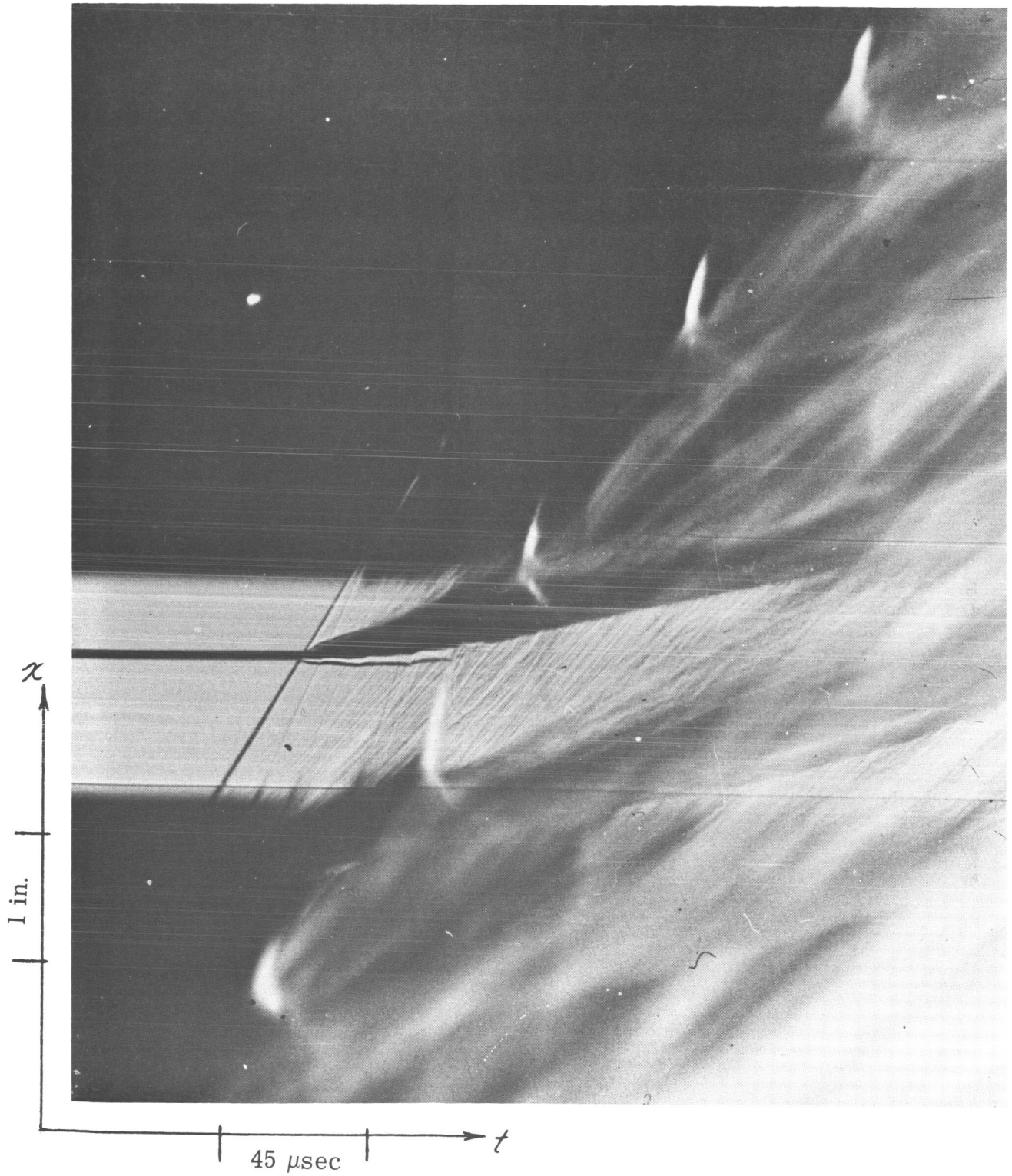


Fig. 2. 13 (c) Enlarged view of Run 279.

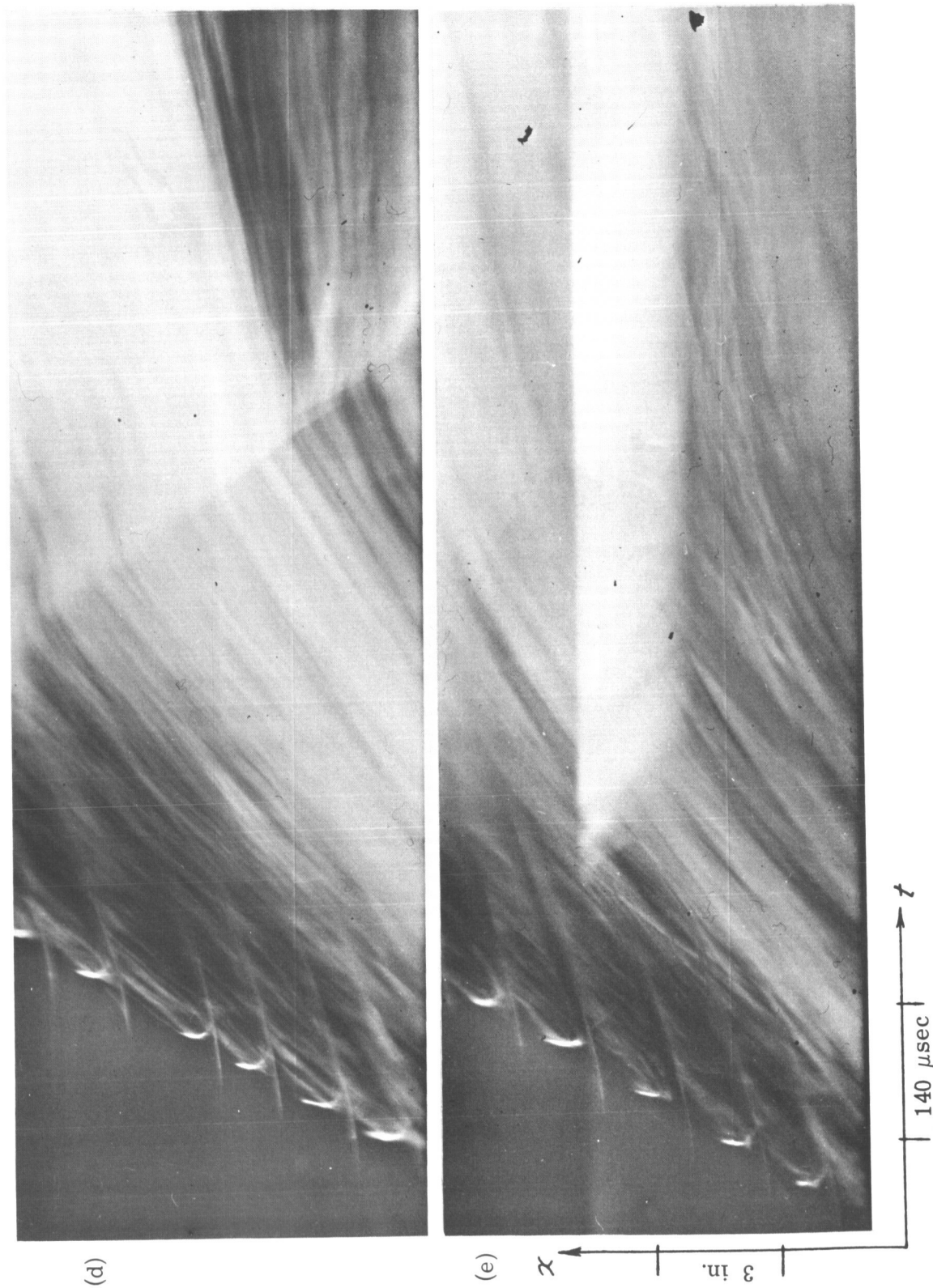


Fig. 2.13 (d) Run 299. Normal case with induced retonation above and below optical section.  
 (e) Run 301. Normal case with induced retonation above optical section.



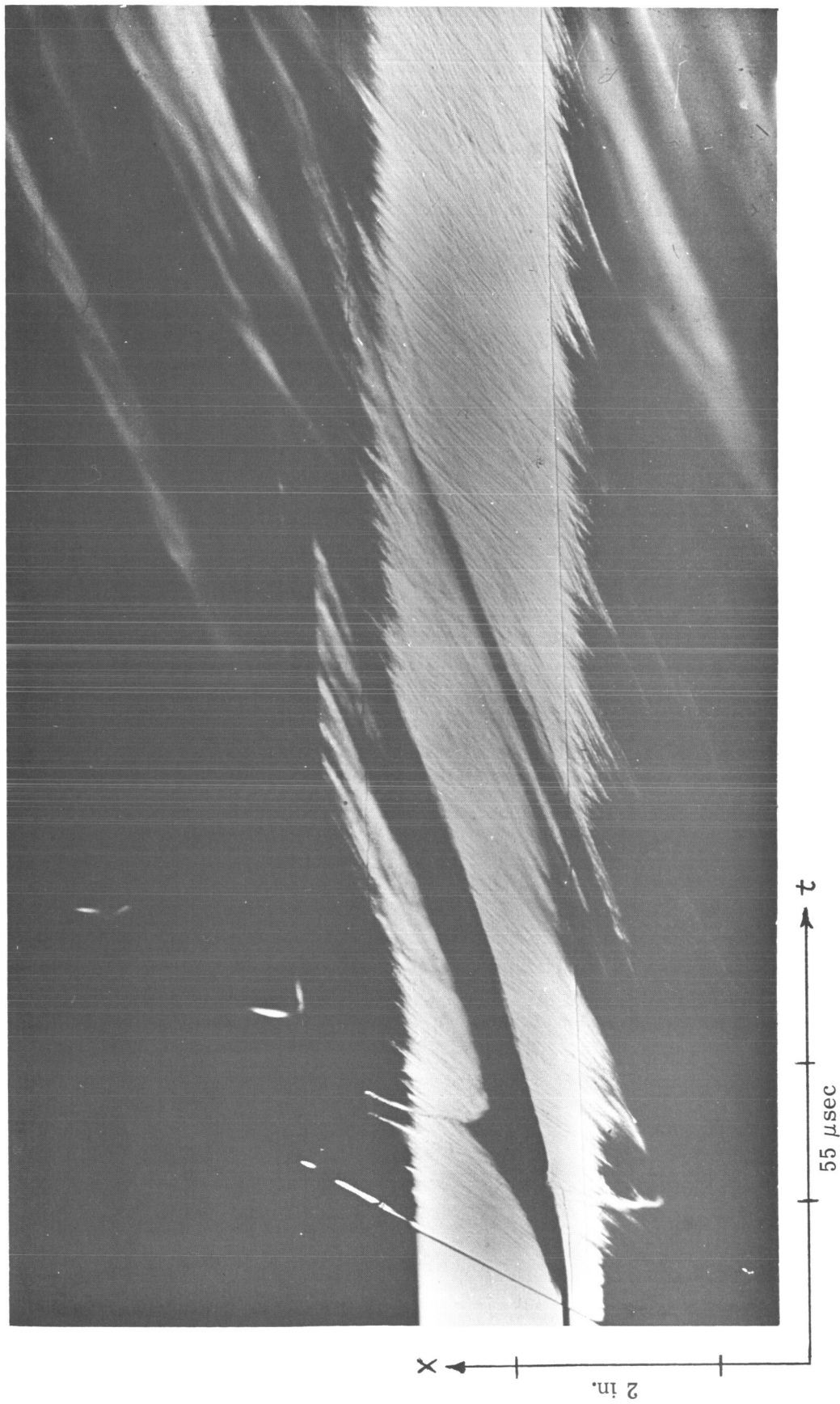


Fig. 2.13(f). Run 280. Exposure to emphasize the trajectory of the drops.

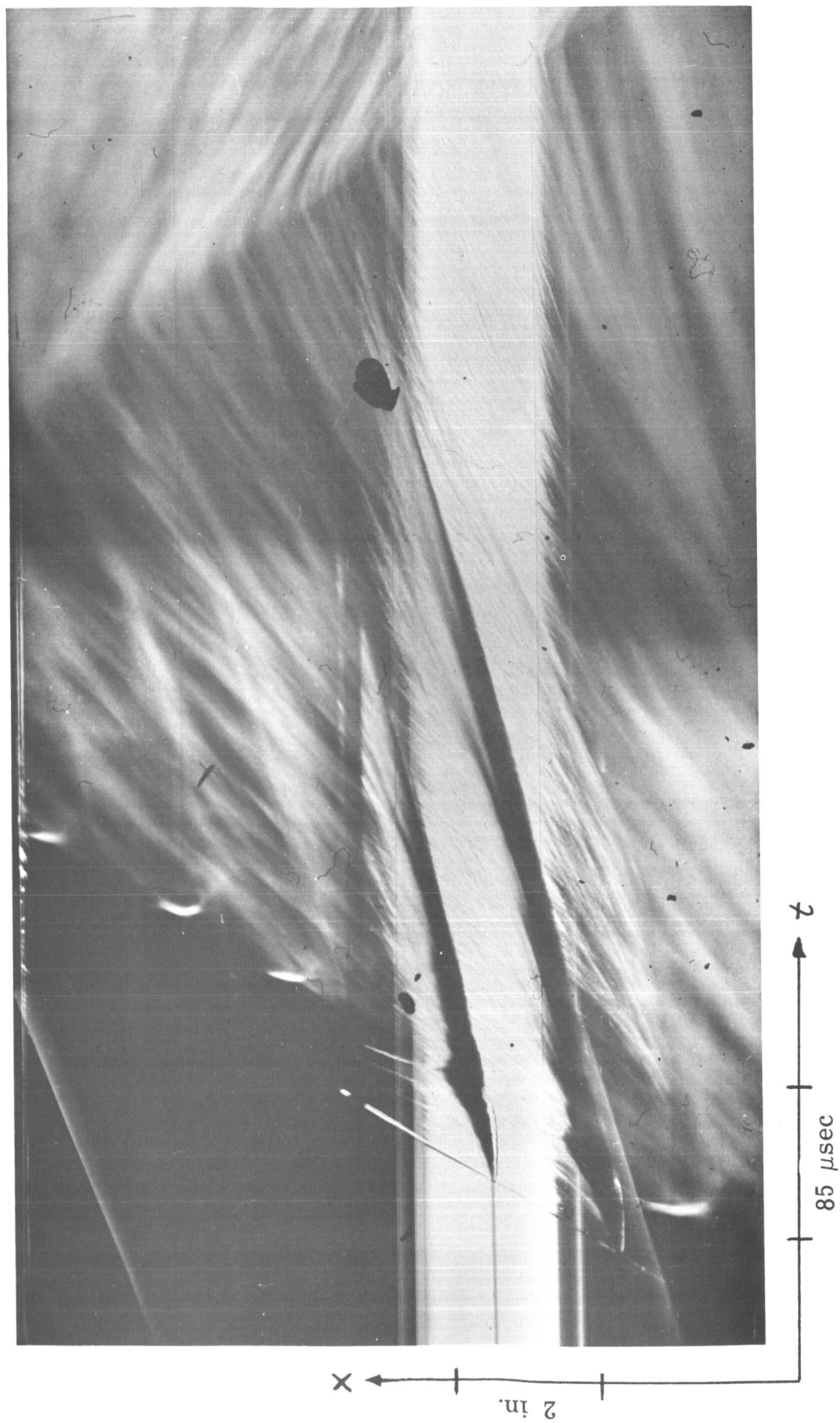


Fig.2.13(g). Run 289. Exposure to emphasize the trajectory of the drops.



The light from combustion lags the initial shock by about  $65 \mu\text{sec}$ . The discrete very intense spots of luminosity at the start of the combustion zone can be associated with the position of each drop and are interpreted as a rapid combustion of the microspray wake which is stripped from the parent drop.

Figure 2.13(c) provides an enlarged view of the drop dynamics. Upon collision with the initial shock, the drop in the collimated light instantaneously undergoes a deformation of the front surface so that the drop appears about 15% narrower due to initial flattening (see Chapter IV). The wake from the drop starts developing immediately and a bow shock is formed in front of the drop. The separation between the bow shock and the drop increases with time for two reasons—the drop is deforming laterally, and the relative velocity between the drop and the convective flow is decreasing due to the acceleration of the drop. The Mach number of the convective flow is 1.40 assuming normal shock conditions and the Reynolds number based on drop diameter is  $2 \times 10^5$ . The front of the drop is oscillating somewhat behind the bow shock. The wake grows to about 1 in. long and then is violently consumed. As seen in Fig. 2.13(c) and (f) the wake combustion produces a local shock wave and this shock terminates the bow shock of the drop just downstream. Four secondary shock waves, which are apparently generated by the combustion process, are seen in Fig. 2.13(c) catching up to the leading shock. When one normal shock overtakes another, a transmitted shock which is stronger than either but less than the combined strength of both occurs. And the reflected wave is a rarefaction for  $\gamma < 5/3$  which is true in our case. In this case the secondary shock waves could be localized but nevertheless this provides the mechanism for the propagation of the leading shock front. The strength of the secondary shocks are analyzed in Table I along with other velocities of interest. The velocities of the secondary shocks vary from 4900 ft/sec near the leading shock to 7800 ft/sec near the wake combustion. The Mach number of these shocks was calculated assuming a constant speed of sound behind the initial shock, and also by assuming the secondary shocks to be a series of normal shocks. The former assumption

TABLE I. ANALYSIS OF STREAK PHOTOGRAPHS

Run	Disturbance	$\alpha$ (degrees)	V (ft/ sec)	M
279	Initial shock	58	3350	3.15
	First secondary shock	66	4920	(2.75)
	Second secondary shock	68	5200	(2.90)(1.87)
	Third secondary shock	75	7830	(4.36)(2.24)
	Fourth secondary shock	75	7830	(4.36)(1.50)
	Speed of sound behind initial shock	41	1790	
	Convective flow behind initial shock	50	2510	1.40
	Chapman-Jouguet speed of sound	43	1930	
	Chapman-Jouguet convective flow	34	1420	0.74
	Retonation wave	-60	-3620	
	Drop in collimated light:			
	Free fall velocity	0.5	18	0.017
	Absolute velocity when bow shock terminates	6.5	250	
	Absolute velocity after wake combustion	2.7	100	
289	Initial shock	60	3350	3.15
	Shock from wake combustion	69	5170	(2.89)
	Speed of sound behind initial shock	46	1790	
	Convective flow behind initial shock	52	2510	1.40
	Chapman-Jouguet speed of sound	45	1930	
	Chapman-Jouguet convective flow	36	1420	0.74
	Retonation wave	-60	-3350	
	Drop in collimated light:			
	Absolute velocity when bow shock terminates	11	360	
	Absolute velocity after wake combustion	4	135	
299 and 301	Velocity near end of breakup	16.5	660	
	Initial shock	60	3750	3.54
	Speed of sound behind initial shock	43	1940	
	Convective flow behind initial shock	53	2880	1.48
	Chapman-Jouguet speed of sound	45	2140	
	Chapman-Jouguet convective flow	37	1610	0.75
	Retonation wave (Run 299)	-54	-3000	

would be more representative of very localized secondary shocks while the latter assumption would represent secondary shocks which follow one behind the other over a larger area. For example, as indicated in Table I, the fourth secondary shock is traveling at a Mach number of 4.36 assuming a constant speed of sound behind the initial shock front, but assuming a series of secondary shocks the fourth secondary shock is traveling at Mach 1.5. Since the pressure jump across the secondary shocks will be different for the two cases, this information is of interest in interpreting the records from the pressure transducers. It should be explained that some shock structure can be seen outside the band of collimated light due to slight deflection and scattering of the parallel beam.

Returning to Fig. 2.13(b), it is apparent that the luminosity continues at the same general level until interrupted by a rearward moving discontinuity; at that point the luminosity increases and at least some of the burning particles change direction and move back up the tube. The velocity of this rearward moving wave as determined by the slope is 3600 ft/sec. This wave is also apparent in the pressure and heat transfer gauge records. The origin of the disturbance is traced to be at the joint between the optical section, which has square corners, and the lower section of the combustion tube, which is structural tubing, with rounded corners. In addition to this mismatch there was a slight misalignment. It was found that the strength of this rearward moving wave could be decreased by providing gradual transition from the square to the rounded corners. An explanation for this effect is that misalignment of the tube produces standing oblique shocks in the convective flow behind the leading shock front of the detonation. As a partially shattered drop flows through the standing shocks, combustion is stimulated with the result that pressure waves are sent out in all directions. The forward moving shocks reinforce the leading detonation shock front while the rearward moving shocks converge and are accelerated by unburned fuel in the reaction zone of the detonation. Thus we have an induced "retonation" in the analogous sense to what occurs at the transition to detonation in a gas.

As further proof of the ability to induce retonation in this system, a 14 in. long section of tube was added just above the optical section and a plate 1/4 in. thick with a 2-1/4 in. diameter hole was inserted between the flanges of the original combustion tube and the 14 in. section. In this way a retonation could be triggered upstream of the test section with the result that the detonation velocity was increased 400-600 ft/sec in the optical section. Figure 2.13(d) and (e) were made with the induced retonation above the optical section. In Fig. 2.13(d) the joint below the optical section was improved as best that could be done with the structural tubing. The retonation still exists but is not strong enough to reverse the flow. In Fig. 2.13(e) the retonation was eliminated by using a machined section below the optical section. The band of luminosity in the center of the photograph is double exposure due to the exhaust from the bottom of the test section and should be neglected.

In Fig. 2.13(d) and (e) streaks of light before the bright combustion of the wake are observable. Here the velocity of propagation has increased from 3350 to 3750 ft/sec and this causes burning of the drop in the stagnation region just behind the bow shock. The stagnation temperature behind the bow shock is estimated to be 1550<sup>o</sup>F in Fig. 2.13(c) and 2000<sup>o</sup>F in Fig. 2.13(d). The stagnation point burning appears to last at least 130  $\mu$ sec; it becomes less distinct at the point where the bow shock is destroyed.

Additional velocity information associated with the reaction zone of the two phase detonation with the aid of the streak photographs is shown in Table I. The streaks immediately behind the initial shock in Fig. 2.13(b), for example, follow quite closely the estimated convective flow velocity behind a normal shock. As heat is added the angle of the streaks of luminosity gradually decrease indicating a decrease in the convective velocity. In the classical theory of detonation the convective velocity decreases until the fluid is moving away from the initial shock front with a sonic velocity relative to the initial shock. At this point the reaction zone is terminated and a trailing rarefaction begins. From the streak photographs it is difficult to distinguish

between heat addition and a rarefaction wave in terms of the angle of the flow, and thus it is not possible to verify the classical model for this case. In order to do this it is necessary to follow one streamline through the entire process. Nevertheless one is tempted to try, and in Fig. 2.13(d) it appears that the angle of the flow is about  $32^{\circ}$  near the end of the reaction zone which yields a velocity of 1350 ft/sec compared to a Chapman-Jouguet velocity of 1610 ft/sec which was calculated from Eq. 2.12 with  $C_D = 0$ . The pressure and heat transfer records, to be presented later, are more of an aid in determining the extent of the reaction zone.

The displacement of the drop as a function of time after passage of the leading shock front and the complete disintegration time can also be obtained from the streak photographs. In Fig. 2.13(f) and (g) the collimated light is more intense, thus emphasizing the high density regions of liquid. Also Fig. 2.13(f) was taken with High Speed Ektachrome (ASA 160) rather than the usual Tri-X Pan (ASA 400). The time required for complete disintegration of a  $2600\ \mu$  diameter drop due to a two-phase detonation propagating at 3350 ft/sec, as obtained from Fig. 2.13(f) and (g), is approximately 500  $\mu$ sec. It is interesting to note that at this time the velocity of the liquid is only 660 ft/sec which is 760 ft/sec below the theoretical Chapman-Jouguet velocity and 1850 ft/sec below the initial convective velocity. The displacement data, which was obtained from Fig. 2.13(b,f,g), is shown in Fig. 2.14. During the first 100  $\mu$ sec of the breakup process the velocity of the leading edge of the drop (obtained from the slope of the x-t curve) fluctuates due first to the combustion of the wake of the previous drop and then to the combustion of the parent wake. A general acceleration of the drop is noted during the first 100  $\mu$ sec. Between the period of 100-300  $\mu$ sec the velocity of the drop is remarkably constant. The acceleration of the drop is apparently reduced by at least an order of magnitude during this period. It is felt, however, that the shear stress of the drop on the fluid does not decrease but rather that the pressure at the rear of the drop increases due to combustion of the wake. For the purpose of

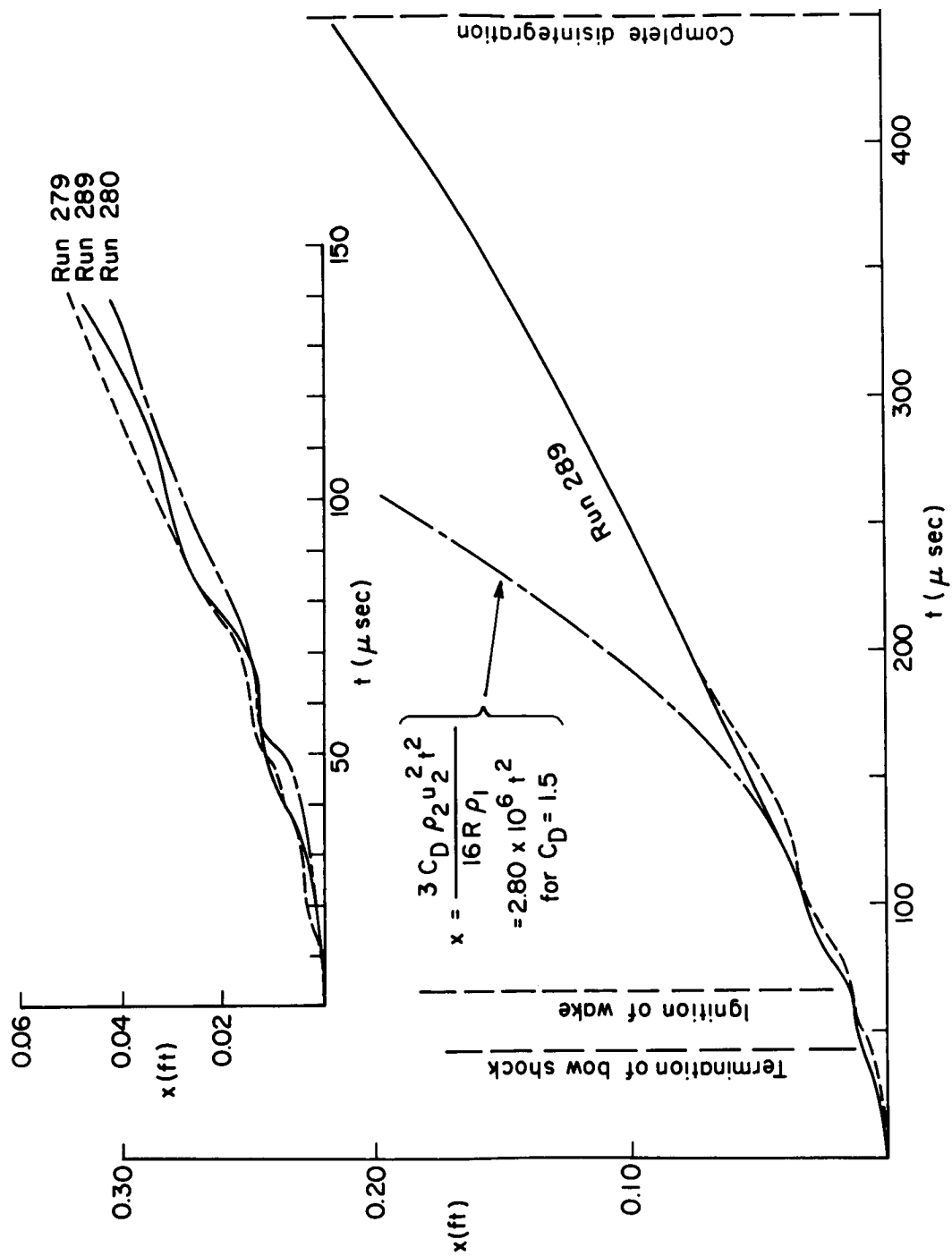


Figure 2.14 Displacement of 2600  $\mu$  Diameter Drop vs. Time After Passage of Detonation Front.

comparison the displacement due to a constant acceleration of a constant mass drop is also plotted assuming that the relative velocity between drop and the fluid remains at the convective flow behind a normal shock. The area of the drop was based on the initial projected frontal area. A drag coefficient,  $C_D = 1.5$  gave the best agreement in the early stage but large deviation can be observed at a later stage.

There appears to be a considerable difference between the behavior of the drops described above and certain features observed in our shock tube studies of inert drops. In the first place the data obtained in the shock tube studies indicates a break up time about 60% of that obtained from Fig. 2.13. However the difficulty in interpretation and the difference in experimental techniques make this comparison difficult. Secondly, the shock tube studies indicate that the drop undergoes approximately constant acceleration, during the entire disintegration process while from Fig. 2.13 the velocity is nearly constant during large portions of the breakup process. The acceleration of inert drops is about 75% higher than that experienced by the burning drop at the early stage of breakup within the two phase detonation. The shock displacement data in section IV-2 can be shown to fit more closely to an average  $C_D$  of 2.6 than of 1.5. Another difference to be noted is that near the end of breakup the inert drop in the shock tube has reached 80 to 90% of the convective flow velocity while the drop in the two phase detonation has reached only 47% of the theoretical C.J. convective velocity or 36% of the convective velocity behind the initial shock front. It is of interest to note that the maximum displacement of the detonating drop, as indicated in Fig. 2.14 is .22 ft, while using a constant acceleration with a  $C_D$  of 2.6 would predict a total displacement of 1.2 ft.

The pressure transducer records of the 2600  $\mu$  diameter drop detonations will be presented next. Figure 2.15 is shown for the purpose of indicating the difficulty of measuring the pressure in the reaction zone of a detonation with

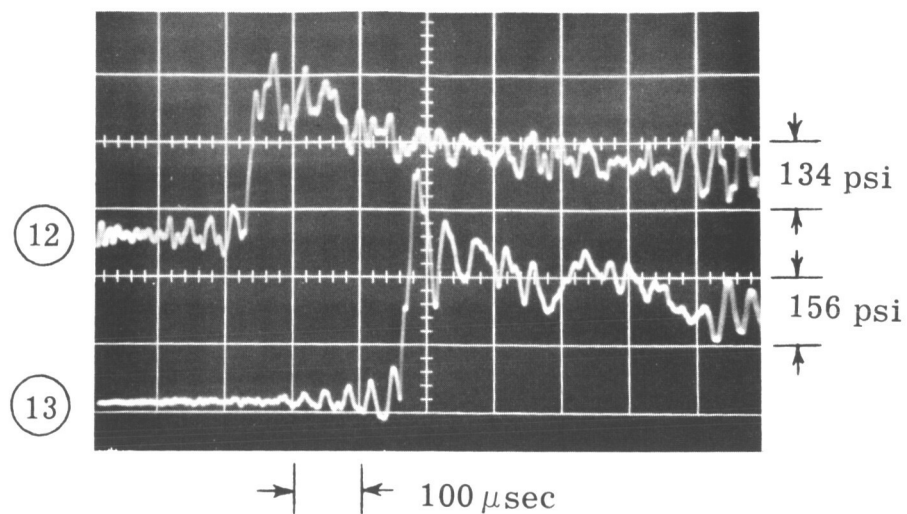


Figure 2. 15 Pressure record of  $2600\mu$  diameter droplet detonation using Kistler pressure transducers Model 603 with 50 KC output filter on charge amplifier at 10 mV/pCb. Run 295. 100  $\mu\text{sec}/\text{div}$  triggered at station 11. Upper beam: station 12, 134 psi/div. Lower beam: Station 13, 156 psi/div.



Kistler instrumentation. A filter has been used to suppress frequencies above 50 KHz, however, it is readily apparent that the dynamic response of the transducer overshadows the structure of the reaction zone. Further details concerning the pressure instrumentation are given in the Appendix.

Pressure records obtained with the lead metaniobate transducer which has the tin acoustic absorbing rod are shown in Fig. 2.16 for various positions along the combustion tube. Trace (a) shows that the pressure pulse due to the driver alone is about 10 psi at station 2. This pulse decays further as it progresses down the tube. With the drops and oxygen gas present, detonation is initiated. Traces (b) and (c) show that the pressure of the leading shock front jumps to 60 and 50 psi respectively at station 2. Furthermore a series of secondary pressure spikes occur about  $200\ \mu\text{sec}$  behind the leading shock. These pressure spikes rise at least 100 psi above the local static pressure and are considered to be caused by the local combustion of the wake of the individual drops, which at this station are spaced 1 to 2 cm apart. This process can provide a powerful means of accelerating the leading shock front. At station 4, as in (d), the pressure behind the initial shock is 100 psig, and the secondary shocks occur sooner and rise about 50 psi above the local static pressure. The time between secondary shocks is greater because the drops are further apart. The velocity between stations 3 and 4 is 2680 ft/sec. At station 8, as in (e), the initial pressure rise is 150 psi and the velocity 3120 ft/sec. The secondary shocks are apparent as well as what was determined to be the induced retonation. At station 12, as in (f), the detonation has travelled 11 ft and experienced one induced retonation; the initial pressure rise is 212 psi and the velocity 3850 ft/sec. It is felt that the majority of the pressure oscillations are in the gas rather than the transducer because of the flat response of the transducer to a pure normal shock. A reflected shock from the end of the tube appears in (f) 1 msec after the leading shock front.

The velocity of propagation as a function of distance from the driver can be obtained from the pressure records in two ways. First, the time from

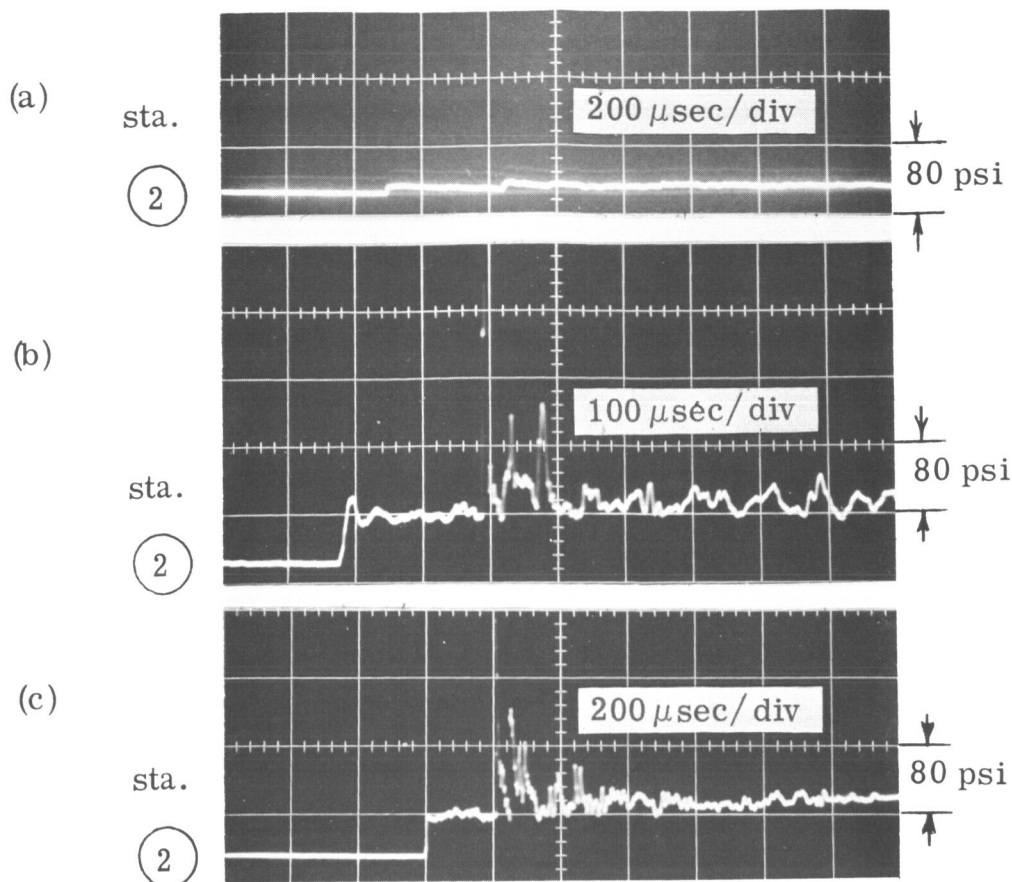


Fig.2.16 Pressure and heat transfer records of  $2600\mu$  diameter droplet detonations using pressure transducers with an acoustic absorbing rod and platinum thin film resistance gauges.

- (a) No drops, driver (30 in. Hg  $2H_2 + O_2$ ) fired into 1 atm air. Pressure transducer No. 6.5 at station 2, 80 psi/div and 200  $\mu$ sec/div, triggered at station 1.
- (b) Run 296. Pressure transducer No. 6.5 at station 2, 80 psi/div and 100  $\mu$ sec/div, triggered at station 1.
- (c) Run 294. Pressure transducer No. 6.5 at station 2, 80 psi/div and 200  $\mu$ sec/div, triggered at station 1.

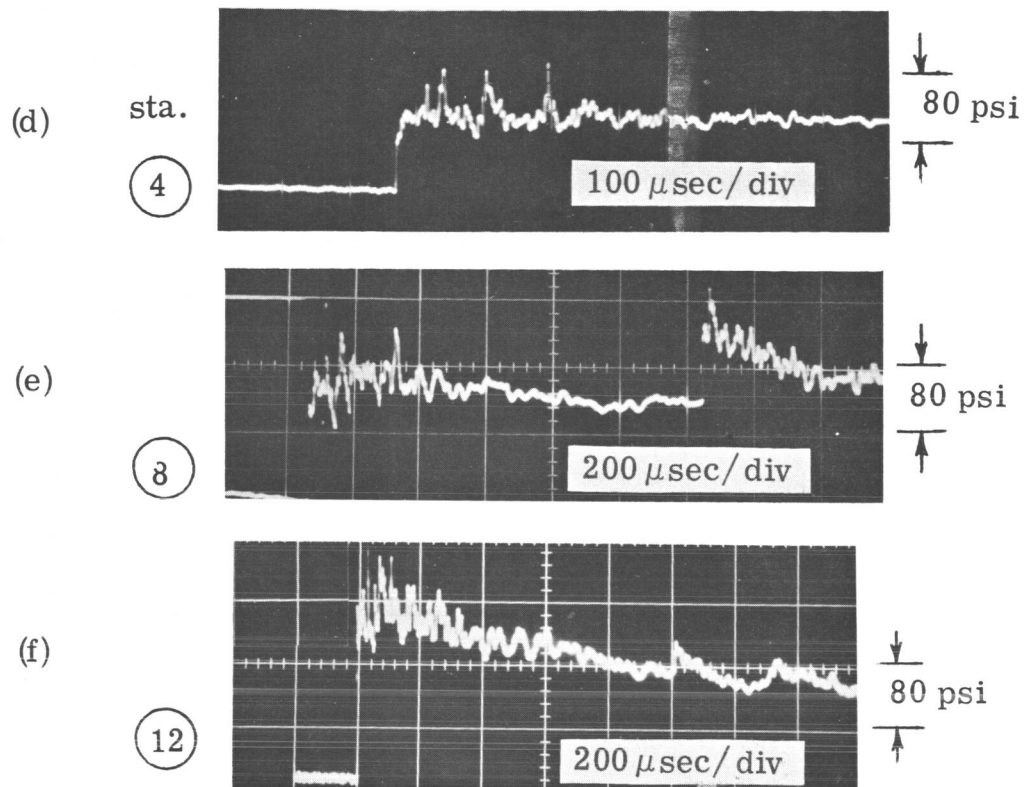


Fig. 2.16

- (d) Run 293. Pressure transducer No. 6.5 at station 4, 80 psi/div and 100  $\mu\text{sec}/\text{div}$ , triggered at station 3.
- (e) Run 285. Pressure transducer No. 6.5 at station 8, 80 psi/div and 200  $\mu\text{sec}/\text{div}$ , triggered at station 7.
- (f) Run 287. Pressure transducer No. 6.5 at station 12, 80 psi/div and 200  $\mu\text{sec}/\text{div}$ , triggered at station 11.

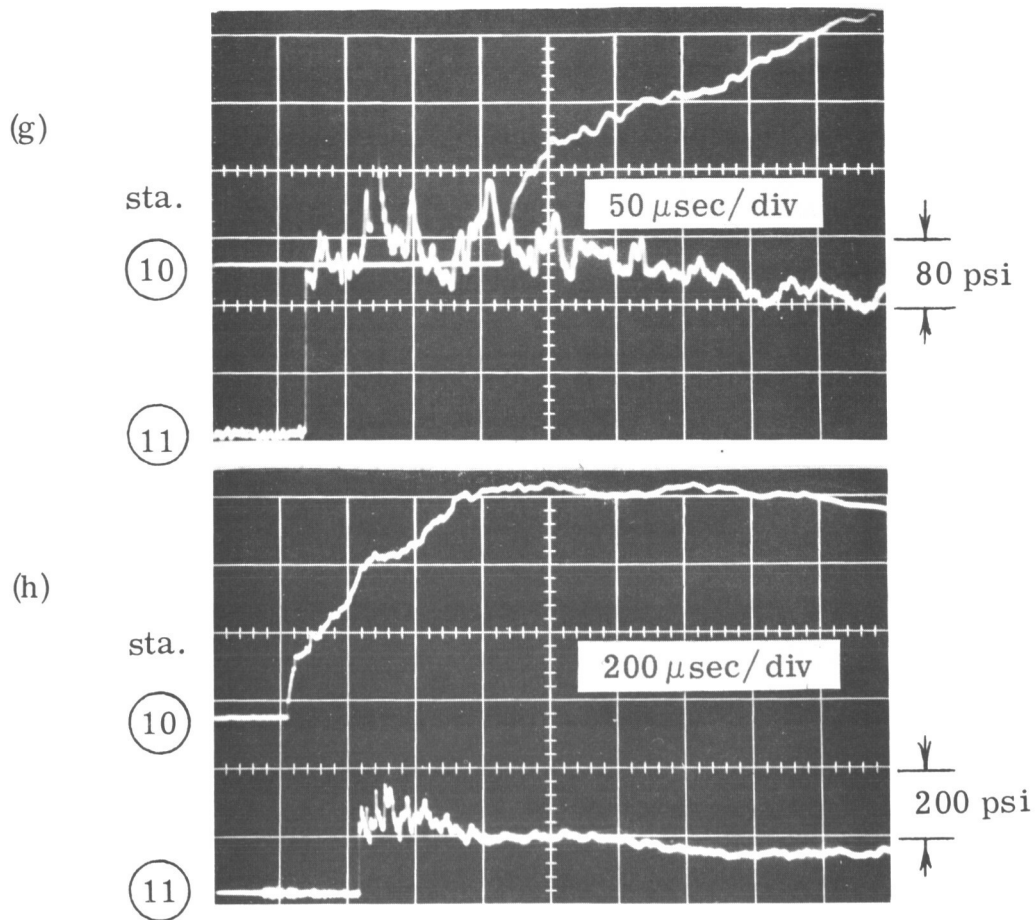


Fig. 2. 16

- (g) Run 281. Upper beam: heat transfer gauge No. 10 at station 10, 0.01 V/div and 50  $\mu\text{sec}/\text{div}$ , triggered at station 9. Lower beam: pressure transducer No. 6.5 at station 11, 80 psi/div, and 50  $\mu\text{sec}/\text{div}$  delayed 350  $\mu\text{sec}$ , triggered at station 9.
- (h) Run 282. Upper beam: heat transfer gauge No. 10 at station 10, 0.02 V/div and 200  $\mu\text{sec}/\text{div}$ , triggered at station 9. Lower beam: pressure transducer No. 6.5 at station 11, 200 psi/div and 200  $\mu\text{sec}/\text{div}$ , triggered at station 9.

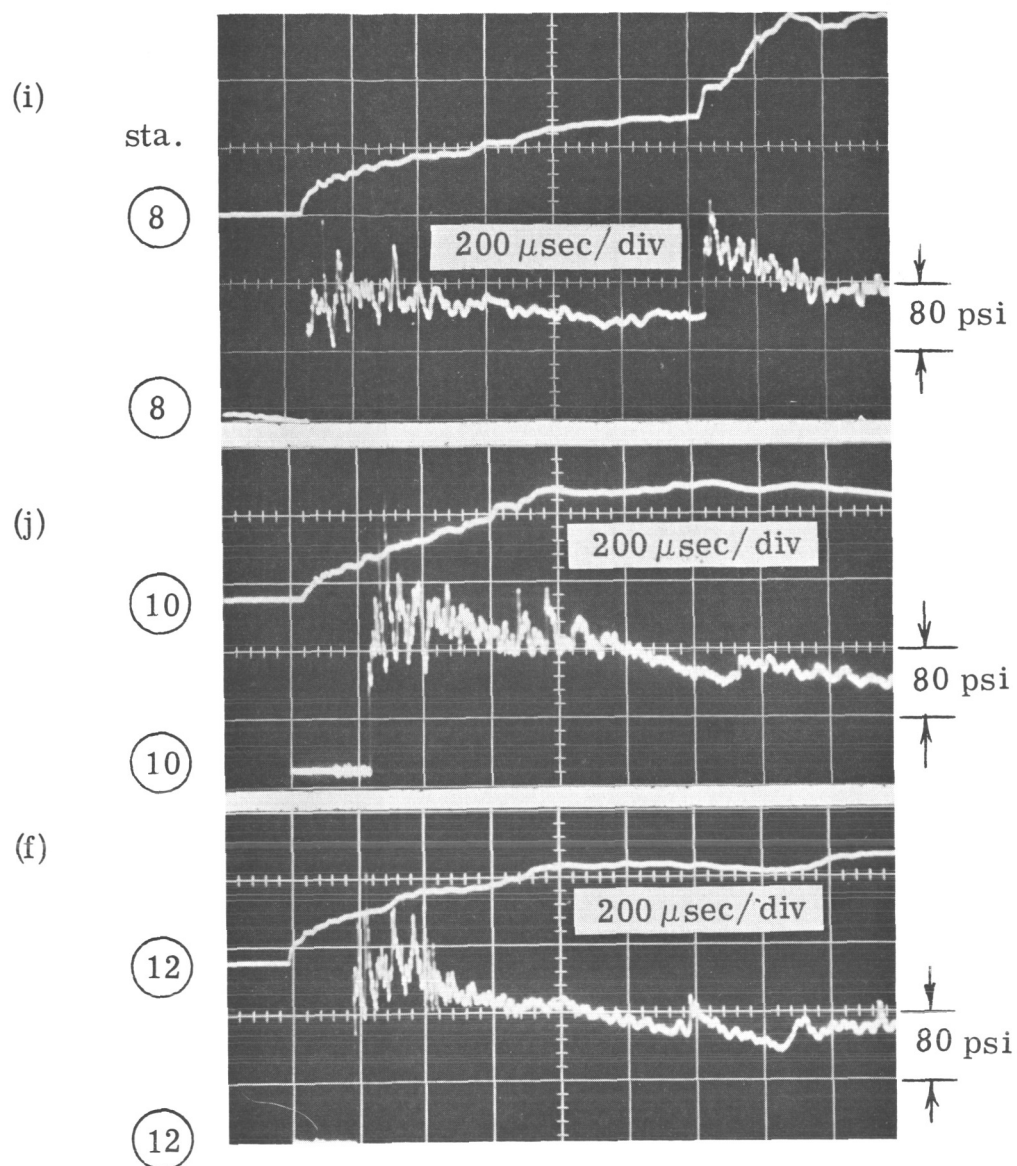


Fig. 2.16

- (i) Run 285. Station 8 triggered at station 7. Upper beam: heat transfer gauge No. 10, .02 V/div and 200  $\mu\text{sec}/\text{div}$ . Lower beam: pressure transducer No. 6.5, 80 psi/div and 200  $\mu\text{sec}/\text{div}$ .
- (j) Run 292. Station 10 triggered at station 9. Upper beam: heat transfer gauge No. 10, .05 V/cm and 200  $\mu\text{sec}/\text{div}$ . Lower beam: pressure transducer No. 6.5, 80 psi/div and 200  $\mu\text{sec}/\text{div}$ .
- (k) Run 288. Station 12 triggered at station 11. Upper beam: heat transfer gauge No. 10, .05 V/div and 200  $\mu\text{sec}/\text{div}$ . Lower beam: pressure transducer No. 6.5, 80 psi/div and 200  $\mu\text{sec}/\text{div}$ .

the trigger to the initial rise of the transducer can be used to compute the average velocity between stations. And second, the initial pressure rise at a given station can be used to obtain the velocity from the normal shock relations. The results for the records which have been presented are shown in Fig. 2.17. The values obtained by the two methods are reasonably close thus lending confidence in the calibration of the transducers. The increase in velocity at about 10 ft is due to the retonation process discussed above. The theoretical steady state detonation velocity for this mixture ratio as obtained by the computer program (Fig. 2.6) is 5624 ft/sec. The observed velocity of 3850 ft/sec is 32% below the theoretical. If this velocity is assumed to be steady then one can conclude from Fig. 2.6 that more losses are associated with the 2600  $\mu$  drops than the 940  $\mu$  drops. Accounting for heat and drag losses according to Eq. 3.19 as explained in section III-4, increases the detonation velocity to about 4800 ft/sec which is still 15% below the theoretical velocity.

Referring to Fig. 2.16 (g, h, j, and k) it is of interest to again consider the pressure behind the leading shock front. After the initial jump the pressure oscillates and increases slightly for about 200  $\mu$ sec due to the generation of secondary shocks. Then there is a gradual decrease in pressure indicating that heat is being added to the flow. The pressure appears to reach a plateau after about 600  $\mu$ sec. Then there is a further decrease in pressure but at a faster rate. It is significant that the wall temperature (from the heat transfer gauges shown just above the pressure record) also levels out at about 600-700  $\mu$ sec. On this basis it is felt that the chemical heat release is over at about 600-700  $\mu$ sec behind the initial shock and that a trailing rarefaction starts from that point. That is to say, the reaction zone thickness is about 2.25 ft.

A summary of the pressure at the initial shock front and at the estimated end of the reaction zone is given in Table II as measured at various positions

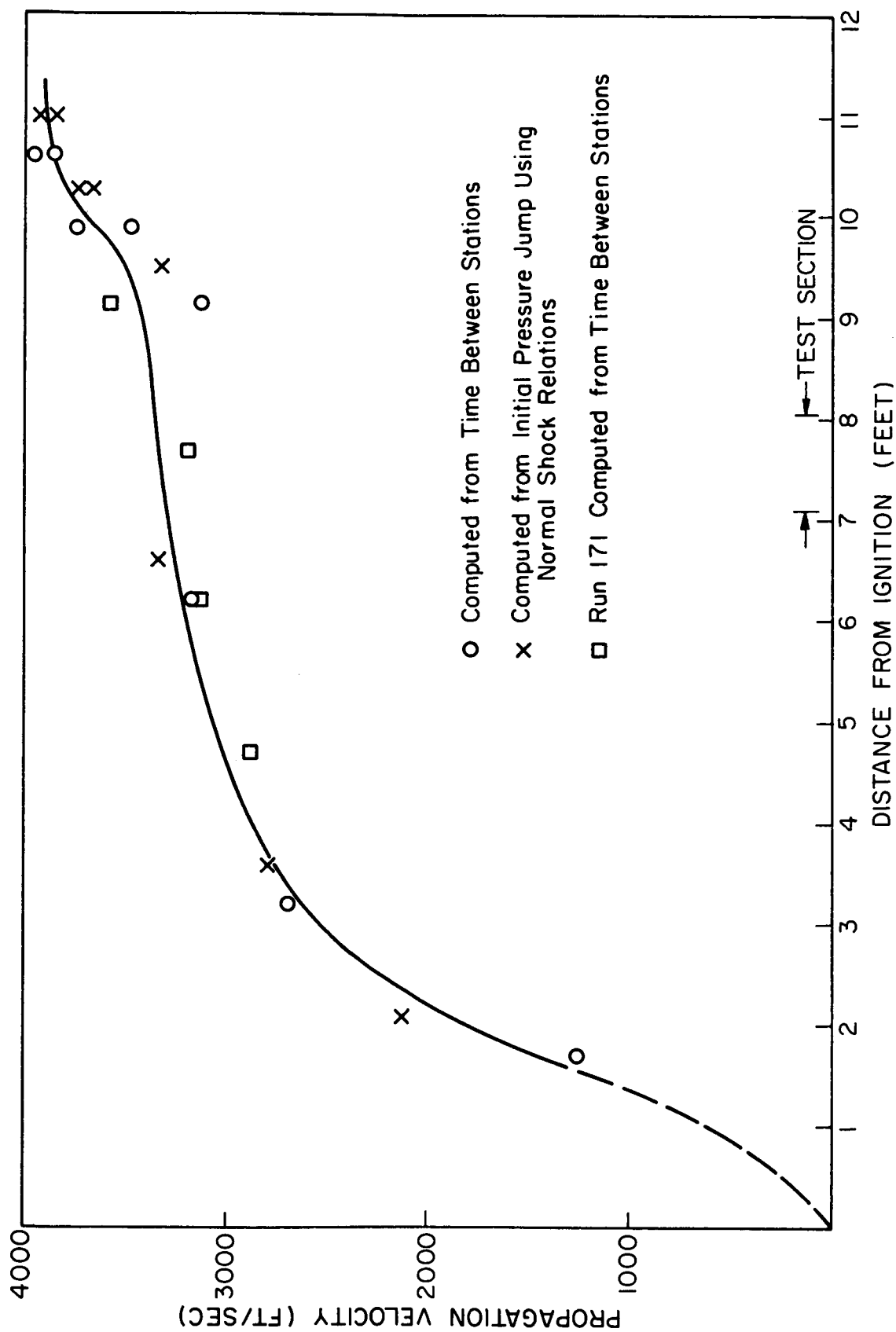


Figure 2.17 Propagation Velocity vs. Distance from Ignition Source for 2600  $\mu$  Diameter Drop Detonation.

TABLE II. ANALYSIS OF PRESSURE DATA FOR 2600  $\mu$  DIAMETER DROPLET DETONATION.

Run	Station	Measured ( $P_1 = 14.5$ psi)	Calculated using Normal Shock Relations	Measured at $t_x$	Calculated from Eq. 3.11 with $\phi = 0$ and $C_D = 0$	Calculated from Eq. 3.11 with $C_D = 0$	Calculated from Eq. 3.33	Estimated Time for Completion of Reaction Zone ( $\mu$ sec)
		$P_2/P_1$	$M_s$	$P_3/P_1$	$P_3/P_1$	$P_3/P_1$	$P_3/P_1$	$t_x$
294	2	4.5	2.00	(5.5)	3.0	3.2	4.1	> 1400
293	4	7.9	2.63	(7.9)	4.9	5.2	6.7	> 1400
285	8	11.4	3.15	(9.0)	6.8	7.3	9.4	> 1200
292	10	11.3	3.12	11.0	6.8	7.2	9.2	600
282	11	14.1	3.50	12.0	8.3	8.9	11.5	600
287	12	15.6	3.68	12.6	8.9	9.5	12.7	600
288	12	15.4	3.65	12.1	9.5	10.1	12.5	600



along the combustion tube. Also the measured results are compared with the theory of section III. At stations 2, 4, and 8 (Figs. 2.16 c,d,i) the observation time is not long enough to determine the end of the reaction zone. At station 2 the pressure is actually higher at 1400  $\mu$ sec after the passage of the initial shock, than just after the shock. At station 4 the pressure at 1400  $\mu$ sec equals the shock pressure. Stations 10 and 12 are more applicable to the theory of section III. The measured pressure at what is considered the end of the reaction zone ( $t_x = 600 \mu$ sec) is in very good agreement with the calculated Chapman-Jouguet pressure at the measured Mach number after accounting for the effect of viscous drag.

The wall temperature data was converted to heat transfer to the wall according to the procedure outlined in the Appendix. The results for runs 288, 292 and 285 (from the data of Fig. 2.16 i,j,k) is shown in Fig. 2.18. This figure was drawn by a CALCOMP 780/763 digital plotter which is linked to an IBM 7090 computer. Stations 10 and 12 show a heat transfer rate of approximately 1000 Btu/ft<sup>2</sup>-sec for a period up to 800  $\mu$ sec after passage of the initial shock front. The large fluctuations are not unreasonable in view of the discrete combustion zones, turbulence, and secondary shocks. After 800  $\mu$ sec the heat transfer rate decreases markedly and the fluctuations are considerably less. At about 1500  $\mu$ sec the reflected shock from the end of the combustion tube terminates the useful data. At station 8 the heat transfer rate is considerably lower since the detonation is less fully developed. A value of approximately 350 Btu/ft<sup>2</sup>-sec is maintained for 1200  $\mu$ sec, at which point the "retonation" appears. These results contrast significantly to the heat transfer measurements behind a one atmosphere hydrogen-oxygen gaseous detonation, which is discussed in the Appendix, due primarily to the extended reaction zone and lower propagation velocity.

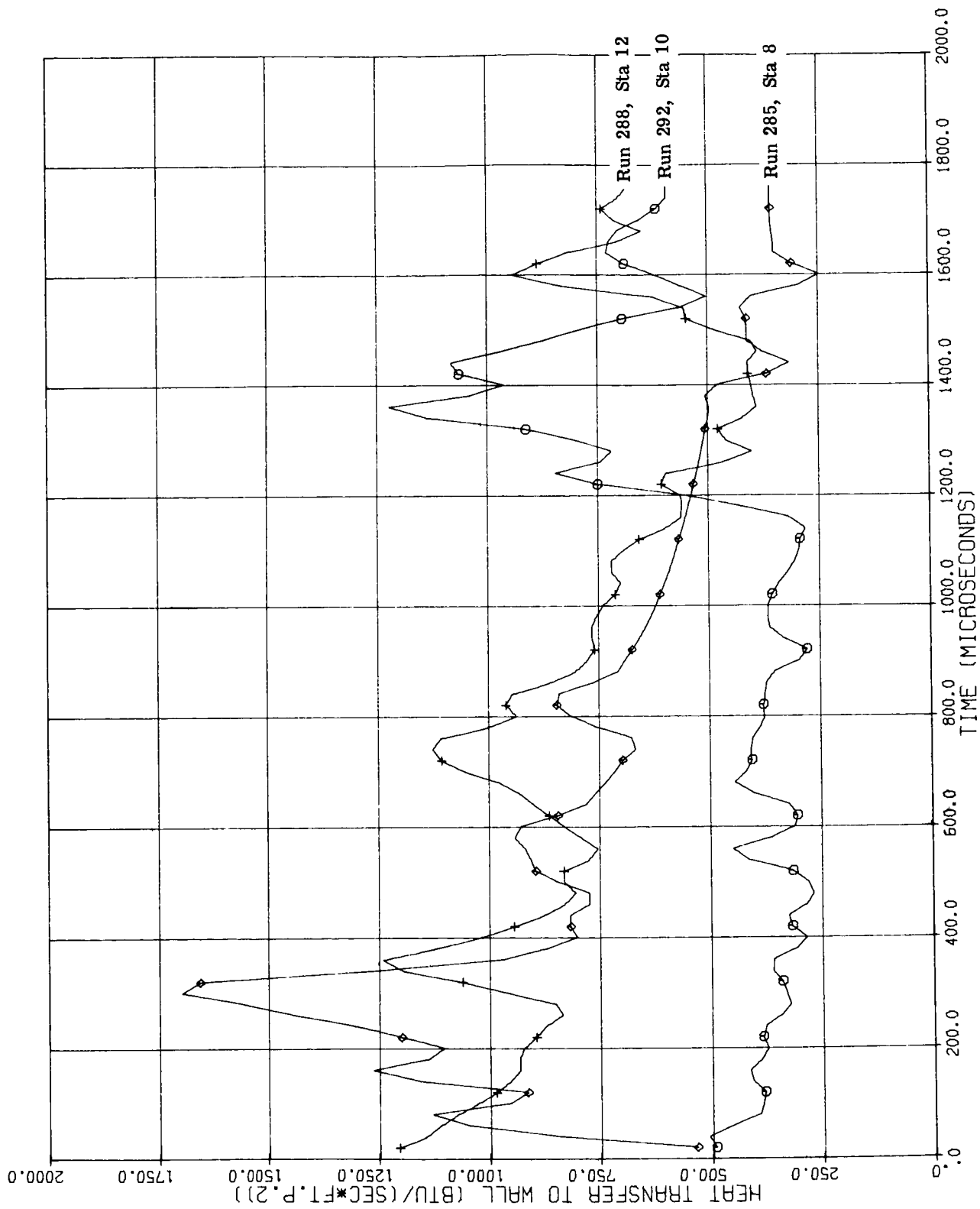


Figure 2.18 Heat Transfer to the Wall from Data Shown in Fig. 2.16(i,j,k).

### III. TWO-PHASE DETONATIONS—THEORY AND APPLICATION

In Refs. (1) and (2) experiments were reported which demonstrated that a detonation wave can propagate in a tube in which the walls are coated with a thin film of liquid fuel; the tube is filled with gaseous oxygen such that the fuel and oxidizer are completely unmixed. Results from pressure transducers, self-luminous framing camera photographs and spark schlieren photographs showed the detonation-like characteristics of this phenomena. In Ref. (3) other observations of film detonations were reviewed and additional photographs of film detonations taken with an image converter camera were presented. Also, the experimental results on the removal of an inert liquid layer on a flat plate which was swept over by a normal shock were given. It was concluded that the liquid layer is gradually stripped off but remains within the boundary layer for at least  $200\ \mu\text{sec}$ . Based on the experimental evidence, a diffusion limited boundary layer combustion model for film detonations was postulated. It is apparent that the boundary layer is highly turbulent. However, as a basis of comparison to possible semi-empirical turbulent analyses, a laminar boundary model was considered first. Equations for a laminar boundary layer with mass addition and chemical reaction behind a travelling normal shock were developed.

In this section the one-dimensional difference equations for a detonation with mass, momentum and heat transfer at the boundaries will be developed to obtain expressions for the Mach number of propagation, pressure ratio, temperature ratio, etc., across the detonation in terms of the reaction zone thickness, and drag, mass and heat transfer coefficients. These equations apply to a film detonation as well as to a spray detonation provided that the boundaries of the control volume are defined to account for the drops. These equations will be useful for correlation with the experimental results. Numerical results for the transfer coefficients for a film detonation which were

obtained from the solution of the laminar boundary layer equations will then be presented. The solutions of the boundary layer profiles which were obtained from the analysis will not be given here, but it is anticipated that a separate report on this subject will be published.

### 1. One Dimensional Difference Equations with Mass, Momentum and Heat Transfer at the Boundaries.

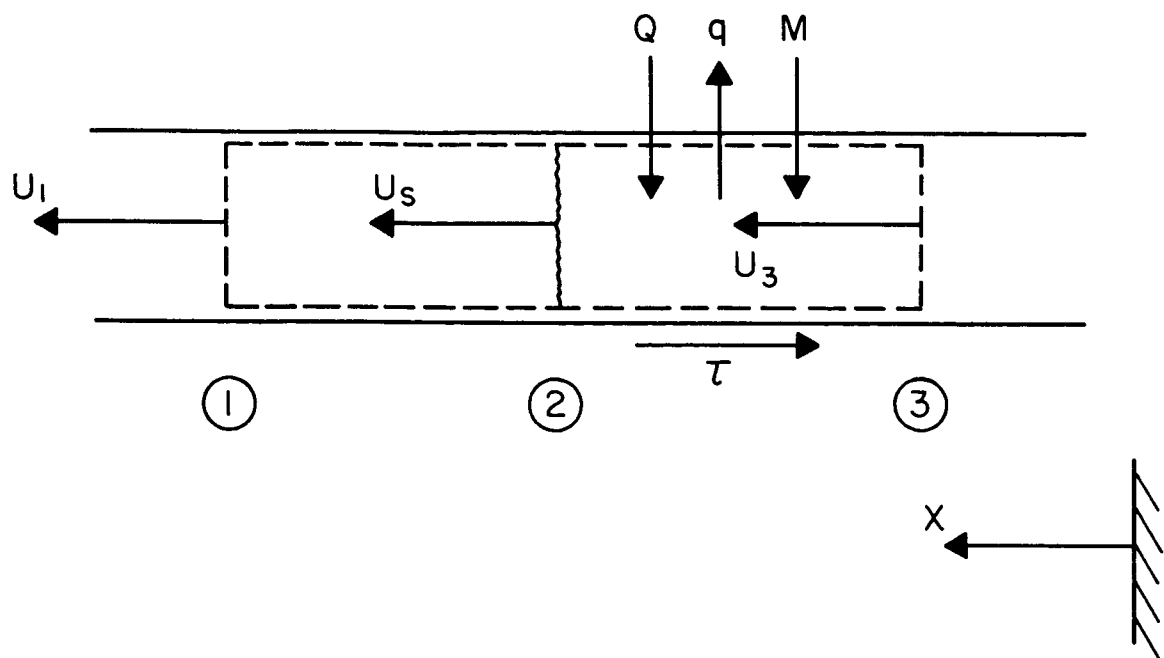
Consider a column of gas in a tube between  $x = x_1$  and  $x = x_3$  which contains a discontinuity in flow variables at  $x = x_2$ , i. e., a shock wave. Heat and mass addition, and shear stress and heat loss at the boundaries occur between  $x_2$  and  $x_3$ . For a time unsteady flow the conservation equations are best derived using a wall fixed coordinate system, however, for a time steady flow either wall fixed or shock fixed coordinates may be used. It is instructive to derive the steady flow conservation equations in wall fixed coordinates and then transform the results to shock fixed coordinates. The coordinate systems are shown in Fig. 3.1. The transformation from the laboratory coordinate  $x$  to the shock fixed coordinate  $\bar{x}$  is given by  $\bar{x} = u_s t - x$ . The velocity transformation between coordinates is  $\bar{u}_1 = u_s - u_1$ .

Let the control volume be denoted by dotted lines. In shock fixed coordinates the control volume is fixed. In wall fixed coordinates let the front and back surfaces of the control volume move with convective velocities  $u_1$  and  $u_3$  respectively.

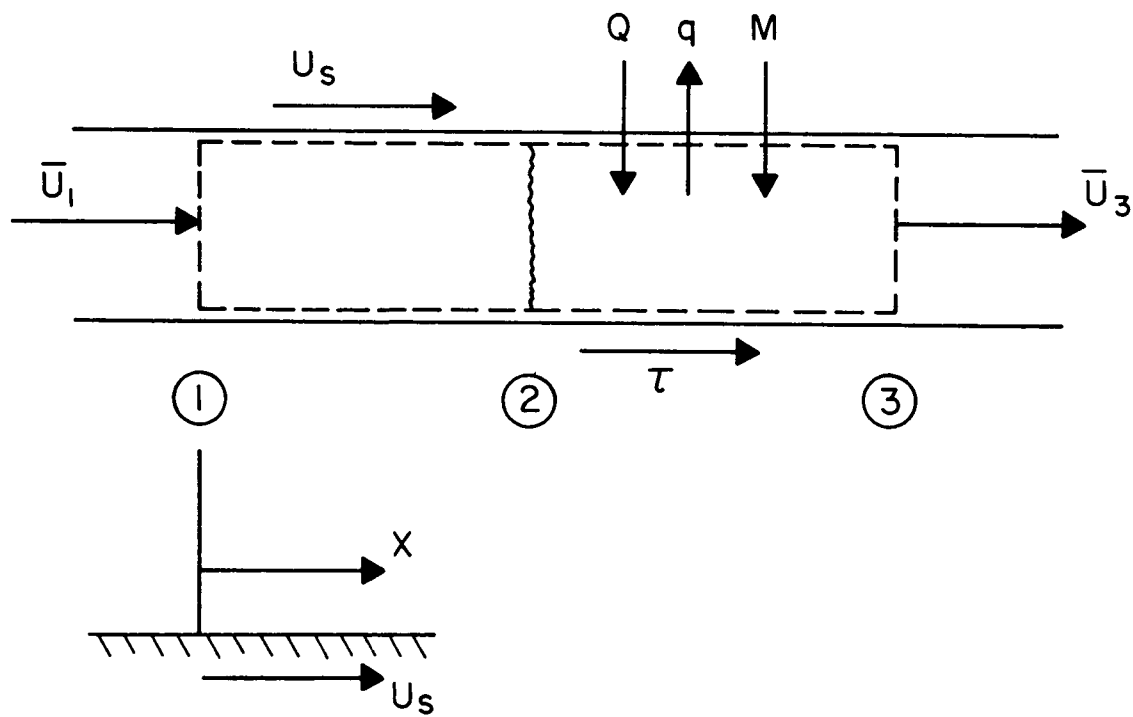
Conservation of mass for the control volume is

$$\frac{d}{dt} \int_3^1 \rho A_c dx = \int_3^2 M b dx$$

Moving the derivative inside the integral (applying the Leibnitz rule, see Courant-Friedrich's, Ref. (6)) and accounting for the discontinuity at  $x_2$ , we have in general,



(a) Wall Fixed Coordinates



(b) Shock Fixed Coordinates

Figure 3.1 Control Volume and Coordinate System for Use with One-Dimensional Conservation Equations.

$$\begin{aligned}\frac{d}{dt} \int_3^1 \psi(x, t) dx &= \frac{d}{dt} \int_3^{2+} \psi dx + \frac{d}{dt} \int_{2-}^1 \psi dx \\ &= \int_3^2 \frac{\partial \psi}{\partial t} dx + \psi_{2+} \frac{dx_2}{dt} - \psi_3 \frac{dx_3}{dt} + \psi_1 \frac{dx_1}{dt} - \psi_{2-} \frac{dx_2}{dt}\end{aligned}$$

Let the limits become:

$$2+ = 2, \quad 2- = 1, \text{ and } \frac{dx_1}{dt} = u_1, \quad \frac{dx_2}{dt} = u_s, \quad \frac{dx_3}{dt} = u_3$$

Then

$$\frac{d}{dt} \int_3^1 \psi(x, t) dx = \int_3^2 \frac{\partial \psi}{\partial t} dx + \psi_2 u_s - \psi_3 u_3 - \psi_1 (u_s - u_1) \quad (3.1)$$

Conservation of mass for a constant area duct becomes,

$$\int_3^2 \frac{\partial \rho}{\partial t} dx + \rho_2 u_s - \rho_3 u_3 - \rho_1 (u_s - u_1) = - \frac{b}{A_c} \int_3^2 M dx$$

For a constant velocity of propagation  $x$  and  $t$  are related by  $x = -u_s t$ , i.e., moving forward in time is equivalent to moving back in distance in the laboratory fixed coordinate system, and thus we can write,

$$\int_3^2 \frac{\partial \rho}{\partial t} dx = -u_s \int_3^2 \frac{\partial \rho}{\partial x} dx = -\rho_2 u_s + \rho_3 u_s$$

And the continuity equation becomes,

$$\rho_3 (u_s - u_3) - \rho_1 (u_s - u_1) = \frac{b}{A_c} \int_3^2 M dx$$

Since

$$\int_3^2 M dx = \int_2^3 M d\bar{x} \quad ,$$

the continuity equation in shock fixed coordinates is,

$$\rho_3 \bar{u}_3 - \rho_1 \bar{u}_1 = \frac{b}{A_c} \int_2^3 M d\bar{x} \quad (3.2)$$

Conservation of momentum for constant area duct is given by,

$$A_c \frac{d}{dt} \int_3^1 \rho u dx = (p_3 - p_1) A_c - \int_3^2 \tau b dx$$

Moving the derivative inside, we obtain:

$$\int_3^2 \frac{\partial \rho u}{\partial t} dx + \rho_2 u_2 u_s - \rho_3 u_3^2 - \rho_1 u_1 (u_s - u_1) = p_3 - p_1 - \frac{b}{A_c} \int_3^2 \tau dx \quad .$$

Thus,

$$\rho_3 u_3 (u_s - u_3) - \rho_1 u_1 (u_s - u_1) = p_3 - p_1 - \frac{b}{A_c} \int_2^3 \tau d\bar{x} \quad .$$

Substituting  $\bar{u}_i = u_s - u_i$  and using conservation of mass equation, we obtain:

$$\rho_3 \bar{u}_3^2 - \rho_1 \bar{u}_1^2 - \frac{u_s b}{A_c} \int_2^3 M d\bar{x} = p_1 - p_3 + \frac{b}{A_c} \int_2^3 \tau d\bar{x} \quad (3.3)$$

Conservation of energy for a constant area duct is given by,

$$\frac{d}{dt} \int_3^2 \rho \left( e + \frac{u^2}{2} \right) dx = (p_3 u_3 - p_1 u_1) - \frac{b}{A_c} \int_3^2 (Q - q + M e_M) dx$$

where the first term on the right hand side is the power supplied by outside forces and the second term is the rate at which energy is transferred into the control volume. Moving the derivative inside, the energy equation becomes,

$$\begin{aligned} \int_3^2 \frac{\partial}{\partial t} \left[ \rho \left( e + \frac{u^2}{2} \right) \right] dx - \rho_3 \left( e_3 + \frac{u_s^2}{2} \right) u_3 + \rho_2 \left( e_2 + \frac{u_2^2}{2} \right) u_s - \rho_1 \left( e_1 + \frac{u_1^2}{2} \right) (u_s - u_1) \\ = p_3 u_3 - p_1 u_1 - \frac{b}{A_c} \int_3^2 (Q - q + M e_M) dx \end{aligned}$$

For constant velocity of propagation  $dx = -u_s dt$  and,

$$\begin{aligned} \rho_3 \left( e_3 + \frac{u_3^2}{2} \right) (u_s - u_3) - \rho_1 \left( e_1 + \frac{u_1^2}{2} \right) (u_s - u_1) = p_3 u_3 - p_1 u_1 \\ - \frac{b}{A_c} \int_3^2 (Q - q + M e_M) dx \end{aligned}$$

Substituting  $u_i = u_s - \bar{u}_i$  and using conservation of mass and momentum equations, the energy equation becomes,

$$\begin{aligned} \rho_3 \bar{u}_3 \left( e_3 + \frac{\bar{u}_3^2}{2} \right) - \rho_1 \bar{u}_1 \left( e_1 + \frac{\bar{u}_1^2}{2} \right) - \left( e_m + \frac{u_s^2}{2} \right) \frac{b}{A_c} \int_2^3 M d\bar{x} = p_1 \bar{u}_1 - p_3 \bar{u}_3 \\ + \frac{b}{A_c} \int_2^3 (Q - q + \tau u_s) d\bar{x} \quad . \end{aligned} \quad (3.4)$$



Equations (3.2), (3.3), and (3.4) are the general conservation equations in integral form for one-dimensional flow in shock fixed coordinates. Let us now assume that:

- a) The fluid is initially at rest, i.e.,  $u_1 = 0$ .
- b) The Chapman-Jouguet condition holds at position  $x_3$ , i.e.,  $\bar{u}_3 = a_3$
- c) The gases are both thermally and calorically perfect so that,

$$h = C_p T = \frac{a^2}{\gamma - 1}$$

$$a^2 = \frac{\gamma p}{\rho} = \gamma RT$$

In terms of  $\rho$ ,  $a$  and  $u_s$  the conservation equations become,

$$\rho_3 a_3 - \rho_1 u_s = C \quad (3.5)$$

$$\rho_3 a_3^2 \left( \frac{\gamma_3 + 1}{\gamma_3} \right) - \rho_1 \left( u_s^2 + \frac{a_1^2}{\gamma_1} \right) = u_s C + D \quad (3.6)$$

$$\rho_3 a_3^3 \left( \frac{\gamma_3 + 1}{\gamma_3 - 1} \right) - \rho_1 u_s \left( \frac{2a_1^2}{\gamma_1 - 1} + u_s^2 \right) = (u_s^2 + 2e_m) C + 2u_s D + 2E \quad (3.7)$$

where

$$C \equiv \frac{b}{A_c} \int_2^3 M d\bar{x} = C_M \left( \frac{A_s}{A_c} \right) \left( \frac{u_2}{\bar{u}_2} \right) \rho_1 u_s = \phi \rho_1 u_s \quad (3.8)$$

$$D \equiv \frac{b}{A_c} \int_2^3 \tau d\bar{x} = C_D \left( \frac{A_s}{A_c} \right) \left( \frac{u_2^2}{u_s \bar{u}_2} \right) \frac{\rho_1 u_s^2}{2} \quad (3.9)$$

$$\begin{aligned}
E &= \frac{b}{A_c} \int_2^3 (Q - q) dx = \Delta H C_M \left( \frac{A_s}{A_c} \right) \left( \frac{u_2}{\bar{u}_2} \right) \rho_1 u_s - C_H \left( h_1 + \frac{u_s^2}{2} - h_w \right) \left( \frac{A_s}{A_c} \right) \left( \frac{u_2}{\bar{u}_2} \right) \rho_1 u_s \\
&= \left[ \phi \Delta H - C_H \left( h_1 + \frac{u_s^2}{2} - h_w \right) \left( \frac{A_s}{A_c} \right) \left( \frac{u_2}{\bar{u}_2} \right) \right] \rho_1 u_s \quad (3.10)
\end{aligned}$$

Here we have replaced the integrals by appropriate transfer coefficients based on the initial gas conditions, and also have introduced an overall mixture ratio and the heat of combustion per unit mass of fuel. Also the shock relation  $\rho_1 u_s = \rho_2 \bar{u}_2$  has been used.

From Eqs. (3.5, 3.6, 3.8, 3.9) expressions for the pressure, speed of sound, density and temperature ratios across the detonation can be written in terms of the Mach number of propagation as follows:

$$\frac{p_3}{p_1} = \frac{1}{1 + \gamma_3} \left[ 1 + \gamma_1 M_s^2 \left( 1 + \phi + \frac{C_D A_s u_2^2}{2 A_c u_s \bar{u}_2} \right) \right] \quad (3.11)$$

$$\frac{a_3}{a_1} = \frac{\gamma_3}{1 + \gamma_3} \left[ M_s + \frac{1}{\gamma_1 M_s (1 + \phi)} + \frac{M_s C_D A_s u_2^2}{2 A_c u_s \bar{u}_2 (1 + \phi)} \right] \quad (3.12)$$

$$\frac{\rho_3}{\rho_1} = \frac{(1 + \gamma_3)(1 + \phi)}{\gamma_3} \left[ 1 + \frac{1}{\gamma_1 M_s^2 (1 + \phi)} + \frac{C_D A_s u_2^2}{2(1 + \phi) A_c u_s \bar{u}_2} \right]^{-1} \quad (3.13)$$

$$\frac{T_3}{T_1} = \frac{\gamma_3 m_3}{\gamma_1 m_1} \left[ \frac{1 + \gamma_1 (1 + \phi) M_s^2 + \frac{\gamma_1 C_D A_s u_2^2 M_s^2}{2 A_c u_s \bar{u}_2}}{M_s (1 + \phi)(1 + \gamma_3)} \right]^2 \quad (3.14)$$

In order to obtain an expression for the Mach number of propagation in terms of the transfer coefficients, heat release, etc., one must also include the energy equation which after considerable manipulation yields a fourth order algebraic equation,

$$\begin{aligned}
M_s^4 & \left[ (1 + \phi)^2 + \frac{C_D A_s u_2^2 (1 + \phi)}{A_c u_s \bar{u}_2} + \left( \frac{\gamma_3 C_D A_s u_2^2}{2 A_c u_s \bar{u}_2} \right)^2 \right] \\
& + 2M_s^2 \left[ \left( \frac{\gamma_3^2}{\gamma_1} - \frac{\gamma_3^2 - 1}{\gamma_1 - 1} \right) (1 + \phi) - \frac{(\gamma_3^2 - 1)(\phi + \phi^2)(\Delta H + e_m)}{a_1^2} \right. \\
& \left. + \frac{(\gamma_3^2 - 1)(1 + \phi) C_H \left( h_1 + \frac{u_s^2}{2} - h_w \right) A_s u_2}{a_1^2 A_c \bar{u}_2} + \frac{\gamma_3^2 C_D A_s u_2^2}{2 \gamma_1 A_c u_s \bar{u}_2} \right] \\
& + \frac{\gamma_3^2}{\gamma_1} = 0
\end{aligned} \tag{3.15}$$

When  $C_D = C_H = 0$  in Eqs. (3.11)-(3.15) the jump relations for heterogeneous detonations without dissipative losses are obtained (see, for example, Eqs. (7-10) in Ref. 1). By considering the order of magnitude of the terms in Eq. (3.15) on the basis of the next two subsections and by letting

$$h_1 + \frac{u_s^2}{2} - h_w \approx \frac{u_s^2}{2}$$

Eq. (3.15) reduces to

$$M_s^2 = \frac{2(\gamma_3^2 - 1) \phi \Delta H / a_1^2}{1 + \phi + \frac{C_D A_s u_2^2}{A_c u_s \bar{u}_2} + \frac{(\gamma_3^2 - 1) C_H A_s u_2}{A_c \bar{u}_2}} \tag{3.16}$$

or in terms of the velocity of propagation,

$$u_s^2 = \frac{2(\gamma_3^2 - 1) \phi \Delta H}{1 + \phi + \frac{C_D A_s u_2^2}{A_c u_s \bar{u}_2} + \frac{2(\gamma_3^2 - 1) C_H A_s u_2}{A_c \bar{u}_2}} \quad (3.17)$$

Denoting  $(u_s)_0$  as the approximate detonation velocity without losses in the reaction zone, where

$$(u_s)_0^2 = 2(\gamma_3^2 - 1) \phi \Delta H / (1 + \phi) \quad (3.18)$$

we have,

$$\frac{u_s^2}{(u_s)_0^2} = \frac{1}{1 + \frac{A_s C_D}{A_c (1 + \phi)} \frac{u_2^2}{u_s \bar{u}_2} + \frac{2(\gamma_3^2 - 1) A_s C_H u_2}{A_c (1 + \phi) \bar{u}_2}} \quad (3.19)$$

In order to evaluate Eqs. (3.11-3.19),  $C_D$ ,  $C_H$ , and  $A_s/A_c$  must be considered separately for the walls, both with film combustion and without, and for the drops. First, however, the transfer coefficients for a laminar boundary layer behind a detonation will be developed and then numerical evaluation will be made.

## 2. Mass, Momentum, and Heat Transfer Coefficients for a Film Detonation.

In order to evaluate the order of magnitude of the terms in Eqs. (3.11-3.19), it is necessary to determine values for the transfer coefficients. The equations for a compressible reacting laminar boundary layer behind a normal shock wave were developed in Ref. (3). The coordinate system used is shown in Fig. 3.2. In deriving these equations, the following assumptions were made:

1. The flow is laminar, steady, at constant pressure and the usual boundary layer approximations hold.

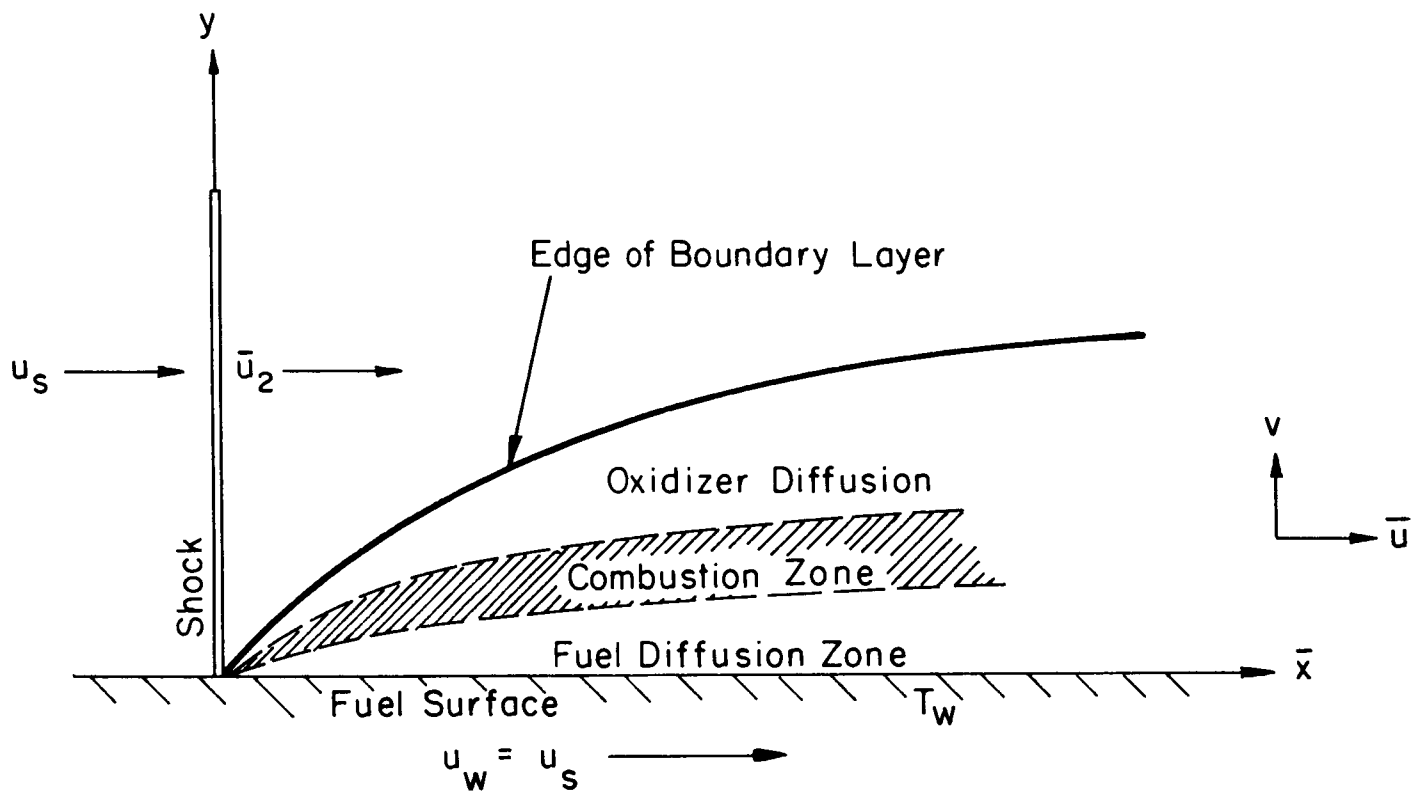
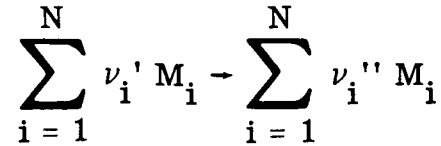


Figure 3.2 Model for Film Detonation: Normal Shock Moving Across a Flat Plate with Boundary Layer Combustion.

2. The Prandtl number is unity, the Schmidt number based on binary diffusion coefficients for each pair of species is unity; body forces, radiative energy transport, and thermal diffusion are neglected.
3.  $\rho\mu/\rho_2\mu_2 = 1$
4. There is a one step chemical reaction of the form



5. The temperature of the vaporizing fuel is constant and equal to the equilibrium boiling point temperature.
6. The properties of the external stream are constant.

The analysis was reduced to solving the Blasius equation,

$$\frac{d^3 f}{d\eta^3} + f \frac{d^2 f}{d\eta^2} = 0 \quad (3.20)$$

with the boundary conditions,

$$df(0)/d\eta = 2u_s/\bar{u}_2 \quad (3.21)$$

$$df(\infty)/d\eta = 2 \quad (3.22)$$

$$\frac{f(0)}{d^2 f(0)/d\eta^2} = - \frac{B}{2(1 - u_s/\bar{u}_2)} \quad (3.23)$$

Here  $f(\eta)\sqrt{\bar{u}_2 \rho_2 \mu_2 \bar{x}}$  has the properties of a stream function and the similarity parameter  $\eta$  is defined by

$$\eta = \sqrt{\frac{\bar{u}_2}{4\rho_2 \mu_2 \bar{x}}} \int_0^y \rho dy \quad (3.24)$$

and B is a thermodynamic parameter which is defined by

$$h_L B = h_2 - h_w + \phi \Delta H \quad (3.25)$$

The solution of Eqs. (3.20-3.23) for the parameter ranges of interest was done on an analog computer and the initial conditions for  $f$  which were obtained are shown in Table III. This table supercedes Table VI of Ref. (3).

In defining mass addition, drag and heat transfer coefficients the convective velocity behind the shock in laboratory coordinates is used as follows:

$$C_M \equiv \frac{b \int_2^3 \rho_w V_w d\bar{x}}{A_s \rho_2 u_2} \quad (3.26)$$

$$C_D \equiv \frac{b \int_2^3 \tau_w d\bar{x}}{\frac{1}{2} A_s \rho_2 u_2^2} \quad (3.27)$$

$$C_H \equiv \frac{b \int_2^3 q_w d\bar{x}}{A_s \rho_2 u_2 \left( h_2 + \frac{\bar{u}_2^2}{2} - h_w \right)} \quad (3.28)$$

Since it can be shown that under the assumptions of this section,

$$q_w = - \tau_w \left( h_2 + \frac{\bar{u}_2^2}{2} - h_w \right) / u_2$$

it follows that

$$C_H = - \frac{C_D}{2} \quad (3.29)$$

In terms of  $f$  and a Reynolds number based on the laboratory velocity Eqs. (3.26-3.28) become,

TABLE III. SUMMARY OF INITIAL CONDITIONS SATISFYING  
THE BLASIUS EQUATION FOR VARIOUS VALUES  
OF  $M_s$  AND B.

Case	$-f(0)$	$f'(0)$	$-f''(0)$	B	$M_s$	$C_M \sqrt{Re_2}$	$C_D \sqrt{Re_2}$	$C_H \sqrt{Re_2}$
1	0	0	-1.33	0	-	0	-1.33	0.67
2	1.00	0	-0.14	14.2	-	-1.00	-0.14	0.07
3	0	4	2.88	0	1.58	0	2.88	1.44
4	1.00	4	1.77	1.1	1.58	1.00	1.77	0.885
5	2.00	4	0.96	4.1	1.58	2.00	0.96	0.48
6	3.00	4	0.45	13.3	1.58	3.00	0.45	0.225
7	3.50	4	0.29	24.2	1.58	3.50	0.29	0.145
8	4.00	4	0.17	47.1	1.58	4.00	0.17	0.085
9	4.73	4	0.073	130	1.58	4.73	0.073	0.037
10	0	6	6.79	0	2.24	0	2.40	1.20
11	3.00	6	1.67	7.2	2.24	2.12	0.591	0.296
12	3.60	6	1.16	12.4	2.24	2.55	0.410	0.205
13	4.20	6	0.78	21.5	2.24	2.97	0.276	0.138
14	4.80	6	0.49	39.2	2.24	3.39	0.173	0.087
15	5.40	6	0.30	72.0	2.24	3.82	0.106	0.053
16	0	8	11.49	0	3.16	0	2.21	1.105
17	4.00	8	2.08	11.5	3.16	2.31	0.400	0.20
18	4.80	8	1.29	22.3	3.16	2.77	0.248	0.124
19	5.20	8	1.00	31.2	3.16	3.0	0.192	0.096
20	5.60	8	0.76	44.2	3.16	3.23	0.146	0.073
21	6.40	8	0.42	91.4	3.16	3.70	0.081	0.041
22	0	10	16.89	0	5.00	0	2.11	1.06
23	4.00	10	3.63	8.8	5.00	2.0	0.454	0.227
24	5.00	10	2.12	18.9	5.00	2.5	0.265	0.133
25	6.00	10	1.15	41.7	5.00	3.0	0.144	0.072
26	7.00	10	0.58	96.6	5.00	3.5	0.073	0.037
27	7.50	10	0.40	150	5.00	3.76	0.050	0.025



$$C_M \sqrt{Re_2} = - \frac{f(0)}{[(u_s/\bar{u}_2) - 1]^{1/2}} \quad (3.30)$$

$$C_D \sqrt{Re_2} = \frac{f''(0)}{[(u_s/\bar{u}_2) - 1]^{3/2}} \quad (3.31)$$

$$C_H \sqrt{Re_2} = - \frac{f''(0)}{2[(u_s/\bar{u}_2) - 1]^{3/2}} \quad (3.32)$$

### 3. Application—Estimate of the Effect of Drag and Heat Loss on the Detonation Parameters.

The influence of drag and heat loss within the reaction zone on the detonation properties described by Eqs. (3.11-3.14) and (3.19), will be briefly examined. First the proper drag coefficients must be determined. As a basis of comparison, drag coefficients for various cases of interest are summarized in Table IV. All of these coefficients are for constant free stream properties, which of course is not the case in a two-phase detonation, but will nevertheless be used as a first approximation to our problem. The analysis for burning walls in turbulent flow is not yet completed. It is interesting to note, however, that the skin friction of a burning wall is much lower than that of an inert wall.

The numerical evaluation will be made for a droplet detonation only. For this purpose we will use  $C_D = 1.5$  for drops within the reaction zone (based on the initial projected frontal area) and  $C_D = 2.5 \times 10^{-3}$  for the wall drag coefficient. This latter drag coefficient which, as indicated in Table IV, is for turbulent boundary layer over non-burning plate, is chosen because of photographic evidence of turbulence within the reaction zone.

In order to evaluate  $A_s/A_c$  for the drops let  $N$  = number of drops per unit volume,  $X$  = distance between the shock and the end of the reaction zone and  $R$  = radius of the drop. Then,

$$A_s = N \pi R^2 A_c X$$

But by definition,

TABLE IV. SUMMARY OF ESTIMATED DRAG COEFFICIENTS

Case	General Form	For $Re_2 \approx 3.0 \times 10^7$
Inert flat plate:		
A. Wind tunnel		
1. Laminar boundary layer (Ref. 7)	$1.33/\sqrt{Re_2}$	$0.244 \times 10^{-3}$
2. Turbulent boundary layer (Ref. 8)	$0.074/(Re_2)^{1/5}$	$3.76 \times 10^{-3}$
B. Shock Tube		
1. Laminar boundary layer for $M_s = 3.16$ (Ref. 9)	$2.22/\sqrt{Re_2}$	$0.406 \times 10^{-3}$
2. Turbulent boundary layer for $M_s = 3.16$ (Ref. 10)		$2.5 \times 10^{-3}$
Burning flat plate:		
A. Wind tunnel		
1. Laminar boundary layer for $B = 31$ (Ref. 11)	$0.069/\sqrt{Re_2}$	$0.0126 \times 10^{-3}$
2. Turbulent boundary layer for $B = 31$ (Ref. 12)	$\frac{0.074 \ln(1+B)}{(Re_2)^{1/5} B}$	$0.420 \times 10^{-3}$
B. Shock Tube		
1. Laminar boundary layer for $M_s = 3.16$ , $B = 31$ (this report)	$0.192/\sqrt{Re_2}$	$0.0352 \times 10^{-3}$
2. Turbulent boundary layer		

Liquid drop in conventional shock tube:

- A. Inert drop for  $10^2 < Re < 10^4$  (Ref. 13)  $\sim 2$
- B. Burning drop for  $10^2 < Re < 10^4$  (Ref. 13)  $\sim 1.5$

$$N = 3 \phi \rho_1 / 4 \pi R^3 \rho_\ell$$

therefore,

$$A_s / A_c = 3 \phi \rho_1 X / 4 \rho_\ell R$$

or for our experiments with oxygen and DECH,

$$(A_s / A_c)_{\text{drops}} = 1.27 \cdot 10^{-3} \phi X / R$$

For the walls  $A_s / A_c$  is simply  $16X/b$  for a square tube.

The term  $u_2^2 / u_s \bar{u}_2$  is of course a function of  $M_s$ ; its value changes from 2.11 at  $M_s = 3$  to 3.64 at  $M_s = 7$  for a perfect gas with  $\gamma = 1.4$ . For our purposes here we will take  $u_2^2 / u_s \bar{u}_2 = 3$ .

The terms  $X/R$  and  $X/b$  must be evaluated from experiments. From our experiments with the  $2600 \mu$  diameter drops it appears that  $X/R \approx 500$ . A possible assumption, which must be checked by experiments, is that  $X/R$  remains constant for different drop sizes. If the reaction length  $X$  is considered controlled by the breakup time of the drops, such an assumption would be consistent with our results on the breakup of inert drops in Fig. 4.12 from which one can infer a constant ratio between drop diameter and breakup distance.

With the above assumptions, Eqs. (3.11-3.14) for a spray detonation with dry walls become,

$$\frac{p_3}{p_1} = \frac{1 + \gamma_1 M_s^2 [(1 + \phi) + 1.4 \phi + .06 X/b]}{1 + \gamma_3} \quad (3.33)$$

$$\frac{a_3}{a_1} = \frac{\gamma_3 M_s}{1 + \gamma_3} \left[ \left( 1 + \frac{1}{\gamma_1 M_s^2 (1 + \phi)} \right) + \frac{1.4 \phi}{1 + \phi} + \frac{.06 X/b}{1 + \phi} \right] \quad (3.34)$$

$$\frac{\rho_3}{\rho_1} = \frac{(1 + \gamma_3)(1 + \phi)}{\gamma_3} \left[ \left( 1 + \frac{1}{\gamma_1 M_s^2 (1 + \phi)} \right) + \frac{1.4 \phi}{1 + \phi} + \frac{.06 X/b}{1 + \phi} \right]^{-1} \quad (3.35)$$

$$\frac{T_3}{T_1} = \frac{\gamma_3 m_3}{\gamma_1 m_1 M_s^2 (1 + \phi)^2 (\gamma_3 + 1)^2} \left[ \left( 1 + \gamma_1 (1 + \phi) M_s^2 \right) + 1.4 \gamma_1 M_s^2 \phi + .06 \gamma_1 M_s^2 X/b \right]^2 \quad (3.36)$$

In Eqs. (3.33-3.36), the first term in the brackets represents the effect of mass addition through the surfaces of the control volume, the second term is due to the viscous shear stress produced by the drops, and the third term is the viscous shear of the walls on the fluid. As shown by these equations for a given  $M_s$  the effect of viscous drag is to increase the Chapman-Jouguet pressure, speed of sound and temperature and to reduce the density. The effect increases as the reaction zone becomes more extended. For our experiments with the 2600  $\mu$  diameter drops,  $X \approx 2.25$  ft and  $X/b \approx 4.1$ .

The more interesting effect of losses within the reaction zone is on the velocity of propagation for which the heat transfer coefficient must also be known. If we use the same assumptions as above and also take the heat transfer coefficient,  $C_H$ , for the inert walls as  $2.5 \times 10^{-3}$  based on preliminary experimental results, then Eq. (3.19) for the velocity becomes,

$$\frac{u_s^2}{(u_s^2)_0} = \frac{1 + \phi}{1 + 3.8 \phi + X/b \left[ .12 + .14(\gamma_3^2 - 1) \right]} \quad (3.37)$$

For our experiments with the 2600  $\mu$  diameter drops, this results in a 25% reduction in velocity due to drag and heat loss, when  $\gamma_3 = 1.18$  is assumed. Mass addition alone does not change the velocity of propagation.

More analysis needs to be done to explore the limits of propagation for a two-phase detonation, but in general the limits appear wider than our experiments have covered to date.

#### IV. DROP SHATTERING

It is apparent from the experiments described earlier that drop shattering plays a prominent supporting role in the development and propagation of detonation waves in two phase mixtures. In view of this, an understanding of the dependence of the rate of disintegration and the breakup time with the physical characteristics of the drop and the flow field conditions surrounding it, is in order.

The breakup of a liquid drop by a detonation front is accomplished through an interaction between the flow field produced by the wave and the drop. A schematic diagram of a shock-drop interaction is shown in Fig. 4.1. The specific type of deformation and disintegration resulting from the interaction is determined by the magnitude of the Weber number as shown in Fig. 4.2. For  $We > 10$ , a condition applying to all the experiments described here, the drop is deformed into a lenticular shape and layers of the liquid at its surface are rapidly stripped off by the shearing action of the convective flow.

The important variables in the drop breakup phenomenon are shown in Table V where the results of a dimensional analysis<sup>(3)</sup> are also presented. The non-dimensional breakup time  $\tau$  is an unknown function  $\phi$  of the other non-dimensional variables:

$$\tau = \phi(We, Re, Re_g, M, \beta) \quad (4.1)$$

The shattering problem has been previously studied by a number of investigators<sup>(13-21)</sup>, and a comprehensive review of the most significant experimental and analytical studies is contained in Ref. (3). Although the scope of the earlier studies did not cover the range of conditions characteristic of two phase detonations, it appears that the two most important variables are  $\tau$  and  $\beta$  when a high dynamic pressure environment, as might be created by a detonation wave, prevails. However, this remains to be more firmly established.

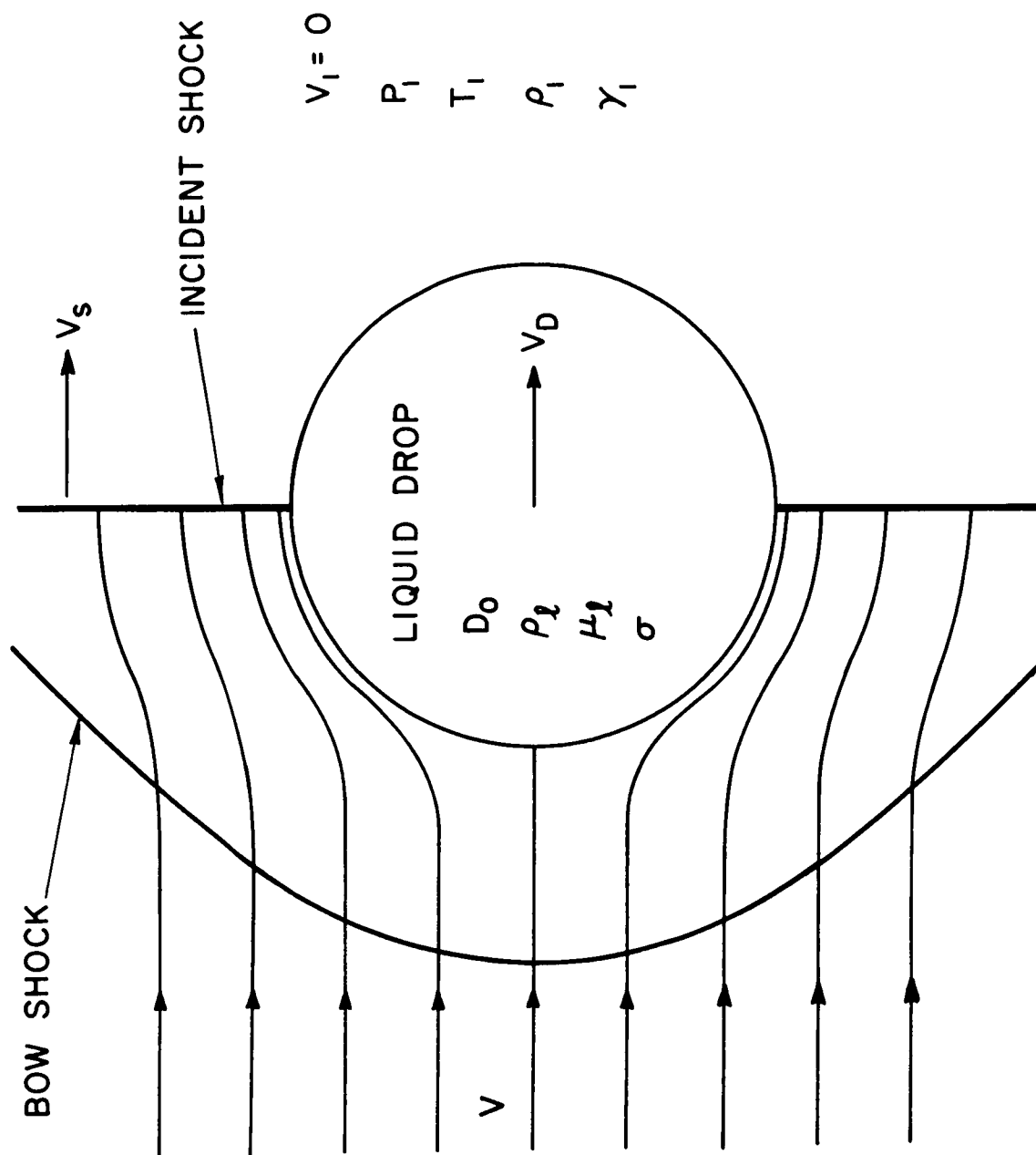


Figure 4.1 Schematic of Shock Wave-Liquid Drop Interaction.

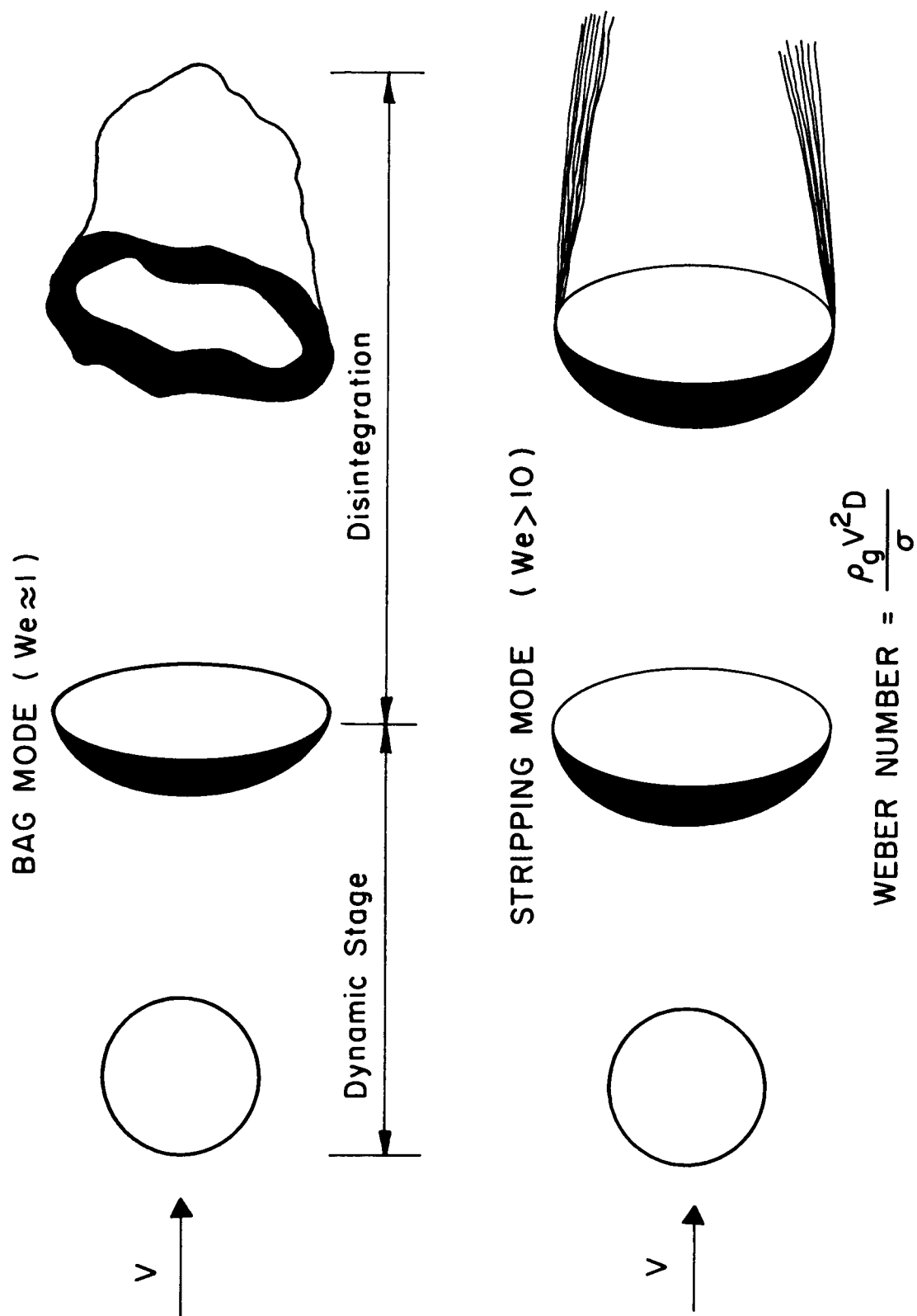


Figure 4.2 The Two Types of Drop Disintegration.

TABLE V. DROP BREAKUP VARIABLES.

Dimensional Variables		Non-Dimensional Variables
Breakup Time	$t_b$	$\tau = t_b V/D$
Drop Diameter	$D$	$We = \rho_g V^2 D / \sigma$
Surface Tension	$\sigma$	$Re_\ell = \rho_g V D / \mu_\ell$
Liquid Viscosity	$\mu_\ell$	$Re_g = \rho_g V D / \mu_g$
Liquid Density	$\rho_\ell$	$M = V/a$
Flow Velocity	$V$	$\beta = \rho_\ell / \rho_g$
Speed of Sound	$a$	
Flow Density	$\rho_g$	
Flow Viscosity	$\mu_g$	

### 1. Experimental Apparatus and Procedure.

The experimental study involves the use of a drop generating system and a shock tube. A single stream of uniform size drops is established in the shock tube normal to the shock velocity and is subjected to shocks of various strengths produced in a helium driven tube. Collimated light from a spark source is utilized to back-light the drops and an image converter camera is employed to photograph the interaction phenomenon. For all of the experiments reported here the initial test section pressure is 1 atmosphere.

The experimental procedure consists of obtaining a time history of the deformation, drift, and disintegration of a water drop by taking a series of photographs, one at a time, at different time intervals after the incident shock wave intercepts it. The wave speed, the drop diameter, and the vertical trajectory of the falling drops are controlled so that the only variable is the time delay in the photographic system. Further details on the experimental facility and procedure can be found in Ref. (3).

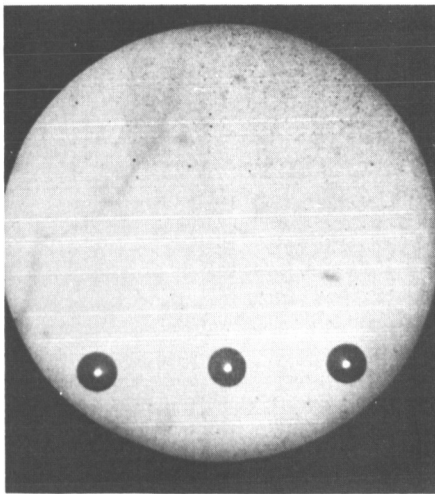


## 2. Results and Discussion.

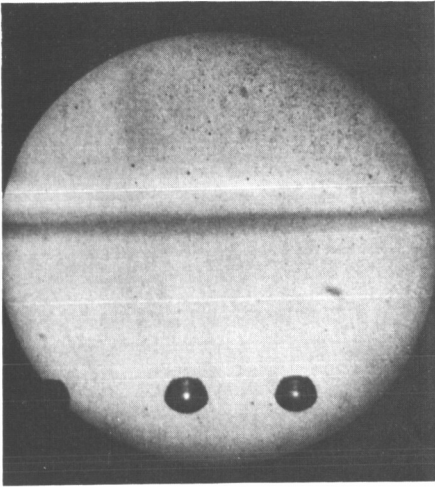
The results discussed here are for experiments that cover the shock Mach number range of  $M_s = 1.5-3.5$  with water drops having diameters in the range  $D_o = 750-2700 \mu$ . Photographs of typical shock wave-water drop interactions are shown in Figs. 4.3-4.6. Drop deformation, displacement, and breakup time correlations are given in Figs. 4.7-4.11.

Figure 4.3 shows the sequence of events leading to the shattering of a stream of  $750 \mu$  drops by a  $M_s = 2.0$  shock wave where initially the convective flow velocity relative to the motionless drop is approximately sonic and equal to 1415 ft/sec. The highlight which appears in the undisturbed drops is an image of the spark light source and it remains very bright and distinct until the growth of capillary surface waves disturbs and finally destroys the drops ability to act as a focusing lens. In this sequence, the highlight disappears between  $7.4 \mu\text{sec}$  and  $8.8 \mu\text{sec}$ , and the planar incident shock wave that is visible in several of the pictures moves from left to right across the drops. The observed breakup can be temporally divided into two rather distinct stages. The first one, or dynamic stage, is the period during which the drops are flattened as a result of the external pressure distributions. The second stage is characterized by a surface stripping process which is produced by the shearing action of the convective flow and which rapidly reduces the drops to clouds of micro-mist. At  $t = 26 \mu\text{sec}$  after the shock made initial contact with the drop, this latter stage is well developed.

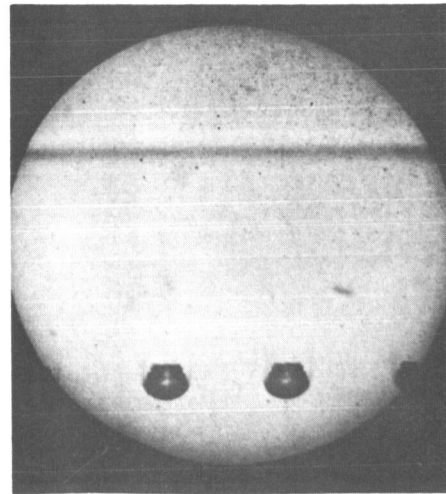
When the incident shock Mach number is increased to  $M_s = 3.0$ , the deformation and disintegration of a drop no longer appear as distinct and separate stages of the breakup but occur almost simultaneously as seen in Fig. 4.4. For example, within only  $10 \mu\text{sec}$  after the shock passage, a significant wake of micro-mist is formed behind the drop, and since the convective flow is supersonic with a Mach number = 1.36, a detached bow shock is also present in the photographs. At  $t = 34 \mu\text{sec}$  capillary surface waves are visible and their wave length



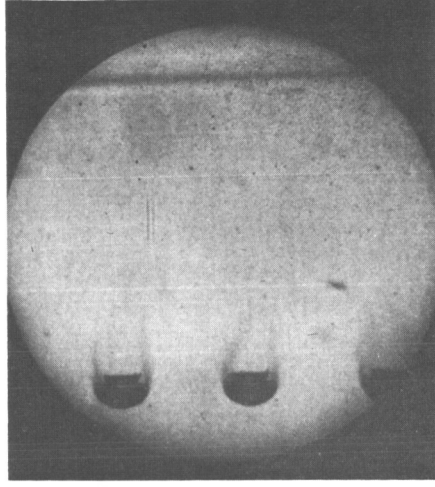
Undisturbed



$t = 5.6 \mu\text{sec}$

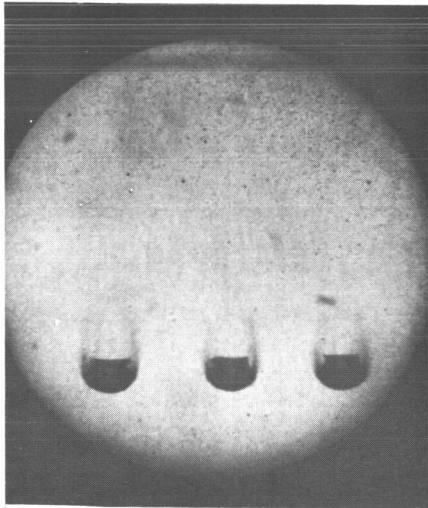


$t = 7.4 \mu\text{sec}$

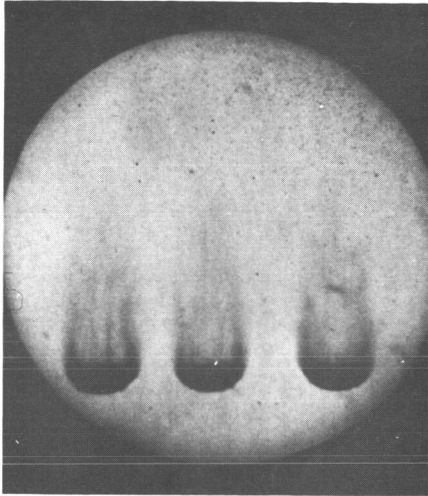


$t = 8.8 \mu\text{sec}$

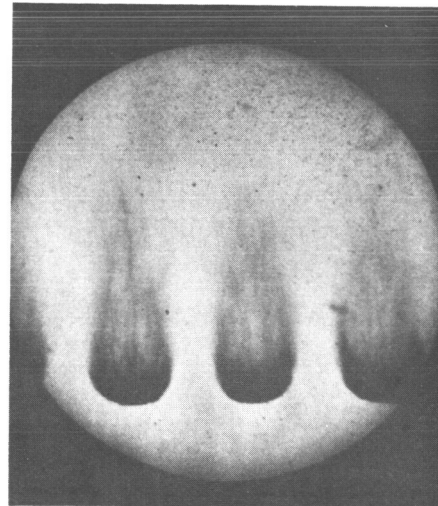
Figure 4.3 The Appearance of  $750 \mu$  Water Drops at Various Times After the Passage of  $M_s = 2$  Shock in Air.



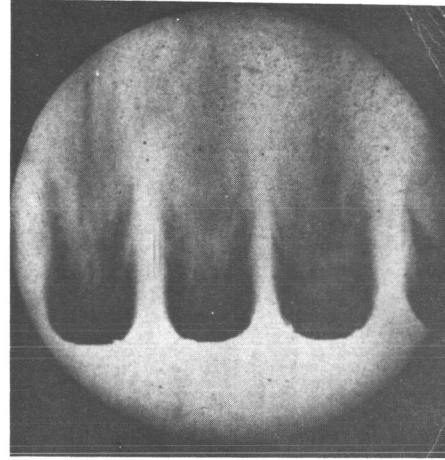
$t = 10.8 \mu\text{sec}$



$t = 15.8 \mu\text{sec}$

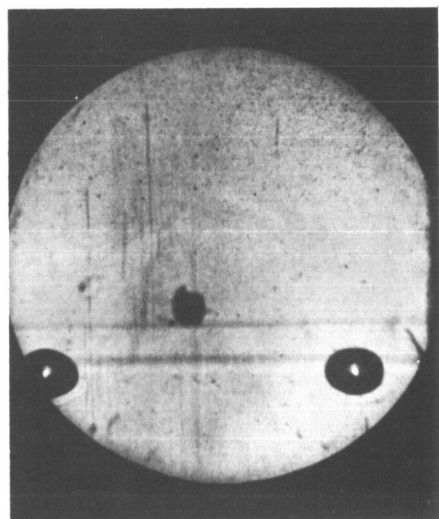


$t = 20.8 \mu\text{sec}$

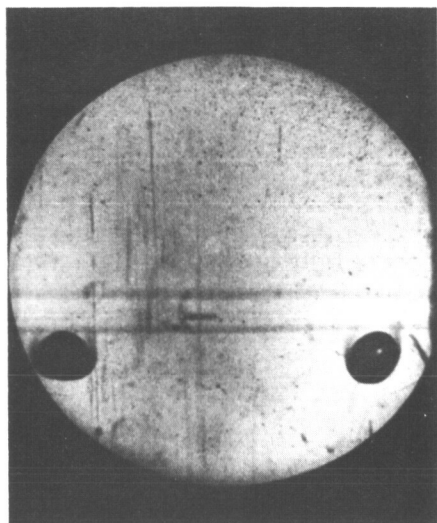


$t = 26 \mu\text{sec}$

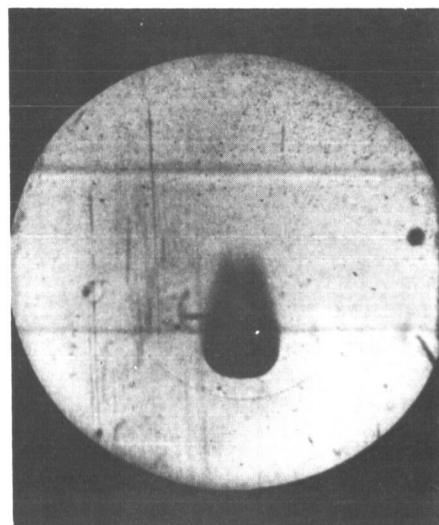
Figure 4.3 (continued) The Appearance of  $750 \mu$  Water Drops at Various Times After the Passage of  $M_s = 2$  Shock in Air.



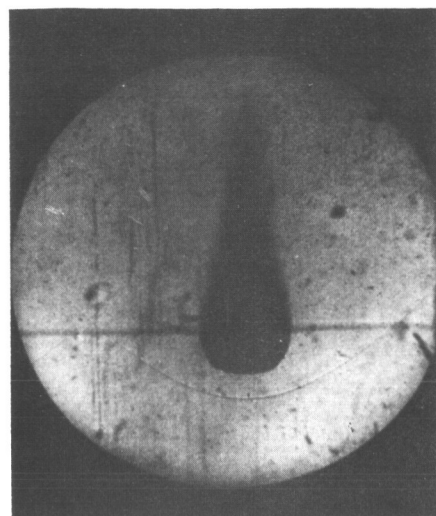
$t = 1 \mu\text{sec}$



$t = 5 \mu\text{sec}$

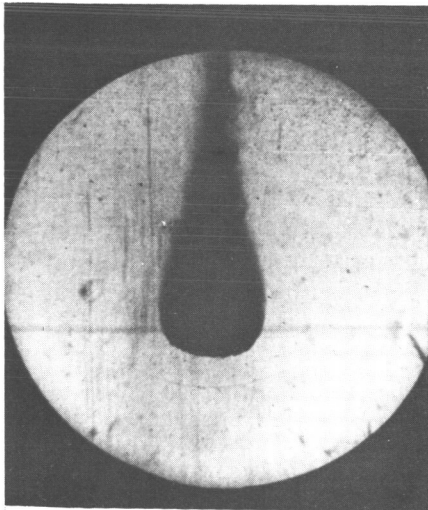


$t = 10 \mu\text{sec}$

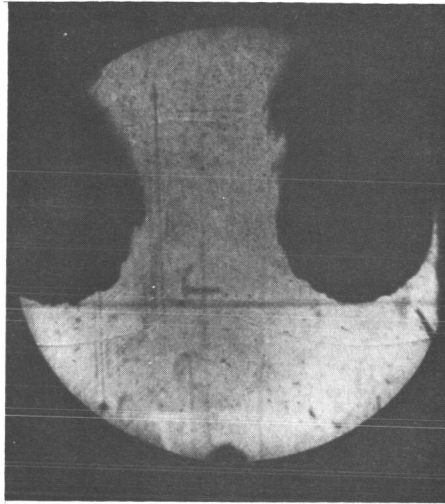


$t = 24 \mu\text{sec}$

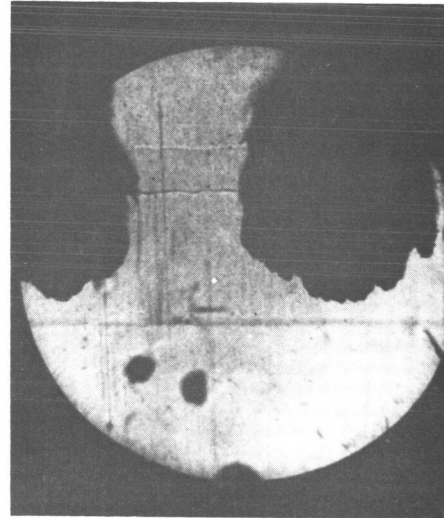
Figure 4.4 The Appearance of  $2700 \mu$  Water Drops at Various Times After the Passage of  $M_s = 3$  Shock in Air



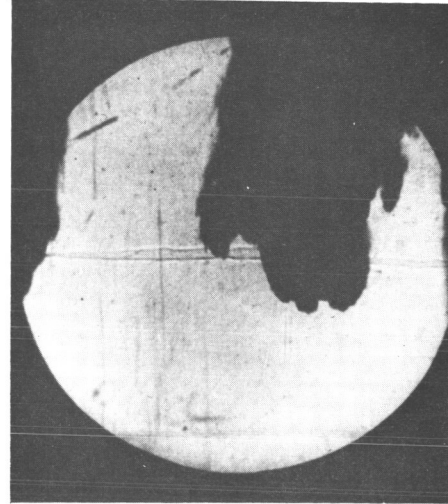
$t = 34 \mu\text{sec}$



$t = 60 \mu\text{sec}$



$t = 72 \mu\text{sec}$



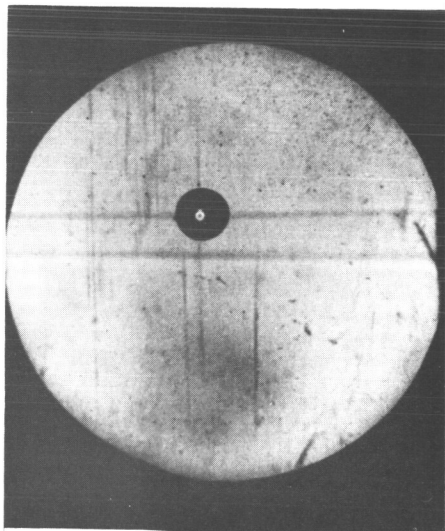
$t = 102 \mu\text{sec}$

Figure 4.4 (continued) The Appearance of  $2700 \mu$  Water Drops at Various Times After the Passage of  $M_s = 3$  Shock in Air.

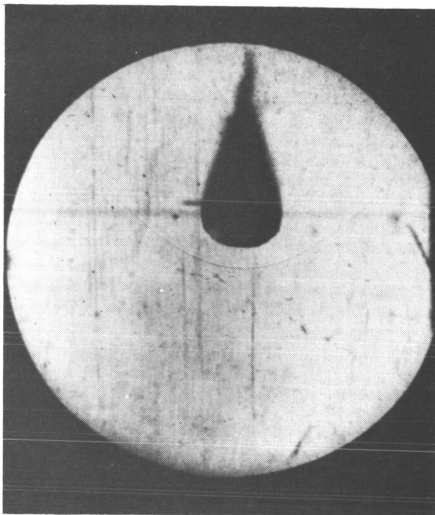
and amplitude increase rapidly until at  $t = 102 \mu\text{sec}$  the drop completely loses its hemispherical shape. The vertical line appearing in all the photographs of this series is a fiducial marker located on the test section windows.

Figures 4.5 and 4.6 are presented to illustrate two important results. First of all, it is observed that in only  $14 \mu\text{sec}$  after a  $M_s = 3.5$  air shock collides with a  $2700 \mu$  drop, a well defined wake is formed behind it. The interesting feature of this wake is that its shape is similar to that developed behind a hypersonic blunt body where the flow, as a result of strong lateral pressure gradients, also converges to form a narrow recompression neck region several body diameters downstream of the rear stagnation point. The very fact that the liquid material being continuously stripped off from the surface of the drop is able to follow the streamline pattern of the wake indicates that the drop is reduced to a fine micro-mist. For if the drop were being eroded away in rather massive pieces, which by reason of their inertia were unable to follow the streamlines, the shape of the wake would be entirely different from the one visible in the photographs. Secondly, the pictures of the  $1090 \mu$  drops, taken at a smaller magnification to include the entire wake, clearly reveal that the breakup is a continuous process of disintegration that begins shortly after the initial contact between a shock and a drop and proceeds until the drop is completely transformed into a cloud of mist. For purposes of this study, the breakup is defined as complete when the wake has the diffuse appearance evident in the photograph taken at  $t = 134.7 \mu\text{sec}$  after shock passage.

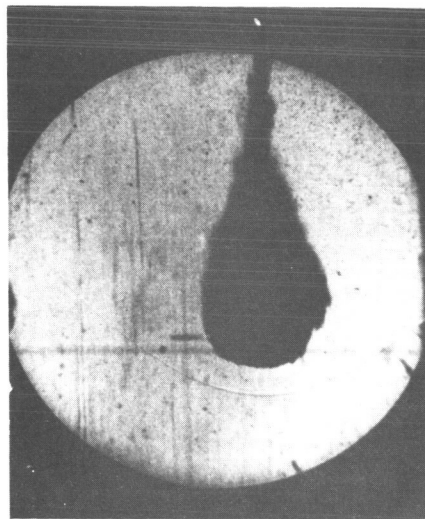
The deformation of a drop as defined by the ratio of maximum diameter to the original diameter is plotted in Fig. 4.7 as a function of time. One observes that the time required to reach an equivalent state of deformation decreases and the maximum diameter attained increases as the incident shock Mach number goes from  $M_s = 1.3$ - $3.5$ . For example, when  $M_s = 1.3$ , the time required for a  $2700 \mu$  drop to reach its maximum deformation of  $2.3 D_0$  is  $230 \mu\text{sec}$  whereas at  $M_s = 3.5$  it only takes  $55 \mu\text{sec}$  to attain a deformation ratio of  $3.8$ .



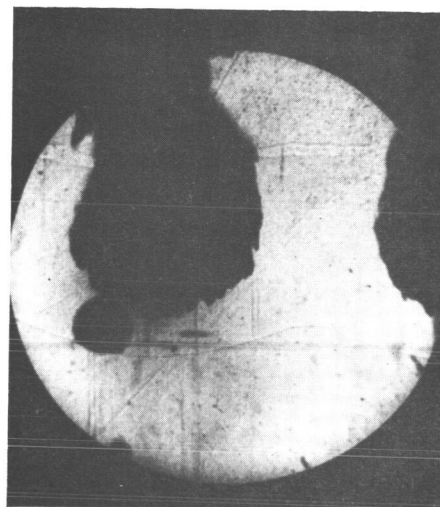
Undisturbed



$t = 14 \mu\text{sec}$



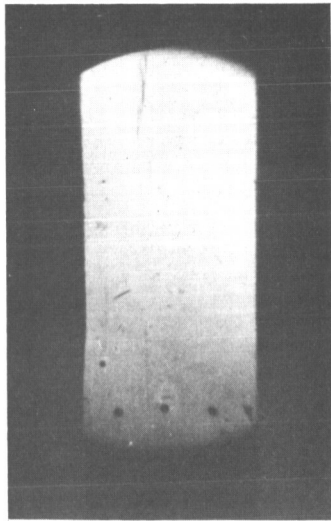
$t = 26 \mu\text{sec}$



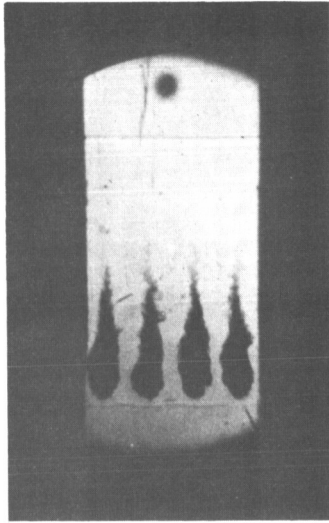
$t = 59 \mu\text{sec}$

Figure 4.5 The Appearance of  $2700 \mu$  Water Drops at Various Times After the Passage of  $M_s = 3.5$  Shock in Air.

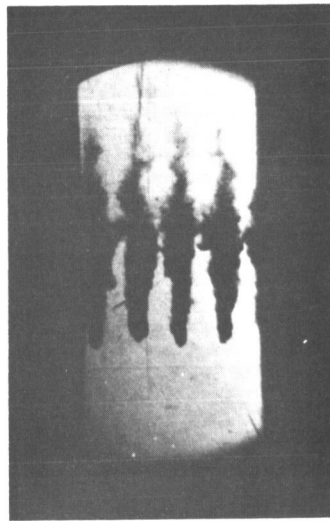




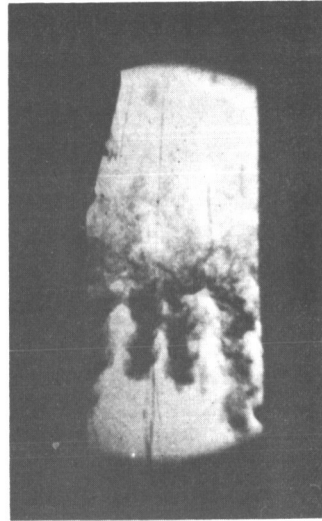
Undisturbed



$t = 38.8 \mu\text{sec}$



$t = 69.8 \mu\text{sec}$



$t = 134.7 \mu\text{sec}$

Figure 4.6 The Appearance of  $1090 \mu$  Water Drops at Various Times After the Passage of  $M_s = 3.25$  Shock in Air.



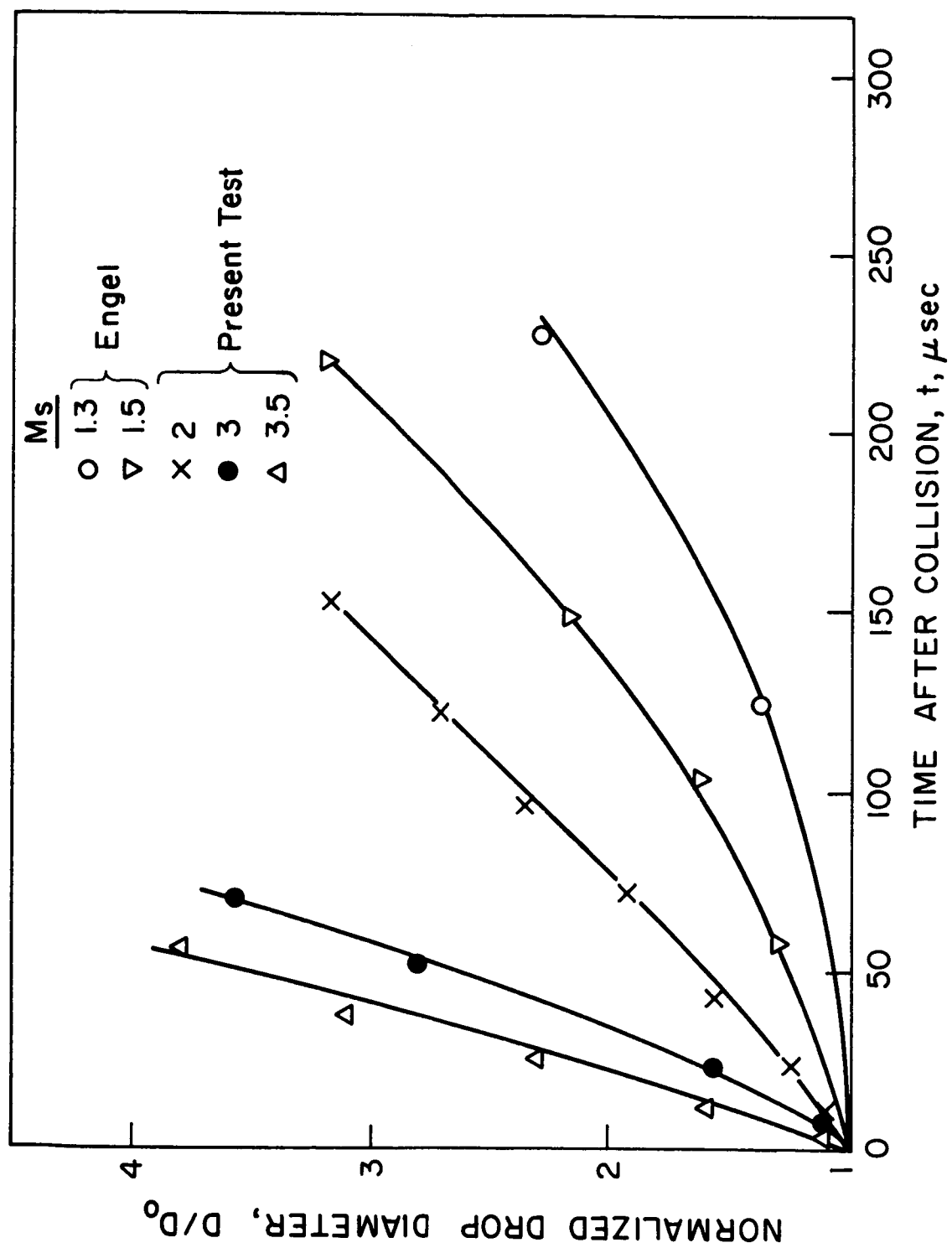


Figure 4.7 Deformation of 2700 μ Drop.

Typical displacement data obtained from the experiments are plotted in Fig. 4.8. The parabolic curves represent the best parabolic fit to the data. Excellent fit is evident at the initial phase of the breakup, but in the later phase deviations can be observed. This suggests that, while initially the drop acceleration is constant, it does not remain constant during the latter portion of the breakup. Physically this indicates that approximately midway through the breakup period the mass of a drop is decreasing at a rate faster than the drag forces are diminishing and the net effect is an increase in the drop acceleration.

The data also show that the distance moved by a drop in a given period of time is considerably greater at the higher Mach numbers than at the lower ones. For example, a  $2700\ \mu$  drop moves one inch in  $150\ \mu\text{sec}$  when  $M_s = 3.5$  whereas at  $M_s = 1.5$  it takes over  $800\ \mu\text{sec}$  to translate the same distance. Calculations made from the displacement data for a  $1090\ \mu$  drop at  $M_s = 3.3$  give the velocity at the instant of breakup as  $V_D = .9V$  and the acceleration as  $.5 \times 10^6\ \text{g's}$ . The above data are plotted in a non-dimensional form in Fig. 4.9 where the present tests are compared with those of Engle<sup>(17)</sup> and Nicholson<sup>(20)</sup>. All of the displacement curves contained in Fig. 4.8 reduce to a single parabola given by  $\bar{X} = .714 \bar{T}^2$ .

The effect of incident shock strength on the time required to break a drop of a given diameter is shown by the information given in Fig. 4.10. For example, less than  $100\ \mu\text{sec}$  is required to completely disintegrate a  $900\ \mu$  drop at  $M_s = 3.5$  whereas  $360\ \mu\text{sec}$  is needed when  $M_s = 1.5$ . The apparent discrepancy between Nicholson's<sup>(20)</sup> data and these results is explained by the fact that Nicholson used various initial pressures,  $p_1 < p_{\text{atm}}$ , in the test section for purposes of altitude simulation studies. Since a reduction in the initial driver section pressure has the effect of producing a lower dynamic pressure for a given shock Mach number, the breakup times he observed were larger than those produced in either this or Engel's<sup>(17)</sup> study.

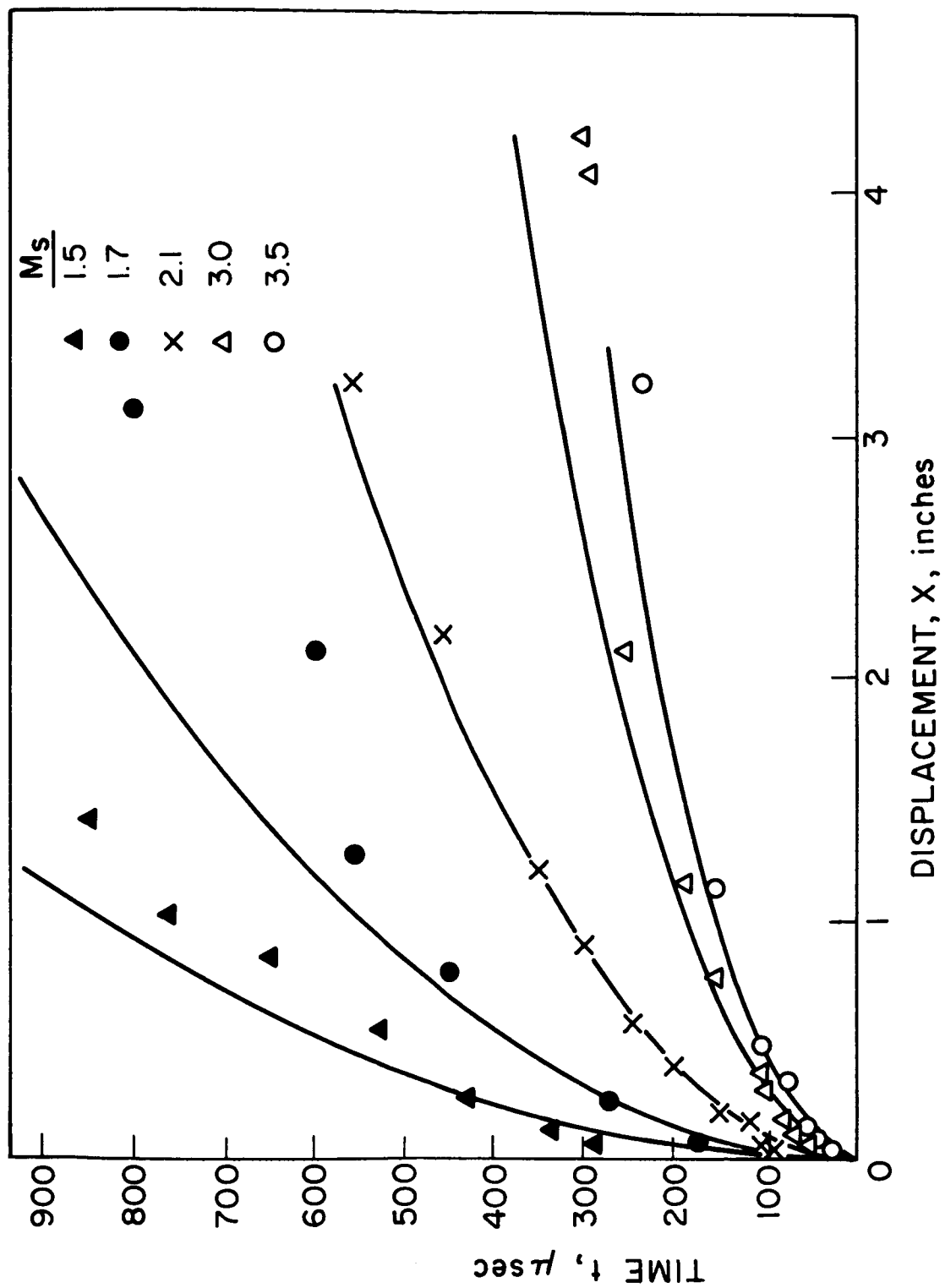


Figure 4.8 Displacement of  $2700\ \mu$  Water Drop After Passage of Wave.

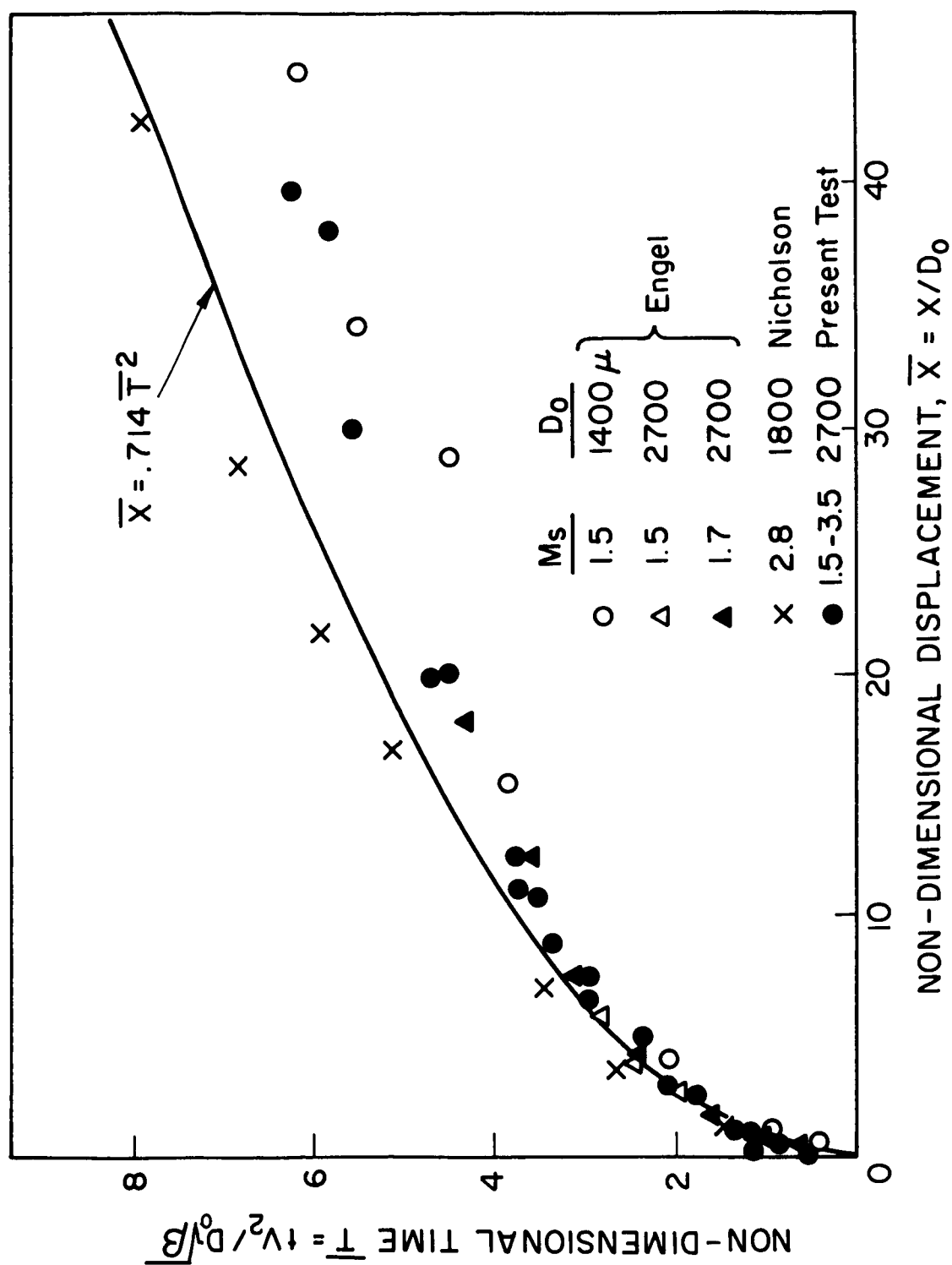


Figure 4.9 Non-Dimensional Displacement vs. Non-Dimensional Time.

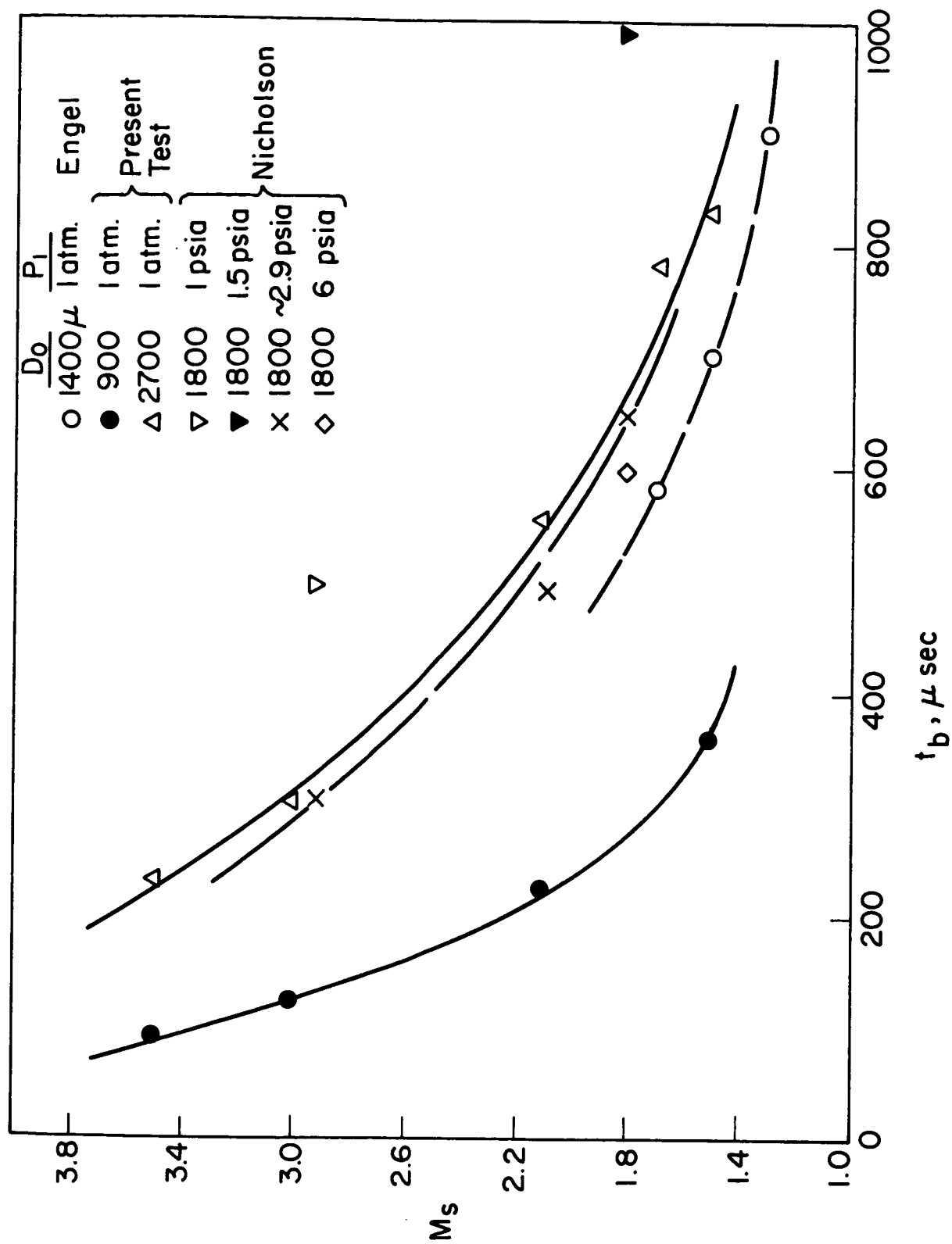


Figure 4.10 Effect of Shock Mach Number on the Breakup Time.

Nicholson correlated his measured breakup times of water drops with dynamic pressure and arrived at an empirical equation  $t_b/D_o = q^{-1/2}$ , when  $t_b$ ,  $D_o$  and  $q$  are expressed in  $\mu\text{sec}$ ,  $\mu$  and  $\text{psi}$  respectively. This equation is shown as the solid line in Fig. 4.11. Some of the data from the present tests along with three points from Engel's study are also included. A curve described by  $t_b/D_o = 2.1 q_2^{-1/2}$  fits the data of the present study fairly well at the high values of dynamic pressure, but not at the lower values. The disparity between our data and that of Nicholson's can partly be attributed to the difference in the definition of breakup time. Furthermore, in our data, there seems to be a systematic difference between the  $900 \mu$  and  $2700 \mu$  data which can mean a size effect.

The data of Engel and of the present tests, contained in Fig. 4.11, is re-plotted in Fig. 4.12 to show the variation of the dimensionless breakup time,  $\tau = t_b V_2/D_o$  with  $M_2, \beta$ ,  $We$ , and  $Re_g$ . It is interesting to observe that the dimensionless breakup time remains essentially constant and approximately equal to 100 throughout the experimental range. Since it was impossible in the experiments to vary only one dimensionless variable at a time, no definite conclusion can be drawn from such a plot. Modification of our shock tube is now started so that a systematic change in the variables can be made.

Our breakup data can also be compared with breakup data of Morrell and Povinelli<sup>(22)</sup> on water jets. These authors find that when  $We/\sqrt{Re_g} \gg 1$ , a condition applying to most of the data in Fig. 4.12, the nondimensional time can be reduced to, in our notation,

$$\tau = .54 \beta^{2/3} \left( \frac{\mu_2}{\mu_\ell} \right)^{1/3} \frac{Re^{3/4}}{We^{1/2}} \quad (4.2)$$

If representative values within the range of conditions for our data are substituted into this equation, one obtains a nearly constant  $\tau \approx 60$  as opposed to 100 found above. The difference could be due to geometry, but this will have to be checked.

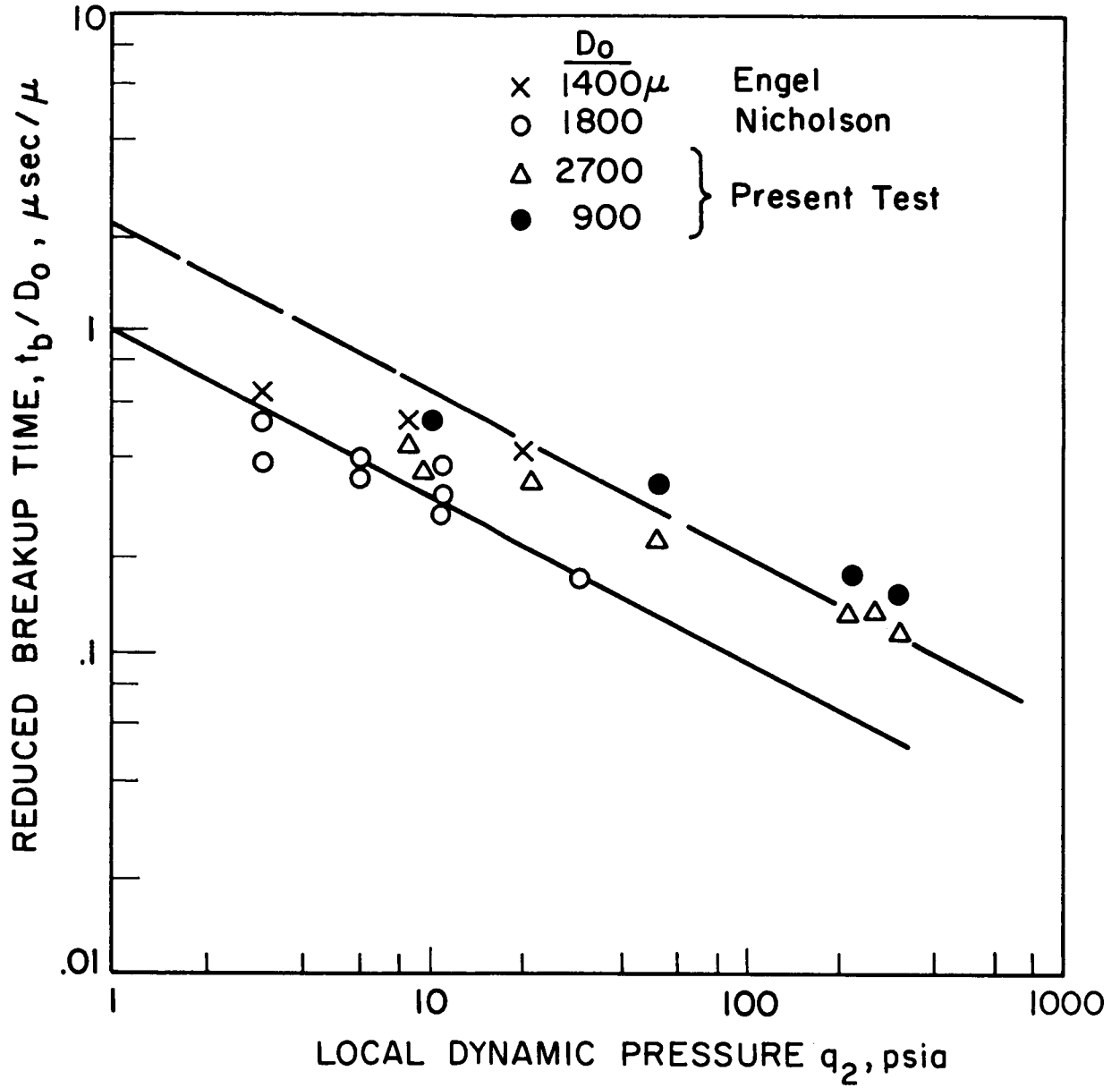


Figure 4.11 Breakup Time Correlation with the Dynamic Pressure.

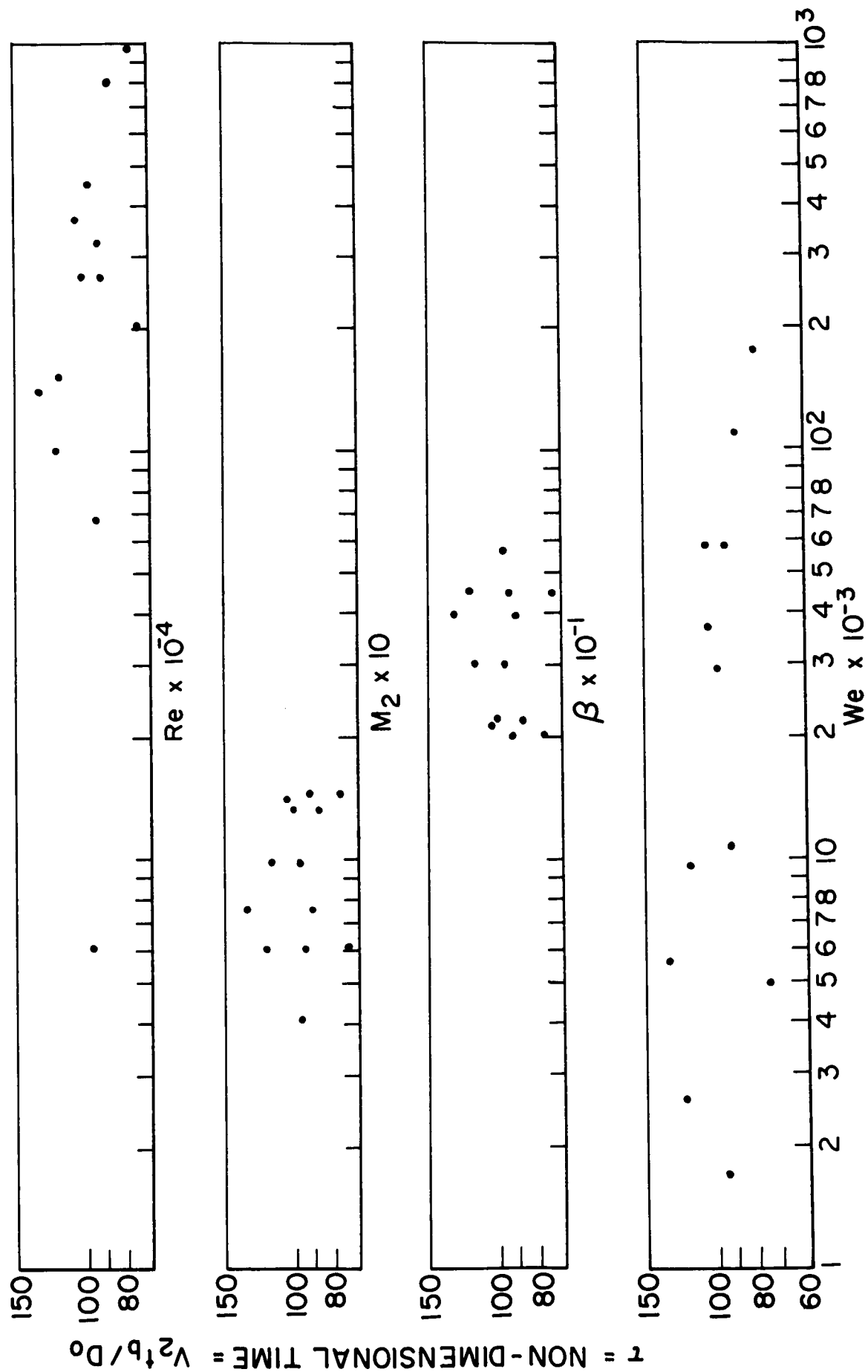


Figure 4.12 Correlation of Non-Dimensional Time with  $Re_g$ ,  $We$ ,  $M_2$  and  $\beta$ .



## V. SUMMARY OF RESULTS

1. The detonation velocity of  $940\ \mu$  spray varies from 5500 to 6950 ft/sec as the equivalence ratio changes from .18-.96. The variation follows the theoretical trend, but in general, the experimental velocities are lower than the theoretical.
2. Detonation can easily be initiated in a single stream of  $2600\ \mu$  diameter drops. For an equivalence ratio of 0.23 a propagation velocity of 3,700 - 4,000 ft/sec is reached.
3. The reaction zone of the detonation of  $2600\ \mu$  diameter drops appears to be  $\sim 2$  ft long. Secondary shocks produced by the burning drops provide a powerful mechanism for driving the initial shock front.
4. "Retonation" has been induced within the reaction zone of two-phase detonations by means of a "step" in the wall of the combustion tube.
5. A piezoelectric pressure transducer has been developed which minimizes the "ringing" within the transducer and is capable of resolving pressure fluctuations within the two-phase detonations.
6. Pressure measurements behind the shock front of the detonation show, at times, an increase in pressure which can be attributed to the presence of secondary shocks.
7. Heat transfer to the wall within the reaction zone is approximately  $1000\ \text{Btu/ft}^2\text{-sec}$  for the  $2600\ \mu$  diameter drops and could possibly be as high as  $10,000\ \text{Btu/ft}^2\text{-sec}$  initially for the  $940\ \mu$  diameter drops.
8. Trajectories of the  $2600\ \mu$  diameter drops within the detonation reaction zone have been obtained with streak photographs. The breakup time of a burning drop appears to be longer and the maximum displacement considerably less than a non-burning drop in a shock tube.

9. Difference equations for two-phase detonations of spray and liquid films which include frictional effects and heat loss within the reaction zone gives improved agreement with experiment when applied.
10. Detonation velocities in the  $940\ \mu$  spray are closer to the theoretical than those of the  $2600\ \mu$  drop stream for the same mixture ratio.
11. The breakup of inert drops by shock waves is observed to occur mainly as a result of the interaction between a drop and the convective flow field established by the shock. The disintegration process is a continuous one which begins almost instantaneously after interaction with an incident shock wave. It is characterized by a transformation of a liquid drop into a disperse micro-mist by the mechanism of shearing on the drop periphery.
12. The acceleration of the inert drops is approximately constant up to the end of the breakup time.
13. The breakup time of inert drops is approximately proportional to the drop diameter and the inverse of the convective velocity.

## APPENDIX

### 1. Pressure Measurement.

In order to better understand the reaction zone of heterogeneous detonations, measurement of static sidewall pressures over a wide-band frequency range from DC to above 1 MHz and for relatively long times was needed. In Refs. (1) and (3) such pressure data was obtained with Kistler model 603 and 601A transducers. These transducers consist of a thin metal diaphragm, a disk of metal for mass, and quartz crystals which produce an electric charge when stressed in accordance with the piezoelectric effect. A faithful reproduction of the pressure in the high frequency range is difficult to achieve because of reflected elastic waves in the sensing element. Filtering the output signal leaves much to be desired. The new Kistler model 603A with "acceleration compensation", while better in this regard, does not give satisfactory results for our work either.

Since pressure transducers which would satisfactorily meet our requirements were, to our knowledge, not available commercially, a design study based primarily on the work of Zaitsev<sup>(23)</sup> and Soloukhin<sup>(24)</sup> was initiated. The main objective was to eliminate the reflected elastic waves in the sensing element by an appropriate design of the transducer. Further, many piezoelectric materials are now available which have superior properties compared to those of quartz and therefore can be used to advantage in the design of a pressure transducer. Before the design of a new transducer is presented, the performance of several Kistler transducers under various conditions of interest will be documented.

#### a. Response of Kistler Transducers.

The response of Kistler model 603, 601A and 603A pressure transducers to a 1 atm stoichiometric hydrogen-oxygen gaseous detonation in a 1/2 x 3/8 in. tube is shown in Fig. A. 1. (The use of gaseous detonation was found to be a simple, repeatable method of producing conditions similar to those encountered in heterogeneous detonations.) All the Kistler transducers were attached to

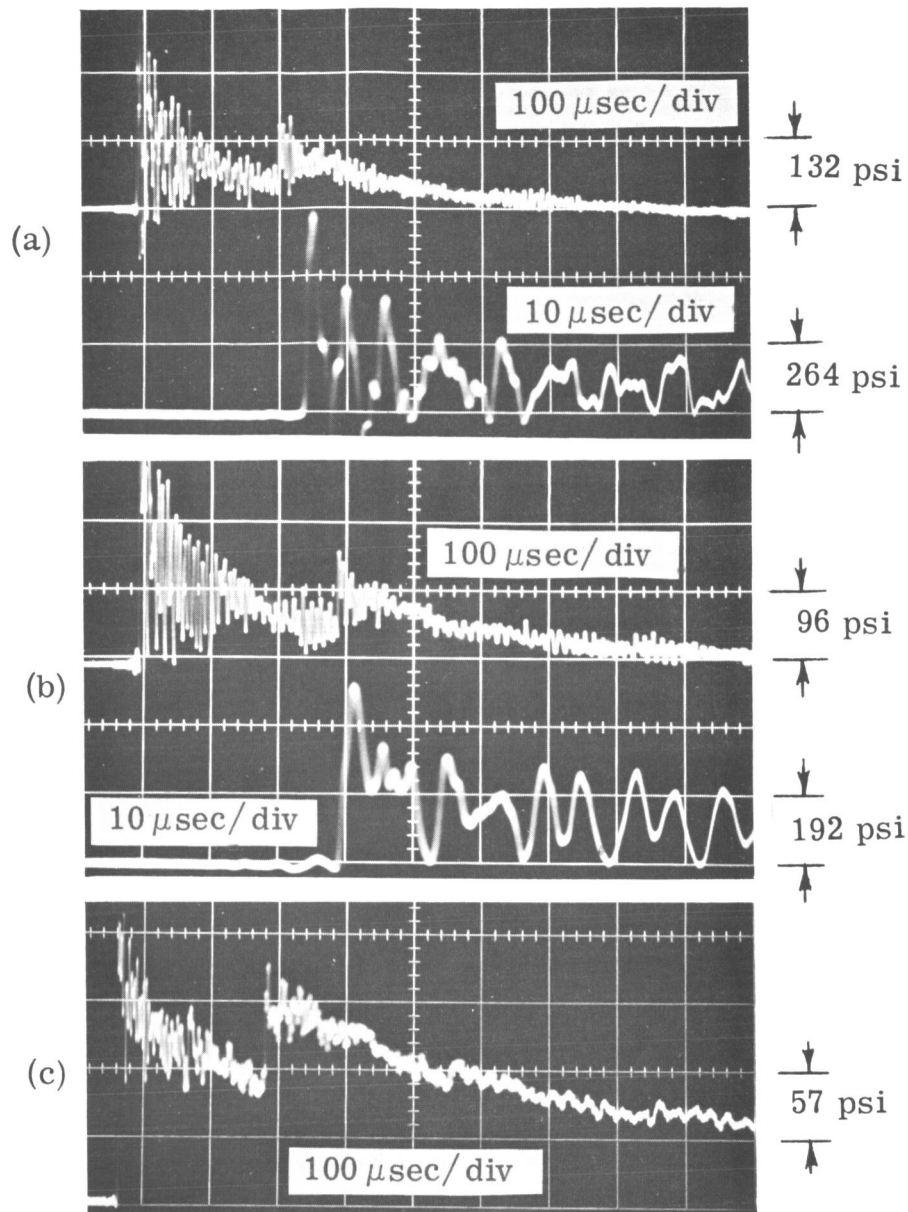


Fig.A. 1 Response of Kistler pressure transducers to a 1 atm stoichiometric hydrogen-oxygen gaseous detonation.

- (a) Model 603, no filter; charge amplifier at 1 mV/pCb  
Upper beam: 132 psi/div and 100  $\mu$ sec/div. Lower beam: 264 psi/div and 10  $\mu$ sec/div.
- (b) Model 601A, no filter; charge amplifier at 1 mV/pCb  
Upper beam: 96 psi/div and 100  $\mu$ sec/div. Lower beam: 192 psi/div and 10  $\mu$ sec/div.
- (c) Model 603A, no filter; charge amplifier at 10 mV/pCb  
57 psi/div and 100  $\mu$ sec/div.

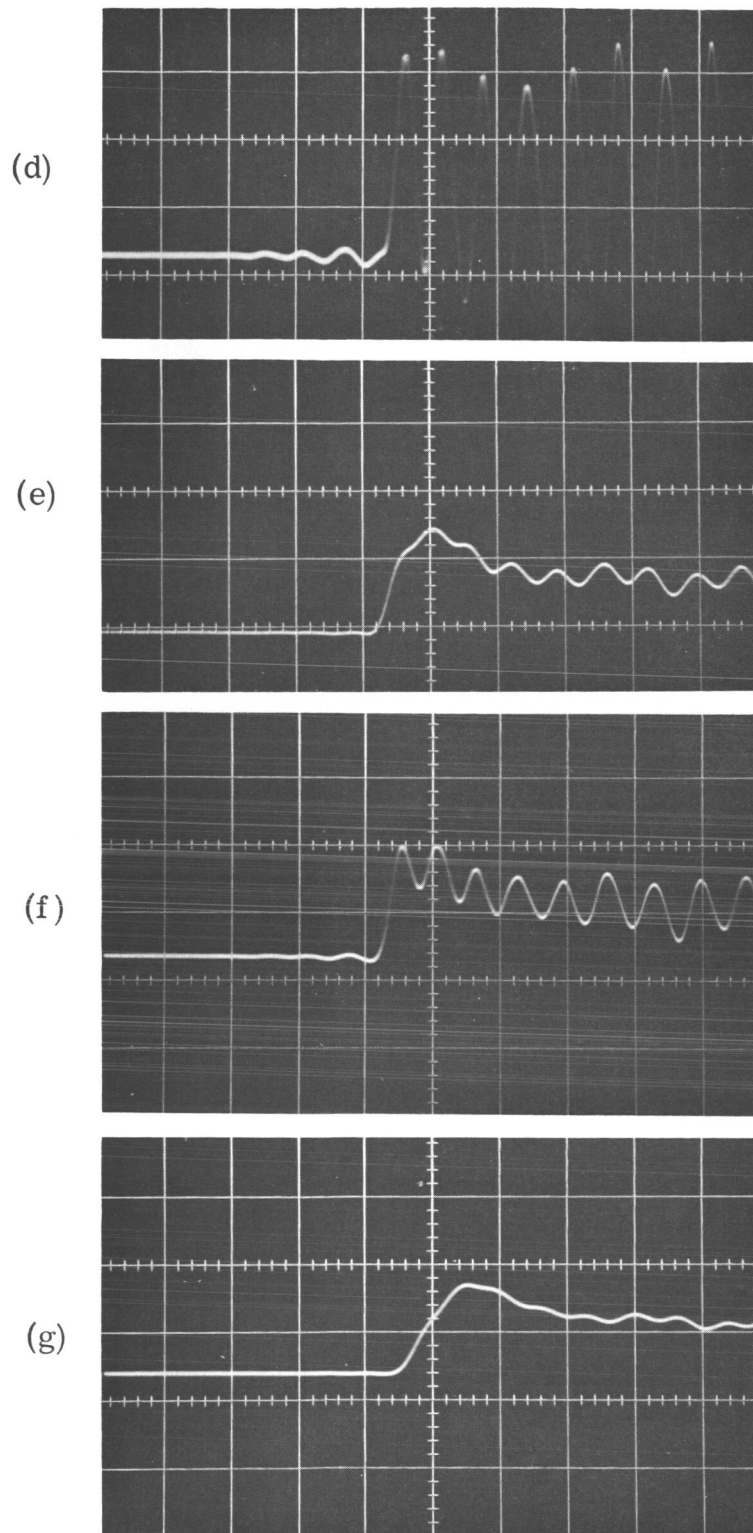


Fig. A. 1

- (d) Model 601A, no filter; charge amplifier at 10 mV/pCb  
192 psi/div and 10  $\mu$ sec/div.
- (e) same as (d) except with Kistler 544-A50 output filter.
- (f) same as (d) except with 27,000  $\Omega$  input filter.
- (g) same as (d) except with both input and output filters.

25 ft of low-noise Kistler cable, a Kistler charge amplifier model 566, and a Tektronix oscilloscope model 555 with type M plug-in-units. The verticle scale is determined from static calibrations. For models 603 and 601A the unfiltered output has an initial overshoot of at least 100% and a natural frequency of about 200 KHz. The second pressure rise is caused by the return of the reflected shock from the end of the closed tube. The model 603A, which recently became available and has "acceleration compensation," has somewhat improved response as shown in Fig. A.1(c), but it is not considered satisfactory to probe the reaction zone of a heterogeneous detonation. In all cases it is difficult to assign a peak pressure to the detonation wave because of the overshoot and the trailing rarefaction wave.

The effect of filtering the signal into or out of the charge amplifier is shown in Fig. A.1(d-g). While the ringing is minimized, the rise time is increased and the signal is attenuated as a function of frequency, and thus it is still difficult to interpret the pressure level and to separate the dynamic response of the transducer from true fluctuations in the gas.

#### b. Pressure Transducer with Acoustic Absorbing Rod.

A diagram of the pressure transducer as built in this laboratory is shown in Fig. A.2. The pressure sensing element is made of lead metaniobate ( $\text{PbNb}_2\text{O}_6$ ). Tin was chosen as the material for the acoustic absorbing rod because the acoustic impedance ( $\rho C = 1.99 \times 10^6 \text{ gm/cm}^2 \text{ sec}$ ) closely matches the acoustic impedance of the lead metaniobate ( $\rho C = 1.92 \times 10^6 \text{ gm/cm}^2 \text{ sec}$ ). The rod was made 6.5 in. long to give a theoretical "ring free" time of  $120 \mu\text{sec}$ . The rod was faced off on a lathe; no special lapping was done. Lead metaniobate was commercially available in 1 in. diameter disks 0.050 in. thick, silvered on both sides. These disks were cut to size with an ultrasonic drill using a  $1 \mu$  boron slurry, and with this technique a  $1/8$  in. diameter was the minimum size that could be cut satisfactorily. Indium solder (Indalloy No. 1, Indium Corp. of America, Utica, N.Y.) which is a 50% indium, 50% tin alloy was used

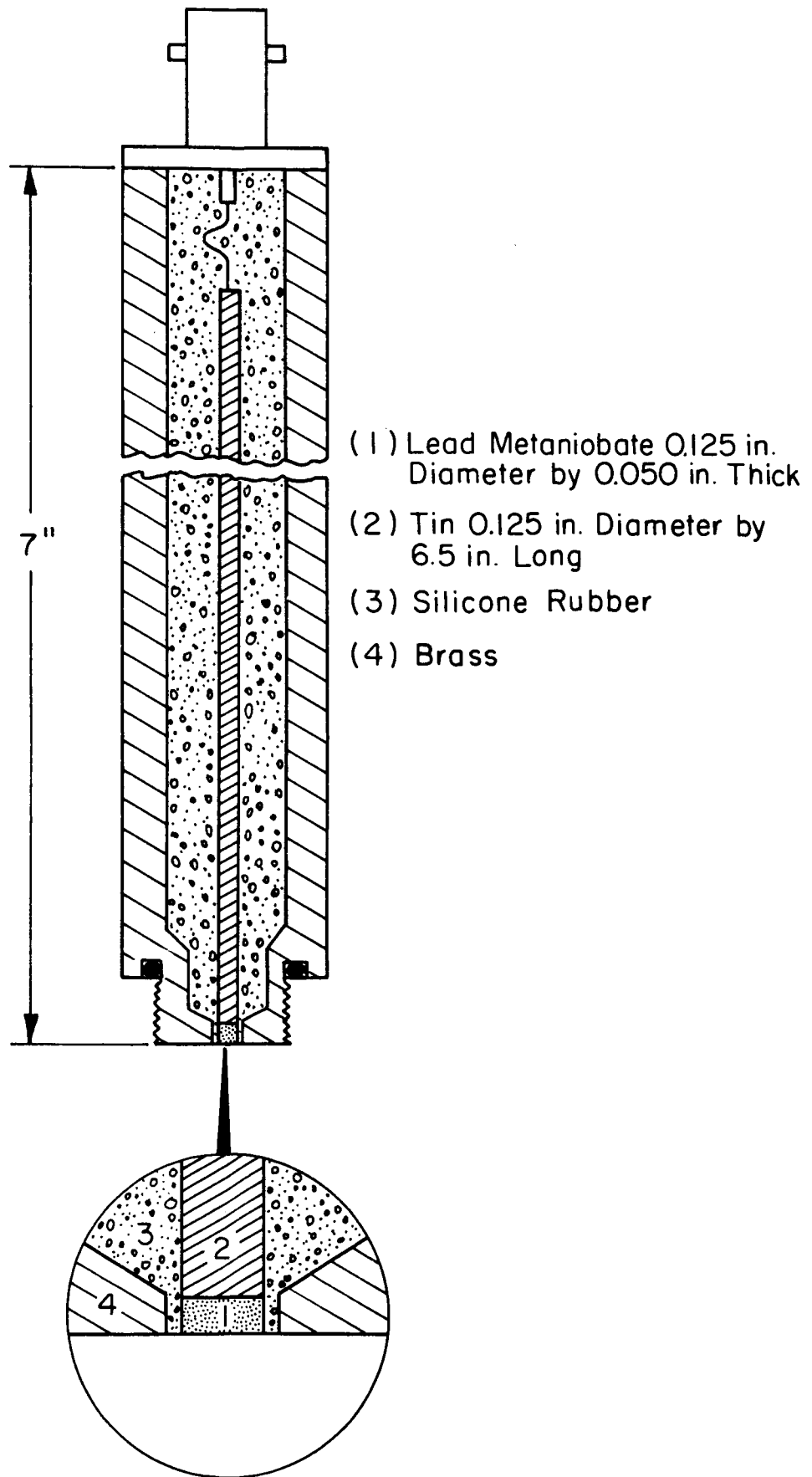


Figure A.2 Pressure Transducer with Acoustic Absorbing Rod.

to join the lead metaniobate disk to the tin rod. No flux was used; however, it was found that a slight amount of precipitated silver powder on the surface of the disk greatly improved the solderability. The rod assembly was then positioned in a brass housing and potted in silicone rubber (Silastic 521, Dow Corning Corp., Midland, Mich.) to provide electrical and mechanical isolation. The clearance between the brass and the pressure sensing element was held to 0.015 in. to minimize longitudinal compression of the silicone rubber. One electrical connection is made at the end of the tin to a BNC connector and the other is made from the sensor to the case with silver doped epoxy and/or a thin wire soldered across the silicone rubber gap.

The choice of lead metaniobate requires some discussion. Quartz has been used extensively to date; however, it appears in general to have less desirable properties as a pressure transducer material than several ceramic piezoelectric materials such as lead titanate zirconate and lead metaniobate. Some of the pertinent properties are listed in Table V as obtained from manufacturer's data and Jaffe<sup>(25)</sup>. The charge generated by a single piezoelectric element is equal to the piezoelectric constant times the frontal area of the element times the pressure. The greater charge output of the ceramics is apparent, but of particular interest is the low cross-axes sensitivity of the lead metaniobate compared to the longitudinal mode. The voltage output is given by the charge generated divided by the capacitance of the element, housing and cable. The capacitance of the element equals the dielectric constant times the area divided by the thickness of the element. Since the capacitance of the housing and cable of this design is generally at least 100 pF, the relatively high dielectric constants of the ceramics is not a disadvantage in terms of output voltage level. Lead metaniobate is also of interest for pressure transducers because of its very low mechanical Q—a parameter which indicates the internal damping of the material. Quartz, on the other hand, has very little damping effect, and thus reflected elastic waves in the crystal continue for relatively long periods of time. The two ceramic materials have Curie temperatures comparable to quartz, and



TABLE VI. PROPERTIES OF SEVERAL PIEZOELECTRIC DISKS NORMAL  
TO THE DIRECTION OF THE APPLIED FORCE.

Piezoelectric Material	Piezoelectric Constant (pCb/N)	Dielectric Constant (relative to air)	Mechanical Q	Curie Point (°C)	Velocity of Compressional Wave (m/sec)	Density (gm/cm <sup>3</sup> )	Acoustic Impedance (gm/cm <sup>2</sup> sec) x 10 <sup>6</sup>
Quartz longitudinal radial	2.3 2.3	4.5 4.5	10 <sup>6</sup>	550	5750	2.65	1.52
Barium titanate longitudinal radial	190 -78	1700 1700	300	115	4300	5.7	2.45
Lead zirconate titanate (PZT5A)* longitudinal radial	374 -171	830 830	75	365	4350	7.75	3.36
Lead metaniobate (278)** longitudinal radial	75 -12	240 240	5 10	550	3200	6.0	1.92

---

\* Clevite Corp., 232 Forbes Road, Bedford, Ohio

\*\* General Electric Corporation, 1501 Roanoke Boulevard, Salem, Virginia

the piezoelectric and dielectric constants vary little with temperature changes from 20°C to 200°C or more. Finally the velocity of a compressional wave, density and acoustic impedance are given in Table VI. Copper is a good acoustic match for PZT, while tin is an excellent match for lead metaniobate. However, PZT-copper transducers assembled in the same manner gave inferior results compared to the lead metaniobate-tin combination.

In recording a high frequency signal from the transducer, the output signal was shunted by .01  $\mu$ F and connected directly to a Tektronix 555 oscilloscope, which has an input impedance of  $10^6$  ohms. This procedure results in an RC time constant of 10 msec and gives satisfactory results for sweep times less than 1 msec provided that the pressure jumps of interest are several hundred psi. In cases where the pressures are lower and/or the times of interest longer it is desirable to increase the input impedance of the recorder. An insulated gate field effect transistor in a common source configuration, as shown in Fig. A. 3, was found to be a simple means of obtaining an input impedance of the order of  $10^{14}$  ohms. The circuit used has a gain of .76 and an input current of less than 0.5 nA with 4V input. This circuit was used for static calibration of the transducers; over the investigated range of 100 to 1000 psi the output of the transducer was quite linear.

The response of the pressure transducer flush mounted in the side-wall of a conventional 1.5 x 2.5 in. shock tube and in a 1/2 x 3/8 in. detonation tube is shown in Fig. A. 4. In Fig. A. 4(a) the response to a Mach 3.2 shock at a pressure level of 156 psig is presented. The rise time of the signal is 2.5  $\mu$ sec which is associated primarily with the time for the shock to traverse the face of the sensing element. The spurious signals are quite small. The response to a 2 atm stoichiometric hydrogen-oxygen detonation at a peak pressure level of 500 psi is given in Fig. A. 4(b). Here some precursor transverse vibration is evident (no attempt to shock mount the transducer case was made). Reflected shocks from a flanged joint and the end of the tube also

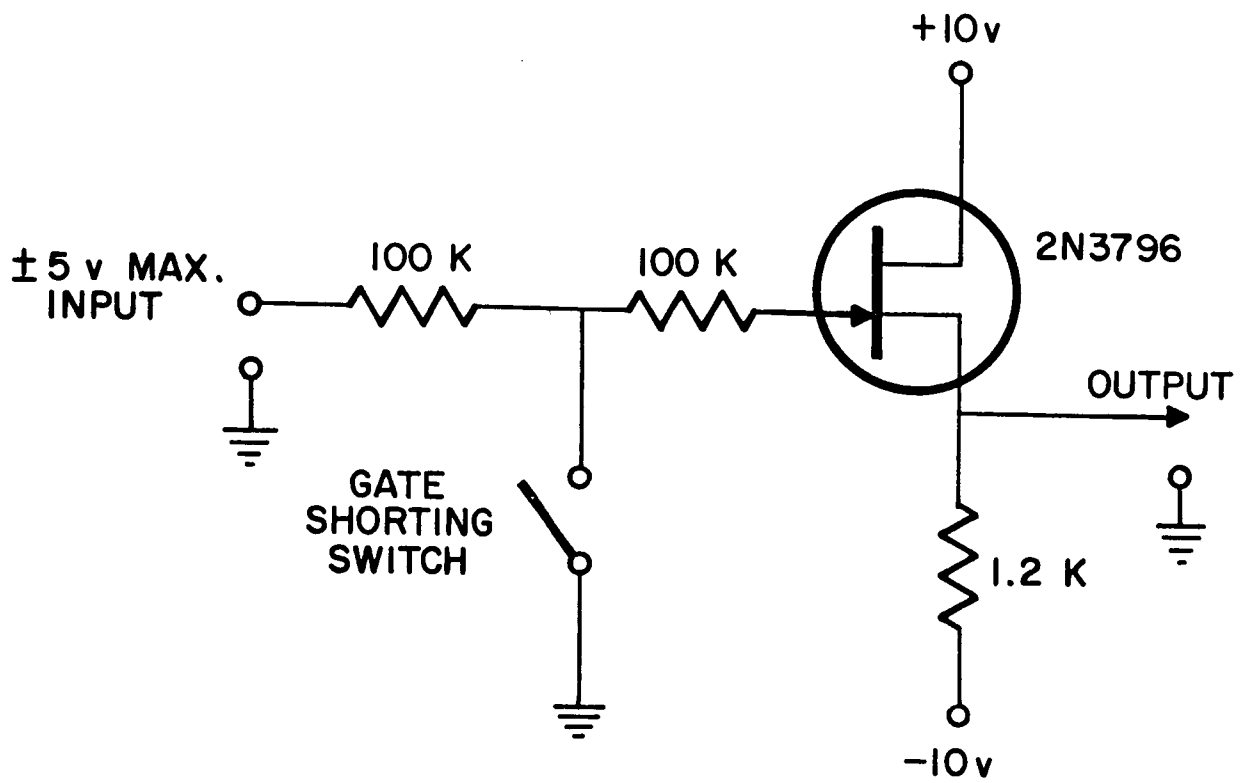


Figure A. 3 High Impedance Circuit for the Pressure Transducer Utilizing a Field Effect Transistor.

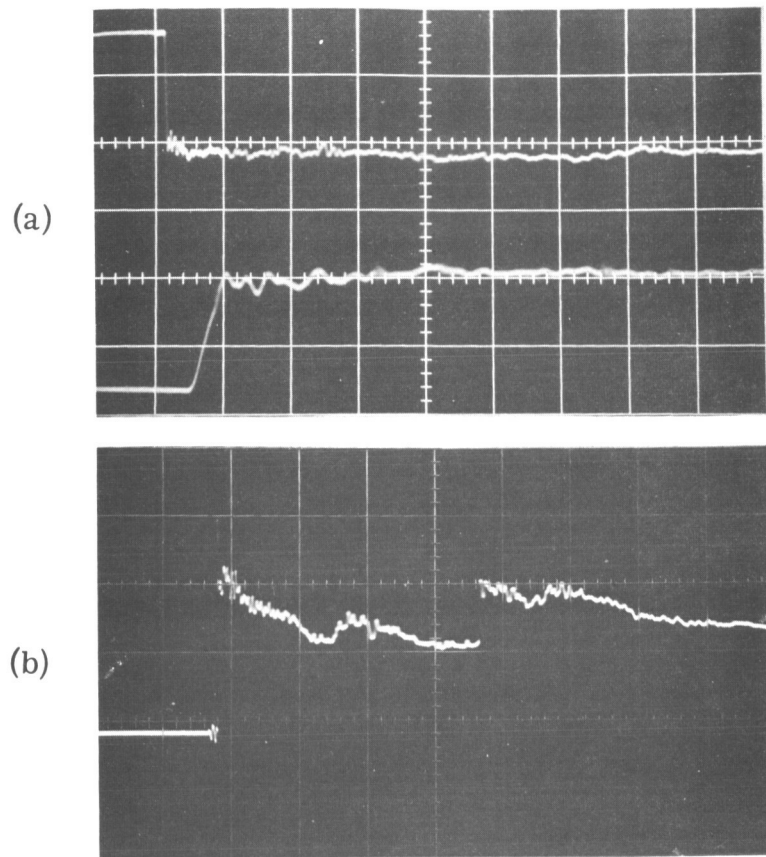


Figure A. 4 Response of 1/8 in. diameter lead metaniobate-tin pressure transducer direct to oscilloscope with 0.01  $\mu$ F shunt:

- (a) Mach 3.2 normal shock in 1 atm air, .02 v/div, 50  $\mu$ sec/div (upper beam) and 5  $\mu$ sec/div (lower beam)
- (b) Stoichiometric hydrogen-oxygen gaseous detonation initially at 2 atm, 0.05 v/div and 50  $\mu$ sec/div.

are evident. In both cases it is rather remarkable that no significant signals due to reflected waves from the end of the tin appear. About  $110\ \mu\text{sec}$  after the initial shock a slight negative going pulse is apparent, which agrees with the predicted arrival of the primary elastic wave from the rear of the tin. Apparently the elastic waves in the tin are attenuated with the aid of the silicone rubber, and thus no further design features are needed for long duration operation.

## 2. Heat Transfer Measurement.

Thin film resistance gauges for determination of the local heat transfer to the wall were used in the heterogeneous detonation studies. This type of gauge is used widely in shock tubes, and the construction and theory are described by Vidal<sup>(26)</sup> and Rabinowicz<sup>(27)</sup>. The design of the gauge used in our work is shown in Fig. A. 5. A strip of Hanovia liquid platinum (Hanovia No. 05, Engelhard Industries, Inc.) about 1 mm wide was painted on a fused quartz (General Electric Type 101) disk  $1/4$  in. diam. by  $1/16$  in. thick. The disk was then baked in an oven at  $1225^{\circ}\text{F}$  for 10 min. A second coat was applied in the same manner. Next the disks were coated with fluorocarbon lacquer (3M Co., No. FX-703) as a dielectric protection against ionized gases. Lead wires were soldered to the platinum and the disk was potted in a brass housing with silicone rubber. The resistance of the gauges varied from 16 to 19 ohms.

The gauge operates on the principle that a small temperature rise in the thin metal film results in a linear change in the resistance of the film, which appears as a voltage variation when used in conjunction with the circuit shown in Fig. A. 6. The response time of this type of gauge is known to be less than  $0.1\ \mu\text{sec}$ . The heat transfer to the gauge is then obtained by assuming one-dimensional unsteady heat conduction through an infinite slab. The solution for the heat transfer to the wall is,

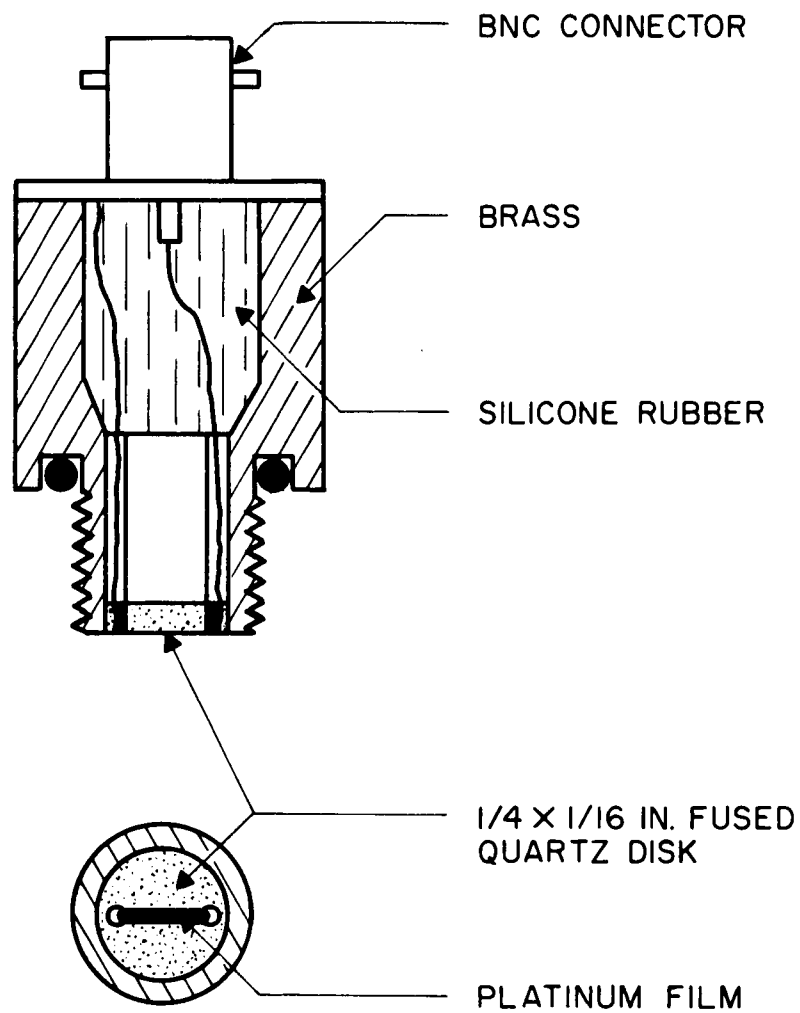


Figure A.5 Assembly Drawing of Heat Transfer Gauge.

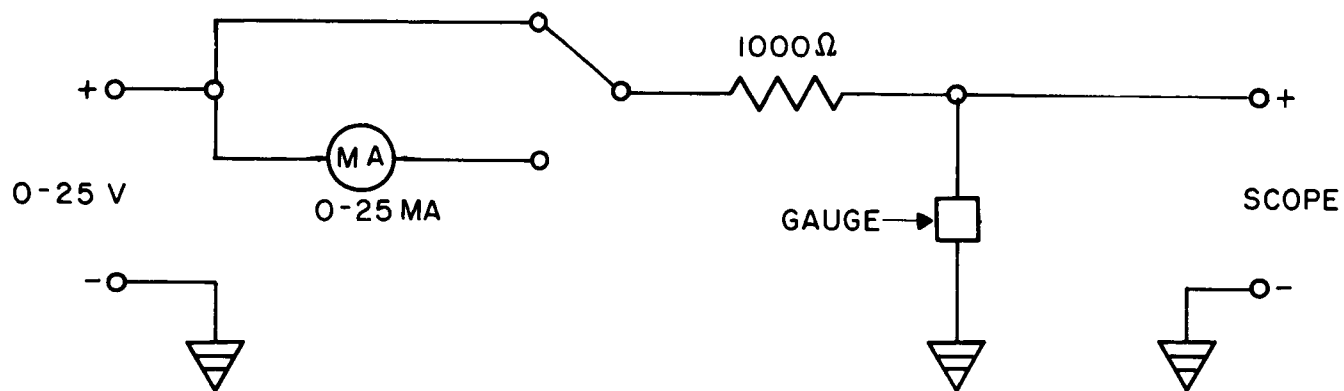


Figure A.6 Operating Circuit for Heat Transfer Gauge.

$$q(t) = \frac{\sqrt{k\rho c}}{\sqrt{\pi} \alpha R_o I} \left( \frac{E(0+)}{\sqrt{t}} + \int_0^t \frac{dE/d\tau}{\sqrt{t-\tau}} d\tau \right)$$

where  $R_o$  is the resistance of the gauge,  $I$  is the current through the gauge,  $\alpha$  is the coefficient of resistivity of the platinum,  $k$ ,  $\rho$ ,  $c$  are the conductivity density and heat capacity respectively of the quartz, and  $E$  is the voltage rise as measured on an oscilloscope.

The parameter  $\sqrt{k\rho c}$  was calculated from data supplied by the General Electric Company for their fused quartz, and a value of .0742 Btu per ft<sup>2</sup> °F sec<sup>1/2</sup> was used. The coefficient of resistivity was determined by calibrating the gauge in a distilled water bath which was held at various temperatures and a value, which varied somewhat for each gauge but averaged about  $0.50 \times 10^{-3}$  per °F, was obtained.

The reduction of the voltage output of the gauge as a function of time to wall heat transfer is a lengthy numerical calculation and was accordingly done on a digital computer. The Polaroid record of the oscilloscope trace was enlarged to 8 x 10 in. and the voltage tabulated at approximately 50 time intervals. Values of voltage between the tabulated points were obtained by interpolation using a third order polynomial. By assuming a straight line approximation to the curve over the small interval, the expression for heat transfer to the wall can be put in the following form which was carried out on a digital computer:

$$q(n\Delta t) = 2A\sqrt{\Delta t} \left[ \frac{E_o}{2\Delta t\sqrt{n}} + E'_{01}(\sqrt{n} - \sqrt{n-1}) + E'_{12}(\sqrt{n-1} - \sqrt{n-2}) + \dots + E'_{(n-1)(n)} \right]$$

where ,

$\Delta t$  is the interval of time between voltage measurements

$n$  represents the nth time interval

$E'$  is the derivative of voltage with respect to time in a given interval



A is the gauge constant which equals  $\frac{\sqrt{k\rho c}}{\sqrt{\pi} \alpha R_o I}$

The heat transfer coefficient  $C_H$  was also evaluated with the aid of the computer where  $C_H$  is defined according to Eq. (3.28). The following expression for  $C_H$  was used and the integration was done using Simpson's rule:

$$C_H (n\Delta t) = \frac{\int_0^{n\Delta t} q \, dt}{t(B - CE)}$$

where

$$B = \frac{\rho_1 U_s^3}{2} \left( \frac{\rho_2}{\rho_1} - 1 \right)$$

$$C = \frac{\rho_1 U_s C_{P1}}{\alpha I R_o} \left( \frac{\rho_2}{\rho_1} - 1 \right)$$

The response of the heat transfer gauge to a fully developed, stoichiometric hydrogen-oxygen gaseous detonation is shown in Fig. A.7. Useful data could not be taken over a longer time with the present setup due to the reflected shock from the end of the tube. These measurements were made as a means of checking the response of the gauge; however, they are of some interest by themselves because this data has not been widely reported. The heat transfer to the wall which was obtained from the traces is shown in Fig. A.8. Also shown is the data of Laderman, Hecht, and Oppenheim<sup>(28)</sup> which was obtained with a ceramic backing material. In addition, these authors report that the local heat transfer rates to the wall are nearly identical throughout the region of transition to detonation. The theoretical predictions of Sichel and David<sup>(29)</sup> are also indicated in the figures. These curves were developed by applying Chapman-Jouguet conditions to turbulent, shock tube-type, boundary layer

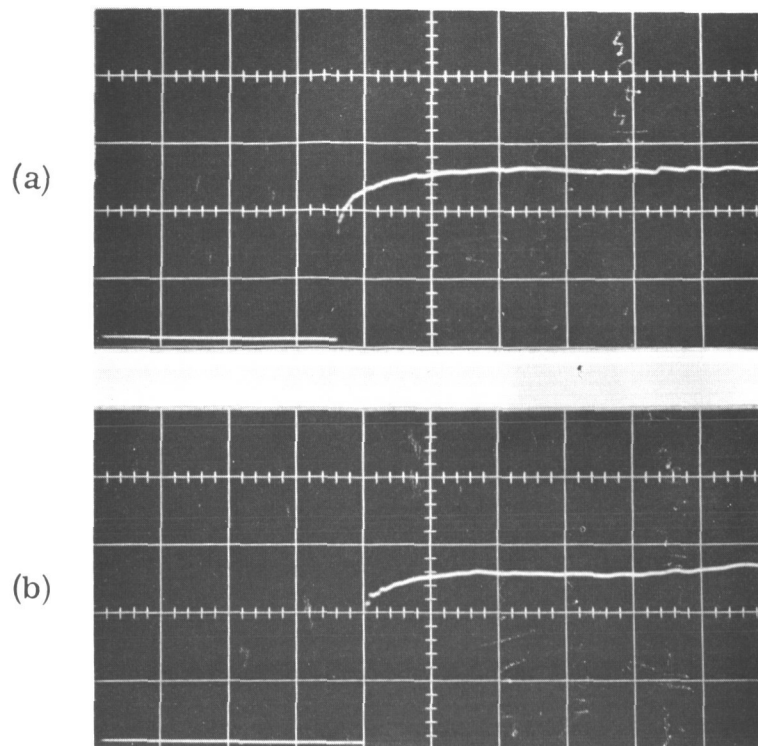


Figure A. 7 Response of heat transfer gauges to a 1 atm stoichiometric hydrogen-oxygen gaseous detonation in the side-wall of  $1/2 \times 3/8$  in. tube.

- (a) Gauge No. 3, 19 mA, 16 ohms, .02 v/div and 20  $\mu$ sec/div.
- (b) Gauge No. 10, 19 mA, 19 ohms, .02 v/div and 20  $\mu$ sec/div.

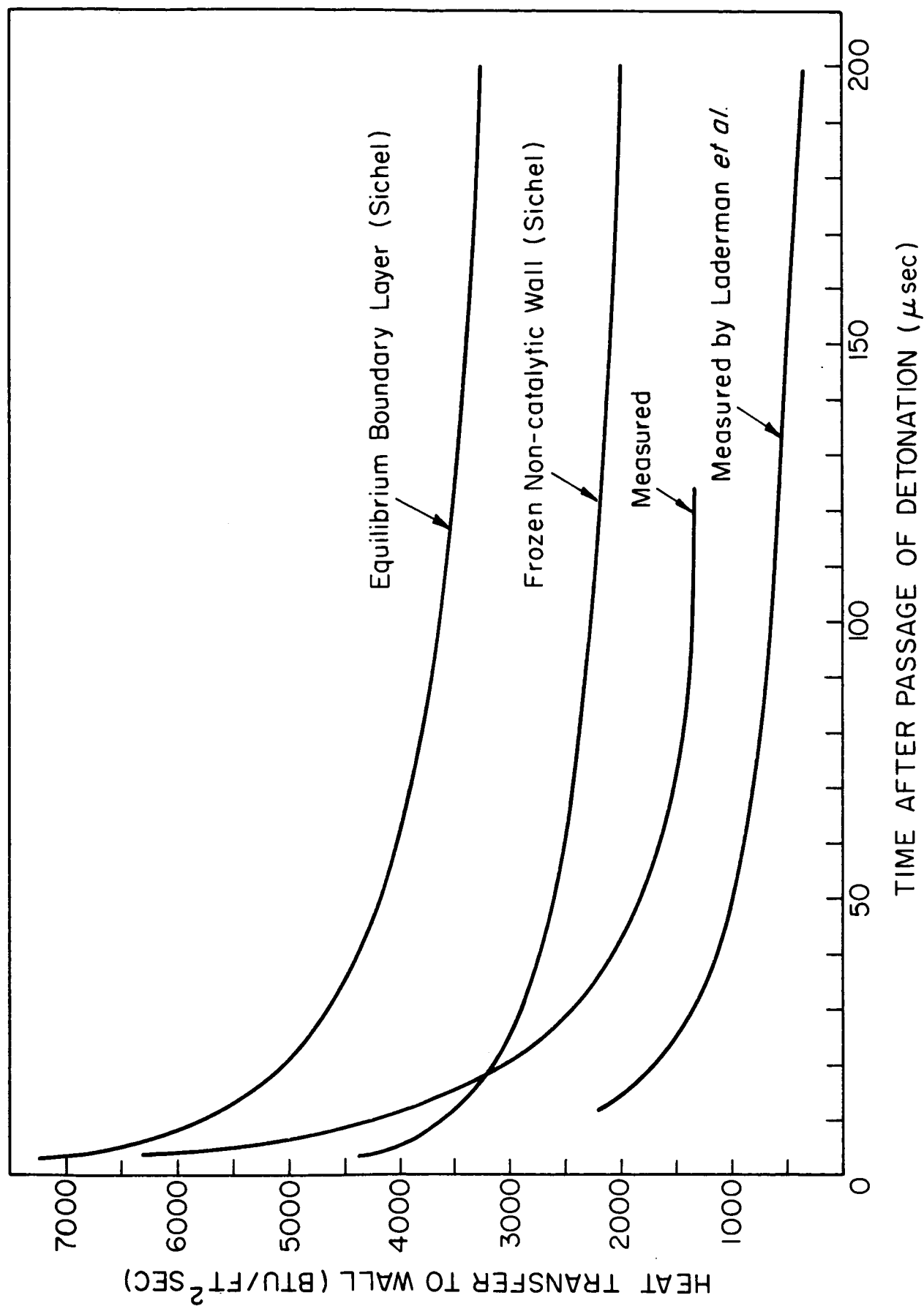


Figure A.8 Experimental and Theoretical Heat Transfer to the Wall Behind a 1 atm Stoichiometric Hydrogen-Oxygen Gaseous Detonation.

equations. The calculation was made for a frozen boundary layer with a non-catalytic wall and for a boundary layer in chemical equilibrium. The rarefaction wave behind the Chapman-Jouguet plane was not accounted for, however, and is the probable reason why the experimental results show higher rates of decrease than does the theory. The reported data here supercedes that reported earlier in Ref. (3).

### 3. Velocity Measurement.

The measurement of detonation velocity was made by using pressure switches located at several points along the tube. These switches, which are part of a multiple RC circuit, produce a signal of 2-3 volts with about 5  $\mu$ sec decay when they are closed by the passage of the wave. The switches and the RC circuit was described in Ref. (3). The signals are displayed on an oscilloscope operated in a raster mode. The raster used before<sup>(3)</sup> had the disadvantage that there was about 20% dead time between horizontal sweeps. As a result any pressure switch signal during this dead-time was lost.

To avoid this dead time an external raster circuit shown in Fig. A. 9 in conjunction with a function generator (Exact Electronics type 255) are used with an oscilloscope (Tektronics model 555). The triangular wave signal from the generator is fed into the external sweep of the scope. A trigger signal from the generator at the beginning of each cycle allows the trace to move vertically for a short period of time unless a 150 v. signal is applied from a thyatron unit. When this signal is received the trace is moved vertically. The signal from the pressure switch circuit is superimposed on the vertical sweep signal by means of a type CA plug-in unit. Because the generator gives one impulse at the beginning of the cycle, each horizontal trace is actually a double trace due to beam travel over itself during one half of the cycle. However, no confusion is generated by this situation since the direction of the decay of the pressure switch signal can be used to find out at what part of the

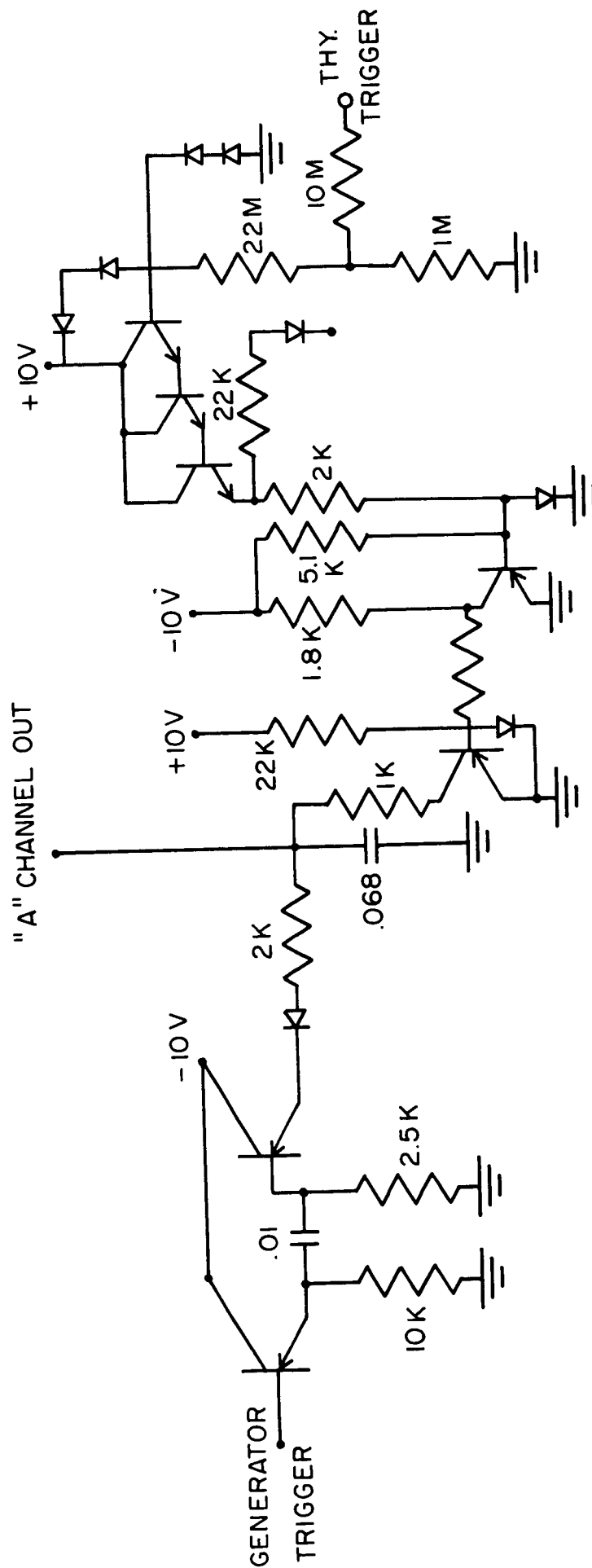


Figure A. 9 Schematic Diagram of Raster Circuit.

cycle the pressure switch signal is started. Figure A.10 shows a typical raster record where signal decays to both left and right can be seen. Measurement of time between two consecutive signals and knowledge of the distance between pressure switches responsible for these signals are used to calculate an average velocity for that distance.

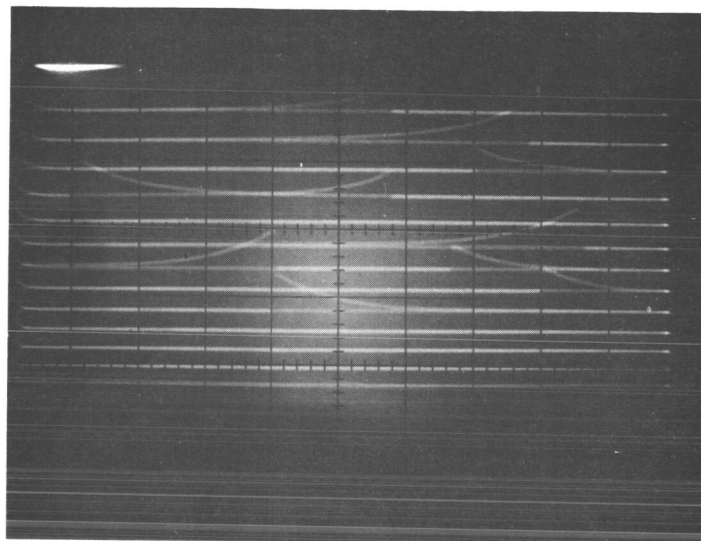


Figure A.10 Typical raster record.

Run no. 263,  $10 \mu\text{sec}/\text{cm}$ , time advancing from top to bottom  
(example: the time between the last 2 pressure  
switch signals =  $160 \mu\text{sec.}$ )

## REFERENCES

1. Nicholls, J.A., Dabora, E.K., and Ragland, K.W., "A Study of Two Phase Detonation as it Relates to Rocket Motor Combustion Instability," NASA CR-272, Aug. 1965.
2. Dabora, E.K., Ragland, K.W., and Nicholls, J.A., "A Study of Heterogeneous Detonations," Astronautica Acta, Vol. 12, 1966, p. 9.
3. Dabora, E.K., Ragland, K.W., Ranger, A.A., and Nicholls, J.A., "Two Phase Detonations and Drop Shattering Studies," University of Michigan, 06324-2-T, April 1966.
4. Morris, D.H., Wojcieki, S., and Oppenheim, A.K., "Development of Detonation in Liquid Fuel Spray with Gaseous Oxidizer — Preliminary Experiments," NASA CR-80098, Oct. 1966.
5. Dabora, E.K., "Production of Monodisperse Sprays," Rev. Sci. Instr., to be published in April 1967.
6. Courant, R. and Friedrichs, K., Supersonic Flow and Shock Waves, Interscience Publishers, New York, 1948.
7. Blasius, H., "Grenzschichten in Flussigkeiten mit kleiner Reibung," Z. Math. u. Phys., 56, 1 (1908).
8. Schlichting, H., Boundary Layer Theory, McGraw-Hill, 1960, p. 537.
9. Mirels, H., "Laminar Boundary Layer Behind Shock Advancing into Stationary Fluid," NACA TN-3401, March 1955.
10. Martin, W.A., "An Experimental Study of the Boundary Layer Behind a Moving Plane Shock Wave," Univ. of Toronto, UTIA Rept. no. 47, May 1957.
11. Emmons, H.W., and Leigh, D.C., "Tabulation of the Blasius Function with Blowing and Suction," Aeronautical Research Council Current Paper No. 157, London, 1954.
12. Marxman, G.A., "Combustion in the Turbulent Boundary Layer on a Vaporizing Surface," Tenth Symposium (International) on Combustion, The Combustion Institute, 1965, pp. 1337-1349.
13. Rabin, E., Schallenmuller, A.R., and Lawhead, R.B., "Displacement and Shattering of Propellant Droplets," Final Summary Rept. AFOSR, Washington, D.C., TR60-75, March 1960.



14. Lane, W.R. , "Shatter of Drops in Streams of Air," J. of Ind. and Eng. Chemistry, Vol. 43, No. 6, June 1951, pp. 1312-1317.
15. Hanson, A.R. , Domich, E.G. , and Adams, H.S. , "An Experimental Investigation of Impact and Shock Wave Break-up of Liquid Drops," Res. Rept. no. 125, Rosemount Aero. Lab. , Minneapolis, Minn. , Jan. 1956.
16. Hanson, A.R. , and Domich, E.G. , "The Effect of Liquid Viscosity on the Break-up of Droplets by Air Blasts—A Shock Tube Study," Eng. Res. Rept. 130, Univ. of Minnesota Institute of Technology, June 1956.
17. Engel, O.G. , "Fragmentation of Waterdrops in the Zone Behind an Air Shock," J. of Res. Nat'l. Bur. Standards, Vol. 60, No. 3, March 1958.
18. Rojec, E.A. , "Photographic Investigation of Shear Type Droplet Breakup," Rocketdyne Res. Rept. 63-39, Nov. 1963.
19. Wolfe, H.E. and Andersen, W.H. , "Kinetics, Mechanism, and Resultant Droplet Sizes of the Aerodynamic Breakup of Liquid Drops," Rept. no. 0395-04(18)SP Aerojet-General Corp. , April 1964.
20. Nicholson, J.E. and Hill, A.F. , "Rain Erosion on Spike Protected Supersonic Radomes," Mithas, Inc. , Cambridge, Mass. , MC-61-6-R3, April 1963.
21. Clark, B.J. , "Breakup of a Liquid Jet in a Transverse Flow of Gas," NASA TN D-2424, Aug. 1964.
22. Morrell, G. and Povinelli, F.P. , "Break-up of Various Liquid Jets by Shock Waves and Applications to Resonant Combustion," NASA TN D-2423, August 1964.
23. Zaitsev, S.G. , "Measurement of Rapidly Varying Pressures in a Gas," Pribery i Tekhn. Eksperim, 6, 97 (1958).
24. Soloukhin, R.I. , "Detonation Waves in Gases," Usp. Fiz Nauk, 68, 513 (1959).
25. Jaffe, H. , "Piezoelectricity," Encyclopaedia Britannica, Vol. 17, 1965, pp. 910-916.
26. Vidal, R.J. , "Model Instrumentation Techniques for Heat Transfer and Force Measurements in a Hypersonic Shock Tunnel," AD 917-A-1, Feb. 1956.

27. Rabinowicz, J., "Aerodynamic Studies in the Shock Tube," California Institute of Technology Hypersonic Research Project Memorandum No. 38, June 1957.
28. Laderman, A.J., Hecht, G.J., and Oppenheim, A.K., "Thin Film Thermometry in Detonation Research," Temperature—Its Measurement and Control in Science and Industry, Vol. 3, Part 2, 1962.
29. Sichel, M. and David, T.S., "Transfer Behind Detonations in  $H_2-O_2$  Mixtures," AIAA J., Vol. 4, No. 6, 1966, pp. 1089-1090.